

The  
University  
Of  
Sheffield.

DISSERTATION SUBMITTED FOR THE DEGREE OF  
DOCTOR OF PHILOSOPHY  
DEPARTMENT OF PHYSICS AND ASTRONOMY

---

**High-bandwidth  
electrical generation of  
single and entangled photons**

---

Jonathan Rupert Ayang Müller

December 2022



# Abstract

Semiconductor quantum dots (QDs) are a promising source of quantum light, combining sub-Poissonian photon statistics, high entanglement fidelities, and compact integration. This thesis examines the temporal driving methodology of electrically-driven semiconductor QDs and its impact on the quantum optical characteristics of the emitted light. To this end, we introduce the design and fabrication of an ultra-high-bandwidth QD light-emitting diode (LED). We demonstrate fast control of charge carrier injection and tunnelling, and report generation of single photons at a record 3.05 GHz clock rate.

Importantly, we introduce a novel driving scheme for entangled-photon sources that rely on radiative cascades of atom-like few-level systems. Using a rate-equation model, we show that an early reinitialisation of the quantum system—before the radiative cascade has completed—may produce entangled photon pairs at a higher rate compared to either conventional pulsed operation or continuous driving of the system. This is subsequently implemented in practice, demonstrating an entangled-pair rate enhanced by  $(21 \pm 3)\%$  compared to the same device when driven continuously. Employing this novel driving scheme, we also demonstrate the electrical generation of entangled-photons at a record 1.15 GHz clock rate with an overall entanglement fidelity of  $(79.5 \pm 1.1)\%$ .

Finally, we present a theoretical model describing the integration of a QD entangled-light-emitting diode (E-LED) in entanglement-based measurement-device-independent quantum key distribution (MDI-QKD). We conclude that a proof-of-principle experimental demonstration is feasible, yielding a peak bit-exchange fidelity of up to 84.3% for a four-state BB84 protocol.

These results may particularly benefit the performance of future long-distance quantum networks using atom-like quantum light sources. Furthermore, the ultra-high-bandwidth device and early reinitialisation scheme may be combined with other techniques to accelerate the radiative lifetime of the emitter, such as Purcell enhancement, further enhancing the quantum light emission for photonic applications.

# Declaration of Authorship

I declare that the work presented in this thesis is my own research, except where otherwise stated, and has not been previously submitted for a degree in this or another university. Parts of the work submitted in this thesis have been published as listed in Publications.

Jonathan Müller

December, 2022



# Acknowledgements

This thesis would not have been possible without the kind and passionate support of many others. As a result, these past few years have brought me many friendships, insights, and unique experiences. First of all, I would like to thank **Sasha Tartakovskii** and **Andrew Shields** for the opportunity to become part of this project and the supervision of my PhD.

I highly enjoyed the pleasant and fruitful research atmosphere at Toshiba CRL. There are too many great people in the group to list them all, so I will only mention a few here by name. Most of all I am deeply grateful to **Mark Stevenson** for the excellent supervision and advice throughout my PhD experience, both inside and out of the lab. In addition, I would like to thank **Joanna Skiba-Szymanska** for kindly teaching me and helping me out in the cleanroom and fabricating some of the most important samples. I'd also like to thank **Jan Huwer** and **Matthew Anderson** in particular for numerous insightful discussions on the nature of quantum dots, physics, and everything else. Finally I'd like to thank all the other researchers and support staff at Toshiba for the fantastic atmosphere throughout my PhD. A very special mention also goes to all the other PhD students at Toshiba, who have made this experience so uniquely delightful and memorable in Cambridge.

I would also like to thank **David Ritchie**, **Lucy Goff**, **Melanie Tribble**, and all the other technical staff at the Cavendish for kindly hosting me in the Semiconductor Physics group at the University of Cambridge, and for the fruitful collaboration on sample growth and fabrication.

I am very grateful to the European Union for generously funding this project via the Horizon 2020 research and innovation programme under the Marie Skłodowska-Curie

## ACKNOWLEDGEMENTS

---

grant Agreement No. 721394. This included many stimulating seminars with all the other research groups in the 4Photon network. In particular I would like to thank **Stefano Sanguinetti**, **Sergio Bietti**, and **Anna Pisano** for supervising the program and organising many of the excellent events.

Many thanks also to **Pjotr Wroński**, **Fauzia Jabeen**, **Christian Schneider**, and **Sven Höfling** for kindly hosting me for an insightful research stay in the Technische Physik group at the Universität Würzburg.

Finally, I would like to thank my family, **Yu Müller-Chiu**, **Gerhard Müller**, and **Elisa Müller**, as well as all my other friends for their tireless support throughout the years, I could not have done it without you.

# Publications

## Articles

- **J. R. A. Müller**, R. M. Stevenson, J. Skiba-Szymanska, G. Shooter, J. Huwer, I. Farrer, D. A. Ritchie, and A. J. Shields, *Active reset of a radiative cascade for superequilibrium entangled photon generation*, Physical Review Research **2**, 043292 (2020)
- G. Shooter, Z. Xiang, **J. R. A. Müller**, J. Skiba-Szymanska, J. Huwer, J. Griffiths, T. Mitchell, M. Anderson, T. Müller, A. B. Krysa, R. M. Stevenson, J. Heffernan, D. A. Ritchie, and A. J. Shields, *1 GHz clocked distribution of electrically generated entangled photon pairs*, Optics Express **28**, 24 (2020)
- C. Gustin, L. Hanschke, K. Boos, **J. R. A. Müller**, M. Kremser, J. J. Finley, S. Hughes, and K. Müller, *High resolution spectroscopy of a quantum dot driven bichromatically by two strong fields*, Physical Review Research **3**, 013044 (2021)

## Conference and workshop presentations

- ‘Active Reset of a Quantum-Dot-LED for Rapid Entangled Photon Generation’ (talk), **SemiconNano 2021** (moved online), Milan, Italy (Aug 2021)
- ‘Active reset of an entangled-LED for superequilibrium entangled photon generation’ (talk), **International Conference on Solid State Devices and Materials (SSDM)** (moved online), Toyama, Japan (Sep 2020)

- ‘Gigahertz-clocked active reset of an entangled LED’ (talk), **3rd 4-Photon Workshop** (moved online), Milan, Italy (Jun 2020)
- ‘Active reset of a radiative cascade for superequilibrium entangled photon generation’ (poster), **Bristol Quantum Information Technologies Workshop** (moved online), Bristol, UK (Apr 2020)
- ‘Generation of entangled photon pairs at gigahertz repetition rates via an ultrafast LED’ (talk), **SPIE Photonics West**, San Francisco, USA (Feb 2020)
- ‘Active reset of a radiative cascade for superequilibrium entangled photon generation’ (poster), **Nanophotonics Winter School**, Sheffield, UK (Jan 2020)
- ‘Towards a quantum relay based on droplet epitaxy quantum dots’ (talk), **2nd 4-Photon Workshop**, Munich, Germany (Oct 2019)
- ‘Electrical generation of entangled light via single droplet epitaxy quantum dot based LEDs’ (poster), **Quantum devices for non-classical light generation and manipulation**, Erice, Italy (Oct 2019)
- ‘Quantum optical properties of single droplet epitaxy quantum dots’ (poster), **Winter school on quantum dots: from growth to fundamental properties**, Würzburg, Germany (Feb 2019)
- ‘Towards a quantum relay based on droplet epitaxy quantum dots’ (talk), **1st 4-Photon Workshop**, Eindhoven, Netherlands (Sep 2018)
- ‘Quantum optical properties of single droplet epitaxy quantum dots’ (poster), **School on Introduction to Quantum Information**, Basel, Switzerland (Feb 2018)

# Contents

<b>Abstract</b>	<b>iii</b>
<b>Declaration of Authorship</b>	<b>v</b>
<b>Acknowledgements</b>	<b>vii</b>
<b>Publications</b>	<b>ix</b>
<b>List of Figures</b>	<b>xv</b>
<b>List of Abbreviations</b>	<b>xix</b>
<b>1 Introduction</b>	<b>1</b>
<b>2 Background and state of the art</b>	<b>5</b>
2.1 Quantum information . . . . .	5
2.1.1 Polarisation qubits . . . . .	6
2.1.2 Entanglement . . . . .	7
2.2 Semiconductor quantum dots as artificial atoms . . . . .	8
2.2.1 Entangled photon pairs and the radiative cascade . . . . .	9
2.3 Characteristics of quantum light . . . . .	11
2.3.1 Entanglement fidelity . . . . .	11
2.3.2 Photon statistics . . . . .	15
2.3.3 Indistinguishability . . . . .	16
2.4 Tailoring the quantum dot emission . . . . .	20
2.4.1 Initialisation of the quantum dot state . . . . .	20

2.4.2	Tuning the emission energy . . . . .	22
2.4.3	Extraction efficiency . . . . .	23
2.4.4	Emission wavelengths . . . . .	25
2.5	Quantum key distribution . . . . .	26
2.5.1	BB84 protocol . . . . .	26
2.5.2	Entanglement-based QKD . . . . .	27
2.5.3	Measurement-device-independent QKD . . . . .	28
2.6	Quantum repeaters . . . . .	30
2.7	Summary . . . . .	30
<b>3</b>	<b>Experimental techniques</b>	<b>33</b>
3.1	Sample design and fabrication . . . . .	33
3.1.1	Stranski-Krastanov growth of InAs quantum dots . . . . .	33
3.1.2	Design of the distributed Bragg reflector . . . . .	35
3.1.3	Electronic band structure of a quantum dot LED . . . . .	39
3.1.4	Fabrication of quantum light emitting diodes . . . . .	41
3.2	Cryogenic and optical measurement setup . . . . .	46
3.2.1	Measurement of the fine-structure splitting . . . . .	46
3.2.2	Calibration of the quantum dot polarisation eigenbasis . . . . .	48
<b>4</b>	<b>High-bandwidth pulsed single-photon sources</b>	<b>55</b>
4.1	Low-capacitance diode design . . . . .	55
4.1.1	Design and fabrication of a high-bandwidth QD LED . . . . .	58
4.2	Experimental operation of gigahertz-clocked single photon sources . . . . .	63
4.2.1	Experimental setup . . . . .	63
4.2.2	Ultrafast control of the tunnelling rate . . . . .	66
4.2.3	Pulsed generation of single photons at a 3 GHz clock rate . . . . .	69
4.2.4	Multiphoton contributions due to re-excitation . . . . .	72
4.3	Conclusion . . . . .	75

<b>5</b>	<b>Entangled photon generation beyond the continuous driving limit</b>	<b>77</b>
5.1	Rate equation model . . . . .	78
5.2	Active reset driving for superequilibrium entangled pair rates . . . . .	79
5.2.1	Superior entanglement fidelity via active reset . . . . .	85
5.2.2	Active reset in the weak pumping regime . . . . .	88
5.3	Experimental active reset . . . . .	92
5.3.1	Driving conditions . . . . .	92
5.3.2	Optical setup . . . . .	95
5.4	Experimental results . . . . .	96
5.4.1	Experimental superequilibrium entangled pair rates . . . . .	102
5.5	Compatibility with optical biexciton initialisation . . . . .	104
5.6	Conclusion . . . . .	105
<b>6</b>	<b>Entangled LEDs for measurement-device-independent QKD</b>	<b>107</b>
6.1	Entanglement-based MDI-QKD protocol . . . . .	108
6.2	Theoretical model . . . . .	110
6.2.1	Four-photon measurement . . . . .	111
6.3	Numerical simulations . . . . .	114
6.3.1	Fidelity to the ideal E-MDI-QKD protocol . . . . .	117
6.4	Conclusion . . . . .	121
<b>7</b>	<b>Summary and outlook</b>	<b>123</b>
<b>A</b>	<b>Appendix</b>	<b>125</b>
A.1	Bit parity of E-MDI-QKD . . . . .	125
A.2	Unintentional four-photon correlations . . . . .	125
A.3	Regions of anti-correlated bit parity . . . . .	127
	<b>Bibliography</b>	<b>129</b>



# List of Figures

2.1	Polarisation state on the Poincaré sphere . . . . .	7
2.2	Diagram of biexciton-exciton radiative cascade . . . . .	10
2.3	Characterising polarisation entanglement . . . . .	12
2.4	Experimental second-order biexciton-exciton cross-correlation . . . . .	13
2.5	Characterising entangled light . . . . .	14
2.6	Schematic HBT and HOM setups . . . . .	16
2.7	Typical HBT second-order correlation . . . . .	17
2.8	Modelled two-photon interference . . . . .	18
2.9	Superequilibrium entangled pair rate for active reset driving . . . . .	29
3.1	Schematic illustration of the Stranski-Krastanov growth mode . . . . .	34
3.2	Typical photoluminescence spectrum of a strain-grown quantum dot . . . . .	35
3.3	Cross-sectional SEM micrograph of a planar microcavity . . . . .	36
3.4	Schematic of the experimental characterisation setup . . . . .	38
3.5	Experimental and simulated reflectivity spectrum . . . . .	39
3.6	p-i-n diode design . . . . .	40
3.7	Etching and metal deposition via photolithography . . . . .	42
3.8	Quantum dot LED fabrication . . . . .	43
3.9	Optical micrographs of a fabricated sample . . . . .	44
3.10	Current-voltage curve and micrograph of an E-LED at $T = 17.5$ K . . . . .	44
3.11	Electroluminescence spectrum and intensity vs applied current . . . . .	45
3.12	SEM micrograph and schematic of fabricated device . . . . .	47
3.13	Optical setup to measure the FSS splitting and polarisation . . . . .	47

3.14	Polarimeter measurements to determine FSS and fibre birefringence . . . . .	49
3.15	Process steps to determine the required polarisation bases . . . . .	50
4.1	Equivalent circuit of a p-i-n diode . . . . .	56
4.2	Normalised EL emission on a standard QD LED, electrically driven via a 1 GHz square wave . . . . .	57
4.3	Schematic illustration of device cross section . . . . .	58
4.4	GHz quantum dot LED fabrication . . . . .	60
4.5	SEM micrograph and schematic of fabricated device . . . . .	62
4.6	Oscillogram of the electrical pulse generator output after attenuation	64
4.7	Optical setup for time-correlated single photon counting . . . . .	64
4.8	Typical instrument response of the SSPD and time-correlated single- photon-counting module . . . . .	65
4.9	Time-resolved pulsed EL emission for different DC biases . . . . .	66
4.10	Time-resolved EL emission as a function of DC bias . . . . .	67
4.11	EL spectra as a function of DC bias . . . . .	68
4.12	Emission characteristics extracted via Lorentzian fits . . . . .	70
4.13	Gigahertz-clocked single photon generation . . . . .	71
4.14	EL spectra for different driving conditions . . . . .	73
5.1	Schematic of the rate equation model . . . . .	78
5.2	QD populations for different driving modes, calculated via a rate equation model . . . . .	80
5.3	Optimum entangled pair generation in equilibrium . . . . .	82
5.4	Superequilibrium entangled pair rate for active reset driving . . . . .	83
5.5	Mean cumulative number of entangled photon pairs emitted over time	84
5.6	Fidelity to a maximally entangled Bell state vs emission delay . . . . .	87
5.7	Time-averaged emission intensity in AR driving as a function of pump rate . . . . .	89
5.8	Modelled population and fidelity at a reduced pump rate . . . . .	89
5.9	Modelled entangled pair rate in the weak pumping regime . . . . .	91

---

5.10	EL spectra for different driving conditions. . . . .	93
5.11	Time-resolved EL intensity . . . . .	94
5.12	(Time-averaged) entangled pair generation advantage . . . . .	95
5.13	Schematic of the optical setup to characterise active reset driving . . .	96
5.14	Time-tagged, time-resolved continuous entangled pair generation . . .	97
5.15	Time-tagged, time-resolved active reset . . . . .	99
5.16	Integrated measured entanglement fidelity in AR driving . . . . .	101
5.17	Comparison of the entanglement fidelity for AR and DC driving . . .	101
5.18	Cumulative entangled pair emission . . . . .	103
5.19	Modelled ratio of AR to DC entangled pair generation efficiency . . .	104
6.1	Measurement setup for entanglement-based MDI-QKD . . . . .	108
6.2	Schematic of entanglement-based MDI-QKD . . . . .	111
6.3	Time-resolved optical intensities of four contributing sources . . . . .	115
6.4	Fourth-order correlation for different polarisation encodings . . . . .	116
6.5	E-MDI-QKD fidelity for different polarisation encodings . . . . .	118
6.6	Mean fourth-order correlation and mean fidelity . . . . .	119
6.7	Mean fidelity along diagonal and after post-selection . . . . .	119
A.1	E-MDI-QKD Fidelity for H input encoding . . . . .	127



# List of Abbreviations

<b>AlAs</b>	aluminium arsenide
<b>AR</b>	active reset
<b>BS</b>	beam splitter
<b>BSM</b>	Bell state measurement
<b>CCD</b>	charge-coupled device
<b>CW</b>	continuous wave
<b>DBR</b>	distributed Bragg reflector
<b>DC</b>	direct current
<b>EL</b>	electroluminescence
<b>E-LED</b>	entangled-light-emitting diode
<b>E-MDI</b>	entanglement-based measurement-device-independent
<b>EPC</b>	electrically driven polarisation controller
<b>FWHM</b>	full width at half maximum
<b>FSS</b>	fine-structure splitting
<b><i>G</i></b>	ground state
<b>GaAs</b>	gallium arsenide

## LIST OF ABBREVIATIONS

---

<b>He</b>	Helium
<b>HWP</b>	half-wave plate
<b>InAs</b>	indium arsenide
<b>IPA</b>	isopropyl alcohol
<b>LED</b>	light-emitting diode
<b>LP</b>	linear polariserhd
<b>MBE</b>	molecular-beam epitaxy
<b>MDI</b>	measurement-device-independent
<b>NIR</b>	near-infrared
<b>PBS</b>	polarising beam splitter
<b>PCB</b>	printed circuit board
<b>PL</b>	photoluminescence
<b>PMMA</b>	poly(methyl methacrylate)/ acrylic
<b>QD</b>	quantum dot
<b>QBER</b>	quantum bit error rate
<b>QKD</b>	quantum key distribution
<b>QWP</b>	quarter-wave plate
<b>RF</b>	radio frequency
<b>SHF</b>	super high frequency
<b>SIL</b>	solid immersion lens
<b>SPDC</b>	spontaneous parametric down-conversion

<b>SSPD</b>	superconducting single-photon detector
<b>TPE</b>	two-photon excitation
<b>UV</b>	ultraviolet
<b>WCP</b>	weak coherent pulse
<b>WL</b>	wetting layer
<b>X</b>	neutral exciton
<b>XX</b>	neutral biexciton



# 1 | Introduction

Optical fibre communications revolutionised global telecommunication networks in the 20th century [Kul04], transforming the way we communicate with each other. Encoding signals via optical pulses enabled the exchange of information at longer distances and higher data rates compared to electrical cables while ensuring resistance to interference and crosstalk [Sen09]. Perhaps similarly, quantum photonics is set to, again, revolutionise our communication infrastructure [Kim08, Qiu14]. By leveraging the fundamentals of quantum mechanics, quantum key distribution (QKD), for example, enables its users to create a shared, provably secure private key via a public communication channel—a task that is impossible via exclusively classical communication [Ben84, Lo99, Gis02].

Single and entangled photons in turn form a fundamental building block for a wide spectrum of applications in quantum information, promising enhanced secure key rates in QKD through elimination of multiphoton emission [Gis02, Hwa03] and global-scale unconditionally secure networks with entanglement-based quantum repeaters [Dür99]. A popular source of quantum light are semiconductor QDs [Dre94, War00]. Much like a single atom, such nanoscopic structures lead to the formation of quantised few-level systems. When the population is transferred between energy levels of the system, the QD can be brought to emit quantum light. Such semiconductor QDs have been shown to emit single and entangled photons with near ideal properties for quantum photonic applications in terms of single photon purity [Han18], entanglement fidelity [Hub18b], indistinguishability [Din16], on-demand generation [Mül14], quantum efficiency [Che18, Liu19, Wan19] as well as on-chip integration [Shi07, Hub18a], electrical operation [Yua02, Sal10], and compatibility with optical fibre quantum networks [Olb17, Xia19].

In order to operate such a quantum light source, it is crucial to control the population of the few-level quantum system. Recent implementations of quantum communication channels based on laser-generated photonic signals operate at GHz clock rates in order to achieve fast data transmission rates [Yua18]. In order to interface with such systems, it is thus desirable to generate single and entangled photons at similar clock rates [Ben05, Har13].

In this thesis we study the quantum optical effects resulting from the temporal driving methodology of the system. To this end, we introduce the fabrication of an ultra-high-bandwidth quantum-light emitting diode. This allows us to control electrical charge carrier injection and tunnelling on time scales significantly shorter than the radiative lifetime of the emitters. This device is then employed to generate single and entangled photons at record clock rates. Furthermore, we demonstrate how a premature reinitialisation of the QD radiative emission cascade may enhance the entangled-pair emission rate compared to either completing the emission cascade or driving the system continuously. This thesis is composed of seven chapters:

In chapter 2 we begin with a brief introduction to quantum information and motivate the use of photons as polarisation qubits. We introduce semiconductor QDs as a source of single and entangled photon pairs and present associated criteria to assess single-photon purity, entanglement and other quantum optical characteristics of light. The chapter ends with a short introduction to QKD as a potential application of quantum light.

In chapter 3 we describe relevant experimental techniques that are employed throughout the thesis. We describe the concept, growth, and fabrication of quantum-light-emitting-diodes based on quantum dots. This is followed by a description of the cryogenic and optical methods used to generate quantum light in practice.

In chapter 4 we present a super-high-frequency (SHF) single-photon LED. We describe the design and fabrication of such a device. Subsequently, we demonstrate the experimental operation at gigahertz clock rates to generate single photons.

In chapter 5 we focus on the generation of entangled photons. First, we establish a theoretical model to motivate high-clock rate operation of the quantum emitter. We

---

theoretically and experimentally investigate the use of fast-clocked driving schemes to generate entangled photons at superior entangled pair rates and fidelities compared to continuous driving schemes.

In chapter 6 we theoretically explore the integration of E-LEDs in a QKD scheme. After introducing the envisioned protocol and theoretical model, we present and analyse the numerically computed four-photon correlations and fidelities resulting from such an implementation.

Finally, in chapter 7 we briefly summarise the results presented in this thesis and discuss possible directions for future research based on this work.



# 2 | Background and state of the art

This chapter provides an overview of the theoretical framework required to describe and characterise single and entangled photons. We begin in section 2.1 with a brief introduction to quantum information and quantum communication. For the work presented in this thesis, we employ semiconductor QDs to generate quantum light. Consequently, in section 2.2 we describe the theoretical basis of the generation of entangled photon pairs from semiconductor QDs via the radiative cascade. This is followed in section 2.3 by the quantum optical framework to characterise entangled light. Here, we also provide the reader with the basic foundation to characterise the photon statistics and indistinguishability of light. In section 2.4 we continue the chapter with an overview of the current state of the art of quantum light generation from QDs in terms of excitation techniques, wavelength tuning, and extraction efficiency. Finally, a promising near-term application of quantum photonics is the use in QKD, allowing for encrypted communication protected by the laws of quantum mechanics. We thus conclude the chapter with a brief introduction to QKD in section 2.5.

## 2.1 Quantum information

The non-classical nature of quantum information theory offers fundamental advantages over classical information technology. Access to the quantum state of the underlying physical system grants, for example, the possibility of unconditionally secure encryption [Ben84, Eke91, Lo99] or the ability to solve a certain set of problems exponentially faster than any classical device [Fey86, Aru19].

The basic building block of quantum information is the qubit, describing the quantum state of a two-level system. A wide spectrum of quantum systems have been shown to enable implementations of a qubit, such as trapped atoms [Cir95], superconducting circuits [Cla08, Aru19], solid state impurity centres [Kan98, Doh13], self-assembled semiconductor quantum dots [Dre94, War00, Fin01], and many more.

For quantum communication, photons are uniquely suitable as qubits due to their fast transmission at the speed of light and weak interaction with the environment [Cla69, Kni01, Gis07]. The quantum information is encoded via the degrees of freedom of photons, for example via the photon number, time bin, orbital angular momentum, or polarisation [Fla19]. Polarisation in particular is a popular encoding of qubit states, partly due to its natural prevalence e.g. in the emission from trapped atoms [Cla69, Asp81] or quantum dots [Ben00]. In addition, optical components to manipulate polarisation, such as wave-plates and polarisers, are well-established and widely available.

### 2.1.1 Polarisation qubits

We begin by choosing the rectilinear polarisation basis, consisting of the horizontal and vertical polarisation state, as the qubit eigenbasis. Using Jones calculus [Jon41, Fow89, Ste17], the horizontally  $|V\rangle$  and vertically  $|H\rangle$  polarised single qubit state vectors can be written as

$$|H\rangle = \begin{pmatrix} 1 \\ 0 \end{pmatrix} \quad |V\rangle = \begin{pmatrix} 0 \\ 1 \end{pmatrix} \quad (2.1)$$

respectively. The diagonal  $|D\rangle$ , anti-diagonal  $|A\rangle$ , right-circular  $|R\rangle$ , and left-circular  $|L\rangle$  polarisation states are then given by

$$\begin{aligned} |D\rangle &= \frac{1}{\sqrt{2}} (|H\rangle + |V\rangle) & |A\rangle &= \frac{1}{\sqrt{2}} (|H\rangle - |V\rangle) \\ |R\rangle &= \frac{1}{\sqrt{2}} (|H\rangle - i|V\rangle) & |L\rangle &= \frac{1}{\sqrt{2}} (|H\rangle + i|V\rangle) . \end{aligned} \quad (2.2)$$

More generally, an arbitrary polarisation state

$$|\psi\rangle = \cos \theta |H\rangle + e^{i\varphi} \sin \theta |V\rangle \quad (2.3)$$

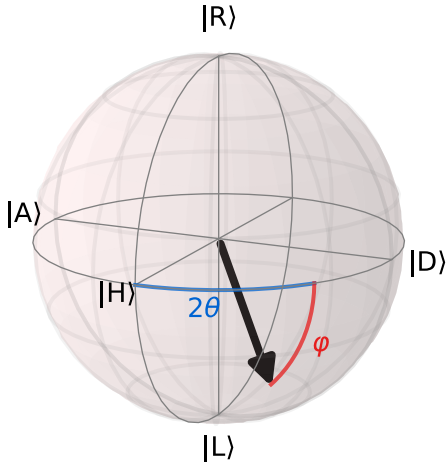


Figure 2.1: Poincaré sphere with an arbitrary polarisation state, defined via the angle  $\theta$  and circularity  $\varphi$ .

defines a point on the Poincaré sphere, as shown in Fig. 2.1. This representation is equivalent to the Bloch sphere for general qubits. In practical terms,  $\theta$  is the polarisation angle with respect to the horizontal plane and  $\varphi$  describes the degree of circularity of the light.

Finally, for later reference we also define a set of elliptical polarisation states

$$\begin{aligned} |E_{LD}\rangle &= \frac{1}{\sqrt{2}} |H\rangle + \frac{1+i}{2} |V\rangle & |E_{RA}\rangle &= \frac{1}{\sqrt{2}} |H\rangle + \frac{-1-i}{2} |V\rangle \\ |E_{LA}\rangle &= \frac{1}{\sqrt{2}} |H\rangle + \frac{-1+i}{2} |V\rangle & |E_{RD}\rangle &= \frac{1}{\sqrt{2}} |H\rangle + \frac{1-i}{2} |V\rangle, \end{aligned} \quad (2.4)$$

where  $|E_{LD}\rangle$  is exactly the bisector of  $|L\rangle$  and  $|D\rangle$ ; and the other three elliptical states are placed analogously following the same naming convention.

### 2.1.2 Entanglement

A pair of two photons is then written as the product of the two quantum states

$$|\psi\rangle = |\psi_1\rangle \otimes |\psi_2\rangle. \quad (2.5)$$

However, conversely it is possible to construct a two-photon state that is not separable, such as

$$|\phi^+\rangle = \frac{1}{\sqrt{2}} (|HH\rangle + |VV\rangle). \quad (2.6)$$

Such a state that cannot be described as a product of two independent photons is called entangled. Consequently, as famously pointed out in the Einstein-Podolsky-Rosen paradox [Ein35], a measurement of one of the two photons impacts the

quantum state of the other photon - no matter the distance between the two photons. This extreme, non-classical correlation forms the basis of many quantum applications, such as quantum computing [Eke98] or quantum teleportation [Ben93].

In Ch. 6 we interfere photons to create Bell states. In addition to the  $|\phi^+\rangle$  state above, the three other Bell states are given by

$$\begin{aligned} |\phi^-\rangle &= \frac{1}{\sqrt{2}} (|HH\rangle - |VV\rangle) & |\psi^+\rangle &= \frac{1}{\sqrt{2}} (|HV\rangle + |VH\rangle) \\ & & |\psi^-\rangle &= \frac{1}{\sqrt{2}} (|HV\rangle - |VH\rangle) \end{aligned} \quad (2.7)$$

and together form a basis of the associated Hilbert space. However, note that it has been shown to be impossible to project a two-photon pair into a Bell state with a 100 % success probability using only linear optics [Lüt99].

## 2.2 Semiconductor quantum dots as artificial atoms

A well-established method of generating highly entangled photon pairs is via spontaneous parametric down-conversion (SPDC) [Kwi95]. By sending a laser into a non-linear crystal, it is possible to randomly generate entangled photon pairs. Due to this non-deterministic process, however, there is an inherent probability of emitting multiple photon pairs at the same time. This constraint on single-photon purity thus inhibits their use in quantum applications [Wan16].

An alternative source for quantum light are single semiconductor QDs. Due to the three-dimensional energetic confinement of charge carriers in these nanometre-sized structures, QDs give rise to quantised energy states, similar to those of single atoms. Consequently, QDs are often referred to as ‘artificial atoms’. Crucially, the ability to deterministically generate single and entangled photon emission paired with monolithical on-chip integration make QDs an attractive candidate for quantum information applications [Shi07]. Substantial progress has been made in recent years, optimizing the QD emission to unseen degrees. For an extensive survey of the quantum optical properties and applications of single QDs, we refer the

reader to Refs. [Mic09] and [Tar12]. In addition, in Refs. [Buc12, Sen17, Hub18a] the engineering of QDs as near perfect sources of single and entangled photons is reviewed extensively.

### 2.2.1 Entangled photon pairs and the radiative cascade

The QD geometry of a lower, direct bandgap semiconductor embedded in a higher bandgap semiconductor creates a potential trap for electrons and holes. As a result of this three-dimensional confinement, quantised energy levels form. Depending on the exact shape of the QD, a variety of charge carrier configurations are allowed [Sei05].

The neutral exciton  $X$  consists of a single electron in the conduction band and a corresponding heavy hole in the valence band, both captured in the QD and coupled by their mutual Coulomb interaction. The electron has a spin of  $m_z = \pm\frac{1}{2}$ , while the heavy hole has a spin of  $m_z = \pm\frac{3}{2}$ . If the total spin of the two charge carriers adds to  $M = \pm 1$ , the  $X$  is optically active, and may relax to the crystal ground state  $G$  while emitting a single photon [Bay02]. The emitted photon in turn inherits the change in spin  $\Delta M = \pm 1$  in the form of left-handed  $|L\rangle$  or right-handed circular polarisation  $|R\rangle$  respectively. However, in the case of self-assembled, elongated QDs, the anisotropic exchange interaction lifts the degeneracy of the  $\pm 1$  exciton states. These split states are linear combinations of the  $\pm 1$  spin states, with a non-zero fine-structure splitting  $S$  of typically tens of  $\mu\text{eV}$ . The resulting emission polarisation is then linear instead of circular, aligned in parallel  $|H\rangle$  and orthogonal  $|V\rangle$ , respectively, to the elongation axis [Bay99, Ste02].

The biexciton state  $XX$  consists of two electrons and two holes in a double singlet configuration. Selection rules prohibit the biexciton from relaxing to the ground state directly. Instead, the biexciton decays to the neutral exciton first, before relaxing into the ground state, emitting a photon in both steps [Mor01]. This process is known as a radiative cascade, and illustrated in Fig. 2.2a.

As a result of spin conservation in the intermediate  $X$  state, two distinct decay paths are formed. Moreover, in the typical case of unpolarised emission, both

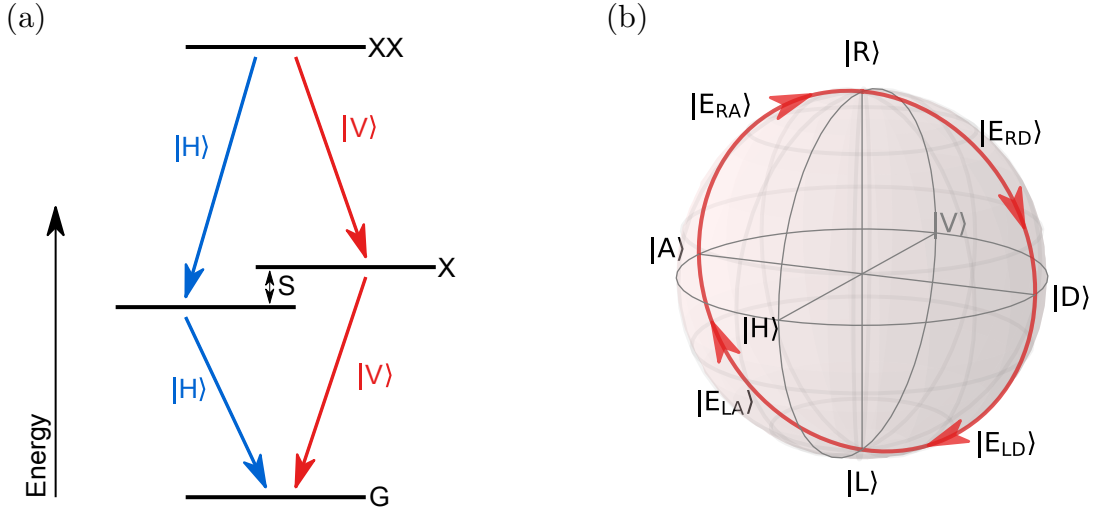


Figure 2.2: (a) Schematic diagram of the biexciton-exciton radiative cascade of a quantum dot. The exciton state is split by the fine structure splitting  $S$ . Two separate decay paths are possible, emitting either two  $|H\rangle$  or two  $|V\rangle$  polarised photons. (b) Evolution of the exciton polarisation on the Poincaré sphere for increasing time delay  $\tau$  after projection of the entangled biexciton onto a measurement polarisation.

decay paths have equal transition probabilities. Crucially, due to the superposition of the two decay paths, the two emitted photons form a polarisation entangled state [Ben00, Ste08]

$$\psi \propto \frac{1}{\sqrt{2}} \left( |H_{XX}H_X\rangle + e^{iS\tau/\hbar} |V_{XX}V_X\rangle \right). \quad (2.8)$$

This superposition state has a phase factor  $e^{iS\tau}$  depending on the fine structure splitting  $S$  and the emission time delay  $\tau$  between the two photons. When the  $XX$  photon is projected into the  $|H\rangle$  or  $|V\rangle$  state, the  $X$  polarisation remains static. However, when the  $XX$  photon is projected into an arbitrary polarisation  $(\cos\theta |H_{XX}\rangle + e^{i\varphi} \sin\theta |V_{XX}\rangle)/\sqrt{2}$ , then the  $X$  photon picks up a phase evolving with the time delay

$$\psi_{\text{evolving}} \propto \frac{1}{\sqrt{2}} \left( \cos\theta |H_X\rangle + e^{i(\frac{S\tau}{\hbar} - \varphi)} \sin\theta |V_X\rangle \right), \quad (2.9)$$

as illustrated in Fig. 2.2b. Importantly, this phase evolution by itself does not imply a decrease in entanglement, as the time-evolving two-photon state of Eq. (2.9) remains inseparable, and thus maximally-entangled [War14].

## 2.3 Characteristics of quantum light

In order to assess generated light emission, in the following we review a short selection of important metrics characterising quantum light as well as the respective optical methods to evaluate them.

### 2.3.1 Entanglement fidelity

To characterise the polarisation entanglement of a photon pair source, the polarisation-resolved second-order correlation  $g^{(2)}$  between the two photon streams needs to be measured first, as illustrated in Fig. 2.3 [Kwi95]. The two-photon second-order correlation is given by

$$g^{(2)}(\tau) = \frac{\langle n_1(t)n_2(t+\tau) \rangle}{\langle n_1(t) \rangle \langle n_2(t+\tau) \rangle}, \quad (2.10)$$

where  $n_i(t)$  are the measured photon counts at time  $t$  on detector  $D_i$  [Fox06, Buc12].

A fundamental test of entanglement is given by the Bell measurement [Bel64]. The famous Bell inequality can be evaluated according to [Cla69, You09]

$$S_{\text{Bell,HV-DA}} = \sqrt{2}(C_{\text{HV}} + C_{\text{DA}}) \leq 2. \quad (2.11)$$

Here, the  $C_\mu$  are the degrees of correlation given by (in the case of an overall unpolarised source)

$$C_\mu = \frac{g_{XX,X}^{(2)} - g_{XX,\bar{X}}^{(2)}}{g_{XX,X}^{(2)} + g_{XX,\bar{X}}^{(2)}}, \quad (2.12)$$

using the co-polarised  $g_{XX,X}^{(2)}$  and cross-polarised  $g_{XX,\bar{X}}^{(2)}$  biexciton-exciton second-order correlations, measured after projection of the photons into the respective

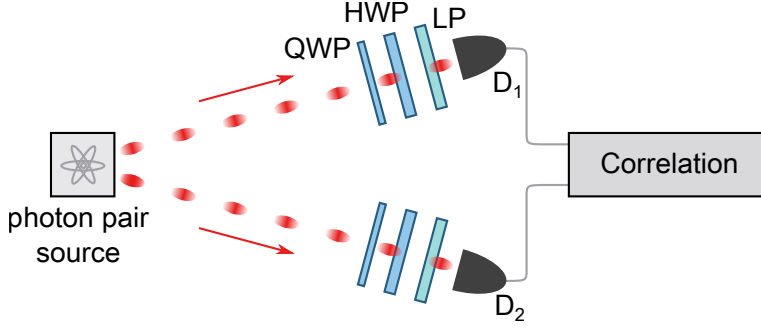


Figure 2.3: Characterising polarisation entanglement. Schematic setup to measure polarisation-resolved two-photon second-order correlation  $g^{(2)}$ . The polarisation basis of the photons is selected via a series of rotatable quarter-wave plate (QWP), rotatable half-wave plate (HWP), and linear polariser (LP) in front of the detectors ( $D_1$ ,  $D_2$ ).

polarisation basis  $\mu$  (Figs. 2.4 and 2.5a). Classically correlated particles will always satisfy this inequality, i.e.  $S_{\text{Bell}} \leq 2$ . Entangled particles, however, can violate the Bell inequality, ideally reaching a maximum Bell parameter of  $S_{\text{Bell}} = 2\sqrt{2}$ .

As described in Eq. (2.8), in the case of non-zero FSS, the phase of the entangled state evolves with increasing emission time delay  $\tau$ . Consequently, the Bell parameter can be measured with respect to this evolving set of polarisation states [War14]:

$$S_{\text{Bell,evolving}}(\tau) = \frac{1}{\sqrt{2}} \left[ 2C_{\text{HV}} + C_{\text{DA}} + C_{\text{LR}} + (C_{\text{DA}} - C_{\text{LR}}) \cos\left(\frac{S\tau}{\hbar}\right) + (C_{\text{ELD}_{\text{ERA}}} - C_{\text{ELA}_{\text{ERD}}}) \sin\left(\frac{S\tau}{\hbar}\right) \right]. \quad (2.13)$$

The result of such a Bell measurement is shown in Fig. 2.5b, along with four static Bell parameters (as defined in Eq. (2.11)).  $E_{\text{LD}}-E_{\text{RA}}$  and  $E_{\text{LA}}-E_{\text{RD}}$  are elliptical polarisation bases (offset by a  $+\pi/4$  phase from the D-A and L-R bases respectively) as indicated in Fig. 2.2b.

A full quantum mechanical representation of the entangled two-photon state is given by its density matrix  $\hat{\rho}$ . This description can be reconstructed by measuring the two-photon correlation in all polarisation basis combinations, as studied in detail in Ref. [Jam01]. Since the aim is to generate an entangled state, it is often sufficient to

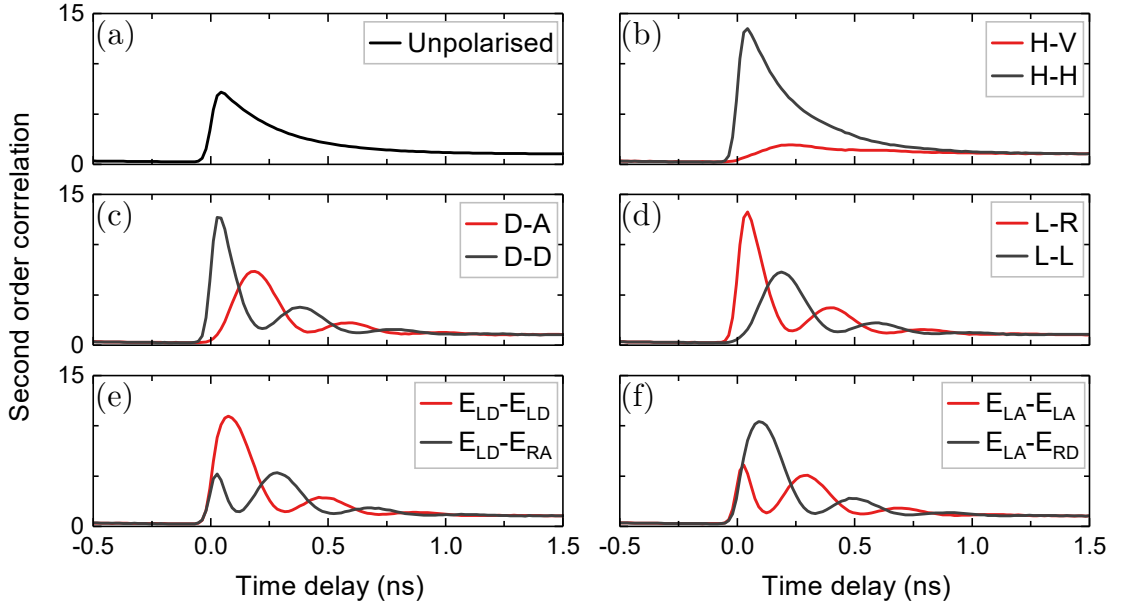


Figure 2.4: Experimental second-order biexciton-exciton cross-correlation  $g^{(2)}(\tau)$  for different polarisation bases, as a function of time delay  $\tau$  between the two photon emissions. Due to the QD FSS of  $10\mu\text{eV}$  the two-photon state oscillates with period  $S/h = 0.4\text{ ns}$ . The various co- and cross-polarised basis sets allow us to track this evolution of the two-photon state for increasing time delays. Experimentally measured on the QD device described in Chs. 3.1 and 4.1.

instead calculate the entanglement fidelity to the maximally entangled, static Bell state  $\phi^+$  of Eq. (2.7). This can be estimated as a single value  $f^+ = \langle \phi^+ | \hat{\rho} | \phi^+ \rangle$  via [Hud07]

$$f^+ = \frac{1 + C_{\text{HV}} + C_{\text{DA}} - C_{\text{LR}}}{4}, \quad (2.14)$$

For a classical, non-entangled state, the fidelity is limited to  $f^+ \leq 0.5$ , while fully uncorrelated emission yields  $f^+ = 0.25$ .

Likewise, the calculation for the entanglement fidelity can be extended to follow the evolving Bell state  $f(\tau)$ , as introduced in Ref. [War14]:

$$f(\tau) = \frac{1}{4} \left[ 1 + C_{\text{HV}} + (C_{\text{DA}} - C_{\text{LR}}) \cos\left(\frac{S\tau}{\hbar}\right) + (C_{\text{E}_{\text{LD}}\text{E}_{\text{RA}}} - C_{\text{E}_{\text{LA}}\text{E}_{\text{RD}}}) \sin\left(\frac{S\tau}{\hbar}\right) \right]. \quad (2.15)$$

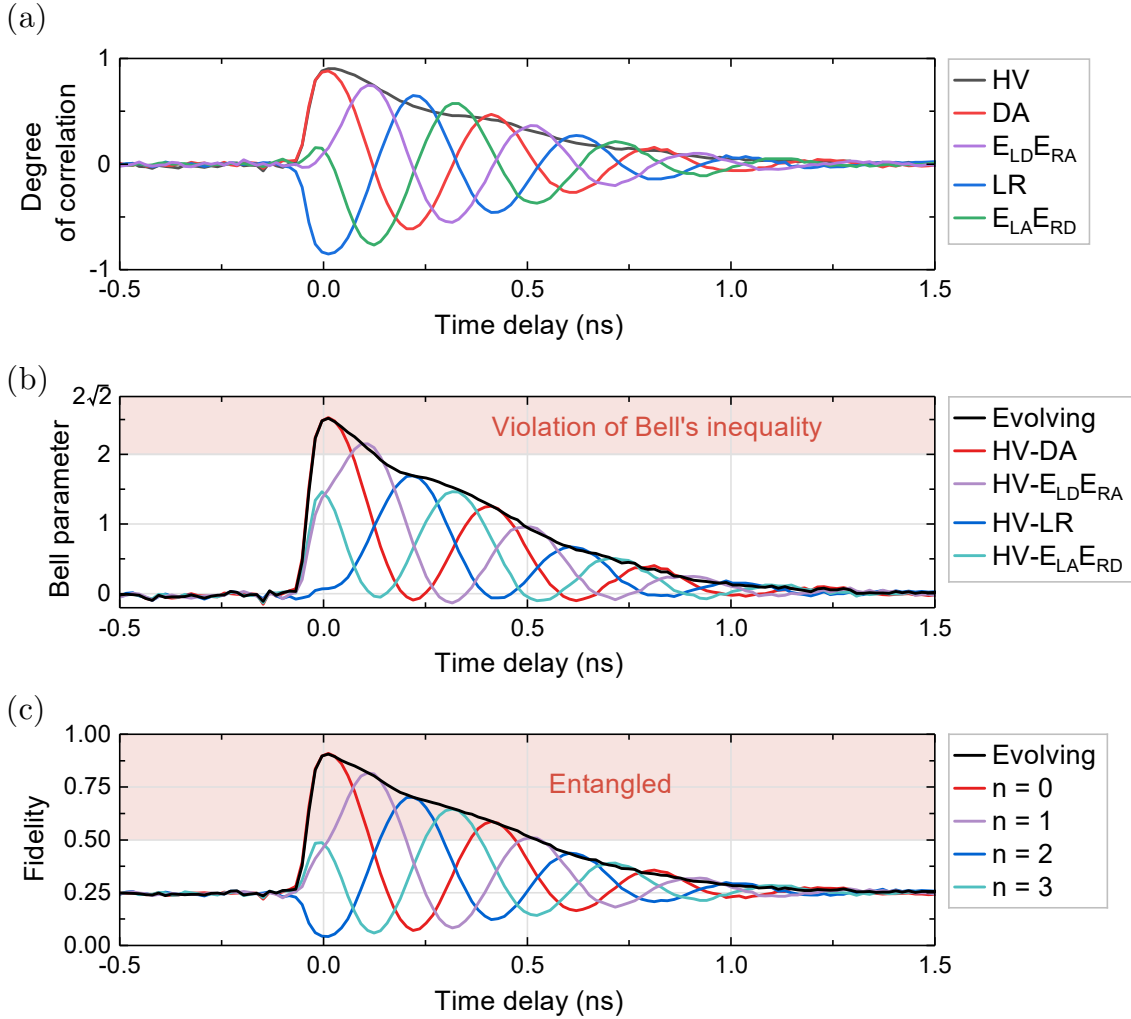


Figure 2.5: Characterising entangled light. (a) Degree of correlation for five different basis sets, via Eq. (2.12) and the experimental second-order correlations shown in Fig. 2.2b. (b) Bell parameter tests for different orthogonal basis combinations via Eq. (2.13). The Bell equality is violated for  $S_{\text{Bell}} > 2$ . (c) Fidelity to different maximally entangled Bell states, using Eq. (2.15). The two-photon state is entangled for fidelities  $f > 0.5$ . The coloured lines in this panel are the respective fidelities to the static Bell states  $[|HH\rangle + \exp(i\pi n)|VV\rangle]/\sqrt{2}$  for  $n = 0, 1, 2, 3$  [War14].

In Fig. 2.5c we can clearly see the oscillation in fidelity to the different static Bell states, as the phase of the two-photon state evolves. At the same time, the fidelity to an evolving Bell state demonstrates entanglement over multiple oscillations. The entanglement does degrade eventually—in this case chiefly due to subsequent uncorrelated emission from the continuously driven source [Ste12a]. We will investigate this phenomenon more closely in Ch. 5.

In addition, the quality of the emission is also limited by the interaction between QD and the solid state environment. Thus, to produce highly entangled photons, it is imperative to reduce detrimental processes such as valence band mixing, charge noise, and reexcitation [Lin11, Hou12, Tro14].

The Bell parameter and entanglement fidelity are only two of many ways to evaluate entanglement. Other methods are given for example by the concurrence [Woo98] or by reconstruction of the full density matrix via quantum state tomography [Jam01].

### 2.3.2 Photon statistics

The quantum nature of the emitted light may also manifest in its photon statistics. This can be investigated by performing the Hanbury Brown and Twiss experiment, as illustrated in Fig. 2.6a. The light is sent into a 50:50 beam splitter, with detectors  $D_1$  and  $D_2$  at the two output ports respectively.

The second-order correlation function again follows Eq. (2.10) [Fox06, Buc12], with the only difference in the experimental setup: Now photon emission is distributed between the two detectors randomly via a (non-polarising) beam splitter. Thus, the  $g^{(2)}(\tau)$  function measures the photon coincidences, depending on the emission time delay  $\tau$ . For an ideal single photon source, no two photons will ever be emitted at the same time  $\tau = 0$ . In that case  $g^{(2)}(0)$  will take the value 0. In contrast, a photon pair source will take the value  $g^{(2)}(0) = 0.5$ , while all classical light is limited to  $g^{(2)}(0) \geq 1$ .

The result of a typical  $g^{(2)}$ -measurement is shown in Fig. 2.7 for the  $X$  emission of a QD. The measured  $g^{(2)}(0) = 0.12 \leq 0.5$  confirms that the measured QD is indeed dominantly a single photon emitter. The non-zero  $g^{(2)}(0)$  value points to

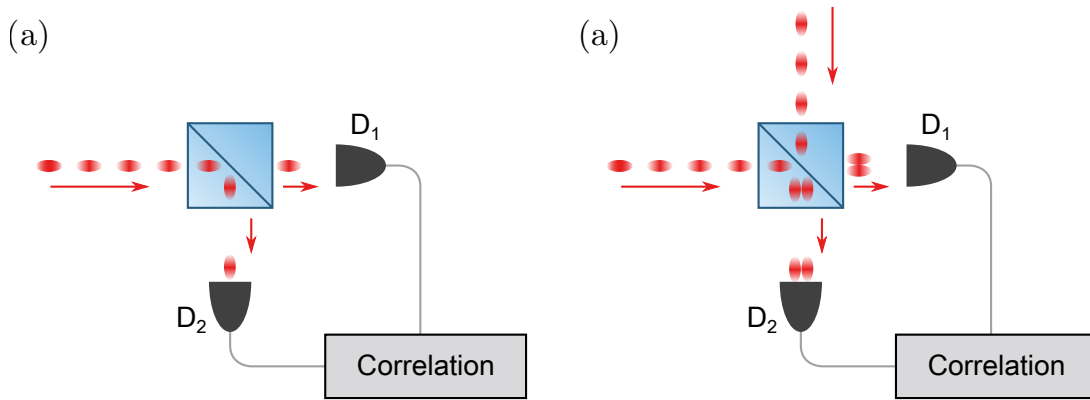


Figure 2.6: Characterising quantum light. (a) Hanbury Brown and Twiss setup to measure the second-order correlation function. (b) Hong-Ou-Mandel interferometer to measure indistinguishability.

multi-photon background emission, for example from the wetting layer (WL) or a nearby second QD, as well as a limited temporal detector resolution. For a single QD, the second-order correlation as a function of time can be simplified to (in the case of non-resonant excitation) the function [Bec01]

$$g_{\text{HBT}}^{(2)}(\tau) = 1 - A e^{-|\tau|/\tau_m}, \quad (2.16)$$

also shown in Fig. 2.7. Here,  $A$  is a parameter accounting for background contributions and  $1/\tau_m$  is the sum of the radiative decay rate and the pump rate of the system [Aha10]. In the figure the function is convolved by the Gaussian temporal instrument response function with an estimated FWHM of 100 ps before fitting. Notably, this reveals that the measured  $g^{(2)}(0)$  value is larger than the underlying photon statistics imply, as the slow instrument response time can obscure the narrow minimum at  $\tau = 0$  [Yua02].

### 2.3.3 Indistinguishability

For many quantum photonic applications such as quantum relays and quantum repeaters, it is necessary to generate indistinguishable photons. This can be tested in a Hong-Ou-Mandel experiment [Hon87], depicted in Fig. 2.6b. Two photons are sent simultaneously into a 50:50 beam splitter via the two input ports, again with

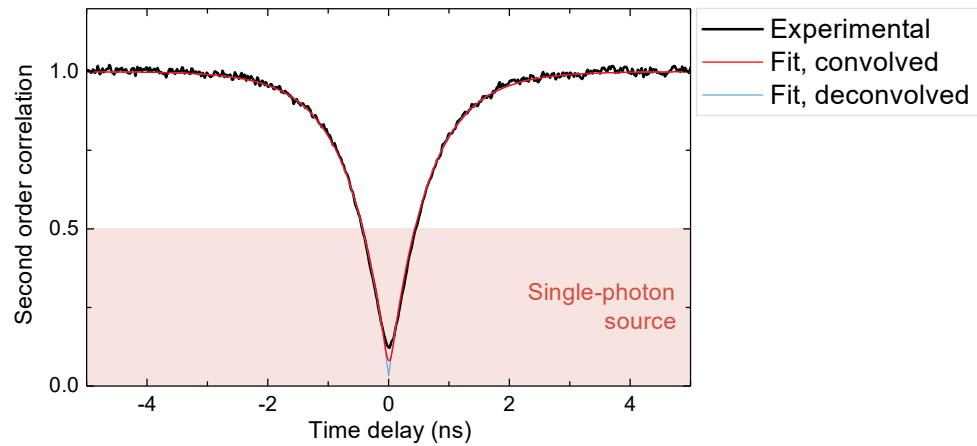


Figure 2.7: Typical HBT second-order correlation  $g^{(2)}(\tau)$  of a neutral exciton EL emission line. The value of  $g^{(2)}(0) = 0.12 \pm 0.01$  indicates dominant single photon emission. The fit function is shown with and without convolution with the 100 ps FWHM Gaussian detector response function. A  $g^{(2)}(0)$  value below 0.5 indicates the presence of a single-photon source [Buc12]. The small remaining offset between fit and experimental data is attributed to additional setup drifts. Experimentally measurement on the QD device presented in Chs. 3.1 and 4.1.

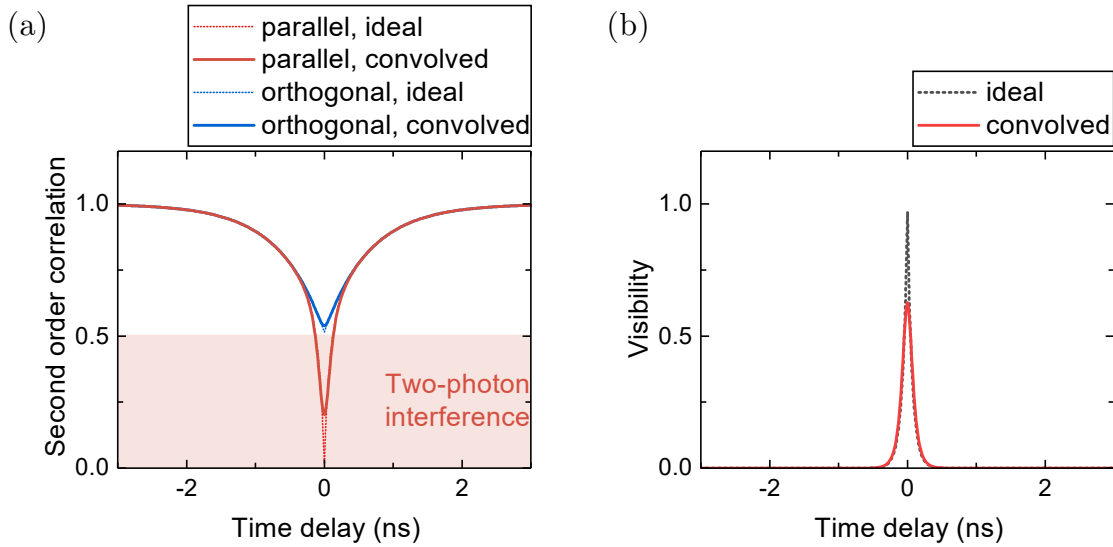


Figure 2.8: (a) Modelled Hong-Ou-Mandel second-order correlation for parallel ( $g_{\parallel}^{(2)}$ ) and orthogonally ( $g_{\perp}^{(2)}$ ) polarised photons, calculated using the HBT fitting parameters of Fig. 2.7 and for a typical coherence time of  $\tau_{\text{coh}} = 150$  ps. A value below 0.5 indicates two-photon interference. (b) Resulting two-photon interference visibility. A value above 0 indicates two-photon interference. Modelled lines are shown for an ideal instantaneous detector, and after convolution with a 100 ps Gaussian detector response.

detectors  $D_1$  and  $D_2$  at the two output ports. If the two photons are indistinguishable, the probability amplitudes of the two wave functions fully interfere such that both photons are only allowed to exit from the same output port. Hence, in the case of a complete overlap of the two wave functions, the photons will register only on either of the two output ports, but not on both at the same time.

For two identical photons with exponentially decaying envelope functions (such as emitted from QDs) and parallel polarisations impinging on the beam splitter, the probability of detecting a photon at both output ports, as a function of detection time delay  $\tau$ , is given by [Leg03, Nil13]:

$$P_{\parallel}(\tau) = \frac{1}{2}(1 - e^{-2|\tau|/\tau_{\text{coh}}}), \quad (2.17)$$

where  $\tau_c$  is the coherence time of the photons.

For two separate sources of the same wavelength and normalised relative intensities  $\eta_1$  and  $\eta_2$ , the second order correlation function is then given by [Pat10]

$$g_{\parallel}^{(2)}(\tau) = \frac{\eta_1^2}{(\eta_1 + \eta_2)^2} g_{1,\text{HBT}}^{(2)}(\tau) + \frac{\eta_2^2}{(\eta_1 + \eta_2)^2} g_{2,\text{HBT}}^{(2)}(\tau) + \frac{2\eta_1\eta_2}{(\eta_1 + \eta_2)^2} P_{\parallel}(\tau), \quad (2.18)$$

where  $g_{1,\text{HBT}}^{(2)}(\tau)$ ,  $g_{2,\text{HBT}}^{(2)}(\tau)$  are the second-order autocorrelations of the two sources as defined in Eq. (2.10), and  $\eta_1$  and  $\eta_2$  are their respective relative intensities. The first two terms describe the case where one or the other source emits two photons at the given time delay. The third term describes the case where both source emit a photon, leading to the desired two-photon interference.

If the photons of the two sources are made to be distinguishable, often by rotating the polarisation of one of the two sources to an orthogonal polarisation, then the probability of two photons exiting opposite output ports becomes

$$P_{\perp}(\tau) = \frac{1}{2}. \quad (2.19)$$

In turn the resulting second order correlation function becomes

$$g_{\perp}^{(2)}(\tau) = \frac{\eta_1^2}{(\eta_1 + \eta_2)^2} g_{1,\text{HBT}}^{(2)}(\tau) + \frac{\eta_2^2}{(\eta_1 + \eta_2)^2} g_{2,\text{HBT}}^{(2)}(\tau) + \frac{\eta_1\eta_2}{(\eta_1 + \eta_2)^2}. \quad (2.20)$$

Figure 2.8a shows the modelled two-photon second order correlation for parallel and orthogonally polarised photon sources, demonstrating the effect of two-photon interference in the parallel case.

The indistinguishability is then commonly evaluated via the interference visibility, defined by

$$M_{\text{HOM}}(\tau) = 1 - \frac{g_{\parallel}^{(2)}(\tau)}{g_{\perp}^{(2)}(\tau)} \quad (2.21)$$

and shown in Fig. 2.8b. A fully indistinguishable source (leading to complete two-photon interference) yields the value  $M_{\text{HOM}}(0) = 1$ . In particular, the figure highlights the pronounced effect of finite detector response functions on the measured interference visibility.

## 2.4 Tailoring the quantum dot emission

A fundamental advantage of QDs over other emitter systems is their entirely artificial fabrication. As a result, the major characteristics can be engineered towards desired requirements by adjusting the involved parameters such as material system, morphology, and experimental conditions.

### 2.4.1 Initialisation of the quantum dot state

In order to initialise the QD into the desired state, the corresponding charge carriers need to be captured in the dot. The standard method of generating charge carriers at the QD is via optical excitation using a pulsed or continuous wave laser. In-depth comparisons between different optical excitation schemes are presented in Refs. [Fog17] and [Hub18a].

In above-band excitation, the emission energy of the excitation laser is chosen to be larger than the GaAs bandgap. Thus, electron-hole pairs are generated by optical absorption in the wetting layer or bulk GaAs near the QD. The charge carriers are subsequently captured by the QD, relaxing non-radiatively to an available exciton or biexciton state. While this scheme is simple to employ, the resulting QD state suffers from dephasing due to charge noise, limiting the entanglement fidelity [Mül14, Kuh15]. Excess charge carriers also lead to undesirable reexcitation from the exciton state back to the biexciton state [Tro14].

In quasi-resonant excitation, the laser is tuned to a higher shell of the exciton state, such that it relaxes non-radiatively into the lowest exciton shell. This technique reduces dephasing from charge noise and reexcitation [Mic09]. However, due to the finite relaxation time, it still suffers from timing jitter, and thus reduced indistinguishability [Kir17, Hub18a].

In resonant excitation, the excitation laser is tuned to match the transition energy of the desired QD state. However, selection rules prohibit the biexciton from being excited directly from the ground state. To address this, the biexciton needs to be initialized via a resonant two-photon excitation (TPE) process. That means

tuning the laser to the centre between biexciton and exciton energy. Only then, the exciton can be excited resonantly, absorbing two laser photons simultaneously. Tuning the pulsed laser intensity to match a  $\pi$ -pulse [Fox06], the biexciton population can be reliably initialized to near 100% [Mül14]. While more complex to set up, the benefits of this excitation scheme are on-demand generation of photons, as well as reduced timing jitter and charge noise. Recently, Reindl et al. [Rei18] have employed this approach to perform quantum teleportation in a quantum relay setup. With an entanglement fidelity to the static Bell state of  $0.925 \pm 0.003$ , the authors demonstrated successful quantum teleportation with an average fidelity of  $0.75 \pm 0.02$ . Finally, recent advances in resonant TPE are surveyed more extensively in Ref. [Hub18a].

An alternative to optical excitation is electrical excitation [Ben00, Yua02, Sal10]. Charge carriers are supplied by applying an electrical current through the QD, by embedding the emitters in a diode-like electrical structure. Similarly to above-band excitation, an electron and a hole are then captured in the QD, forming an exciton. Electrical excitation has a unique set of benefits over optical excitation. Most importantly, the complexity of the excitation setup is vastly reduced, eliminating obstacles such as fluctuations in laser intensity or resonance conditions entirely. Recently, electrically generated entangled photons have been used successfully for the operation of a long-distance quantum relay, achieving a post-processed teleportation fidelity of  $0.900 \pm 0.027$  over a total of 1 km of fibre [Var16]. At the same time, the non-resonant electrical excitation process inhibits the emission quality due to dephasing and reexcitation mechanisms [Ste12b]. Nevertheless, resonant electrical excitation schemes [Ben00] and close control of the electrical timing have been proposed to reduce these detrimental processes [Kan17]. Finally, the compact integration without the need for a complex excitation laser system presents a clear path to realizing industry compatible devices.

### 2.4.2 Tuning the emission energy

Due to the random nature of self-assembled QD formation, the emission wavelengths in any ensemble of QDs exhibits an inhomogeneous broadening over tens of meV. In future applications such as quantum relays and quantum repeaters, however, it may become necessary to interfere photons from different sources, requiring an almost perfect overlap in wavelength.

In order to gain the ability of tuning the QD emission wavelength, different approaches have been implemented. The most well-established approach is the fabrication of electrical contacts above and below the QD [War00]. The back gate is realized during growth, by depositing a heavily doped layer before depositing the QDs. Using the electrical gates to generate an electric field in growth direction, the emission energy is shifted via the quantum-confined Stark effect [Fry00b]. Bennett et al. [Ben10a] have shown that an additional tunneling barrier between the QD and the electrical gates can extend the accessible Stark shift range to more than 10 meV before the charge carriers tunnel out of the QD.

In electrical excitation, supplying a current inherently involves changing the voltage potential across the QD, inducing a Stark shift. A recent implementation in Ref. [Lee17] has decoupled this relationship by performing the electrical injection in an independent pumping mesa next to the QD device. The generated light is emitted laterally, and excites the QD in the neighboring tuning mesa. This implementation demonstrates the possibility to electrically tune emission intensity and emission wavelength independently.

Another area of interest is the control of the fine-structure splitting (FSS) in the QDs. As mentioned in section 3.1.1, the anisotropic exchange interaction leads to a FSS in the  $X$  state. Although the presence of FSS does not inherently limit the entanglement fidelity of the emission, non-zero FSS requires a high temporal detector resolution and either post-processing of the measurement data, or additional measurement steps involving elliptical polarisation bases, as shown in Eq. (2.15) [Hud07, War14]. A variety of methods to control the FSS have been demonstrated,

applying an external perturbation to the QD, such as electric fields [Ger07, Ben10b], magnetic fields [Hud07] or strain [Sei06]. As demonstrated by Trotta et al. [Tro12], simultaneous control over two independent external perturbations is sufficient to eliminate the FSS of an arbitrary quantum dot. By adding control over a third degree of freedom, for example via three independent piezo actuators, the QD emission energy can be tuned in addition to maintaining the exciton degeneracy [Tro16]. Recently, Huber et al. [Hub18b] have employed such a strain-tunable device together with resonant TPE to generate near maximally entangled photons with a fidelity of  $0.978 \pm 5$  without temporal post-selection.

### 2.4.3 Extraction efficiency

A key requirement for quantum photonic applications is a high emission intensity of the source. Naturally, the QD emits isotropically in all directions [Sen12]. Combined with the strong internal reflection at the semiconductor surface, this means that a standard microscopy setup would collect less than 1% of the emitted light. The theoretical foundations for understanding and enhancing the collection efficiency are discussed extensively in Ref. [Bar02]. In the following, we discuss two main approaches: solid immersion lenses and optical cavities.

The first approach is the use of high refractive index solid immersion lenses (SILs) placed directly onto the sample. This geometry allows a larger cross-section of light to exit the semiconductor. Recently, Chen et al. [Che18] have investigated the influence of an intermediate, lower refractive index layer between semiconductor and SIL on the QD emission profile. By using a PMMA layer of 100 nm, the authors were able to achieve a current record collection efficiency of  $(65 \pm 4)\%$  at the first collection lens. Furthermore, an entanglement fidelity of  $0.90 \pm 0.03$  was reported, using resonant TPE.

Microlenses extend the concept of SILs. Instead of attaching the SIL onto the sample after fabrication, a micrometre-sized lens is patterned using an in-situ (with the sample in the cryostat) cathodoluminescence lithography technique [Gsc13, Gsc15]. This approach combines deterministic fabrication and precise spacial selectivity.

Bounouar et al. [Bou18] have recently used microlenses to demonstrate entangled light generation with an extraction efficiency of  $(8.4 \pm 1.0) \%$  per photon. A resulting entanglement fidelity of  $0.73 \pm 0.03$ , via resonant TPE, was reported.

The second approach is the use of cavities to direct the quantum dot emission into predefined optical modes. By embedding the quantum dot in between two distributed Bragg reflectors (DBRs), a simple planar cavity is created. The distance between the two DBRs is required to be an integer multiple of half the QD wavelength [Bab92].

The concept of micropillars takes this approach further by restricting the optical modes in lateral direction as well [Pel03], in addition to the vertical confinement via the DBRs. Due to the Purcell effect, the spontaneous emission rate together with the emission efficiency is increased significantly [Bar02]. A sophisticated fabrication process is necessary to etch vertical micropillars of the desired size and containing a single quantum dot. Nevertheless, this design has been shown to routinely enable emission efficiencies above 70%, together with both, near perfect single photon purity and indistinguishability [Din16, Som16, Uns16]. Additionally, this approach has been shown to be compatible with electrical tuning [Now14] and electrical excitation [Böc08, Sch16]. However, a major restriction is the narrow spectral coupling range of a micropillar. As a consequence, the optical mode in the micropillar cannot couple to the biexciton and exciton emission line simultaneously. A solution has been presented by Dousse et al. [Dou10]: By employing a double micropillar design with the quantum dot in one of the two pillars, the biexciton and exciton emission couple into two separate optical modes. As a result, the authors reported an unprecedented collection efficiency of 34% per photon, with an entanglement fidelity of 0.67. However, no further advances using this double micropillar design have been reported since, likely owed to the difficulty of matching the QD emission wavelength to cavity resonance.

Finally, large progress has been made recently using so-called bull's-eye cavities. As indicated by the name, the cavity is formed by etching a number of rings into the semiconductor, concentric around the position of the QD. These rings act as

a circular DBR mirror, laterally confining the emitted light. By suspending this structure as a thin membrane on top of a low-index material (such as SiO<sub>2</sub>) followed by a gold mirror, a large fraction of the overall emission is then refracted vertically towards the collection lens. Using this strategy, Liu et al. [Liu19] and Wang et al. [Wan19] achieved record photon pair extraction efficiencies of  $(65 \pm 4) \%$  and  $(59 \pm 1) \%$  respectively, coupled with significant Purcell enhancement.

#### 2.4.4 Emission wavelengths

The wide choice of material system and quantum dot morphology enables emission in different spectral wavelength ranges. Most well-established are In(Ga)As QDs on GaAs, which naturally emit in the NIR wavelength range from 850 nm to 970 nm [Sen17]. This is reflected in excellent optical properties, such as long coherence times, background free emission, and strong entanglement [Kuh15, Din16, Han18, Wan19]. Consequently, this was the material of choice for the QDs employed in this work.

Rapid advances have been made recently in extending quantum dot emission wavelengths to the telecommunication O- and C-bands around 1310 nm and 1550 nm respectively [Huw17, Pau17, Mül18]. These wavelengths are of special interest for applications in quantum communication due to their lower transmission losses in optical fibre. In order to produce quantum dots emitting at telecom wavelengths, different growth methods have been developed. Successful generation of telecom O-band, entangled photons has been shown for InAs QDs grown on an InGaAs strain relaxation layer [War14, Huw17]. In the telecom C-band, Olbrich et al. [Olb17] have used InAs dots on a metamorphic InGaAs buffer layer for the generation of entangled photons, while Müller et al. [Mül18] have employed InAs droplets grown on an InP substrate to demonstrate the same.

Finally promising results have recently been demonstrated using droplet-etched GaAs/AlGaAs QDs on a GaAs substrate [Huo13, Hub17]. This system offers the possibility of low FSS due to reduced strain and enhanced symmetry of the QD shape, as well as faster radiative recombination rates compared to other types of

QDs. Notably, these factors have been leveraged for the first demonstrations of entanglement swapping using solid-state quantum emitters [Bas19, Zop19].

## 2.5 Quantum key distribution

Quantum key distribution allows two users to create a shared, provably secure private key via a public channel, a task that is impossible via exclusively classical communication [Ben84, Lo99, Gis02]. Instead, classical public key encryption schemes rely on unproven assumptions about the complexity of mathematical algorithms and estimates of an attacker's computational prowess for computational security [Nie10]. In the following we briefly introduce some of the experimental concepts in QKD that are relevant to the results presented in this work.

### 2.5.1 BB84 protocol

The first, but still widely used QKD protocol is BB84 [Ben84]. As introduced in Ch. 2.1.1, information can be encoded in the polarisation of a photon. In the four-state BB84 protocol, we assign the polarisation states  $|H\rangle$  and  $|D\rangle$  the binary value 1, and the states  $|V\rangle$  and  $|A\rangle$  are assigned the value 0. In a first step the sender, typically called Alice, sends a sequence of single photons with polarisation chosen at random among the four states. The receiver, Bob, in turn measures the photon polarisation in either the rectilinear or the diagonal basis, once again chosen at random. If the photon state matches the measurement basis, Bob will measure the correct polarisation and thus binary value with probability 1.

If Bob chooses the wrong measurement basis, he will only have a random 50% chance to yield the correct binary value. Thus, in a step called basis reconciliation, Alice and Bob then share their chosen measurement bases via a classical, public channel. Subsequently, they discard bits where different polarisation bases were chosen, such that the remaining bits are generated and measured in the same basis.

Importantly, they would be able to detect an adversary attempting to eavesdrop on the key exchange. By comparing a substring of the generated key, they can estimate

the quantum bit error rate (QBER). As the no-cloning theorem prohibits the faithful copying of qubits, an attacker listening in on the key exchange would be unable to fully hide their tracks. Additional post-processing of the key by Alice and Bob ensures that any potential attacker is detected [Gis02, Cha02, Fun10, Xu20]. Although the original proposal required true single photon sources to ensure unconditional security, the decoy state technique [Hwa03] allows for the use of weak coherent pulses (WCPs) that occasionally contain multiple photons, such as produced by a weak laser. Using this technique, secure quantum bit rates beyond 10 Mb/s have been achieved [Yua18]. Nevertheless, the use of WCPs substantially inhibits the attainable key rates, offering the potential for multi-fold key rate improvements when instead using true single photon sources such as quantum dots [Wan08, Cha20, Kup20].

### 2.5.2 Entanglement-based QKD

Another quantum mechanical resource for QKD is entanglement [Eke91]. In the BBM92 protocol [Ben92], a third party Charlie sends one photon each of a polarisation-entangled photon pair (e.g.  $|\psi^+\rangle$ , see Eq. (2.7)) to the communicating parties Alice and Bob respectively. Subsequently, Alice and Bob randomly and independently measure their photons in either the diagonal or rectilinear basis, again with an  $|H\rangle$  and  $|D\rangle$  result representing 1 and vice versa. During basis reconciliation, bits where Alice and Bob chose different bases are discarded. If the resulting QBER is low enough, they can be sure to share an unconditionally secret key.

Notably, this protocol is source-independent [Ben92]. Even if an adversary hijacked the photon pair source of Charlie and sent out arbitrarily manipulated photon pairs, Alice and Bob would always be able to detect this tampering in the resulting QBER and recognise the attack. This protocol lends itself naturally to entangled photon pairs generated from quantum dots, as demonstrated in Refs. [Dzu15, Bas21, Sch21]. To this end, in Ch. 5 we briefly evaluate the results on efficient generation of entangled photon pairs w.r.t. the resulting QBER in entanglement-based QKD.

### 2.5.3 Measurement-device-independent QKD

In contrast to source-independent QKD schemes such as the BBM92 protocol, other protocols instead focus on measurement-device-independence [Lo12, Xu15, Xu20]. This is particularly attractive because it is often the measurement device that is the most complex and costly part of the setup, offering the highest potential for side channel attacks. In the measurement-device-independent (MDI) QKD protocol proposed by Lo et al. [Lo12], Alice and Bob each prepare a photon pulse with polarisation chosen randomly among  $|H\rangle$ ,  $|D\rangle$ ,  $|V\rangle$ ,  $|A\rangle$ . As illustrated in Fig. 2.9, the two photons are then sent to Charlie. If Alice and Bob chose the same polarisation basis, then the two photons interfere on Charlie's beam splitter, thus becoming entangled.

With the illustrated setup it is then possible to measure either the  $|\psi^+\rangle$  or  $|\psi^-\rangle$  Bell state. The measurement result is publicly announced by Charlie, revealing the parity of the two bits sent by Alice and Bob. As is easily verified, following Table 2.1 Bob may then flip his bit depending on the chosen polarisation bases and the measured Bell state in order to form a shared secret key with Alice.

	$ \psi^+\rangle$ Bell state	$ \psi^-\rangle$ Bell state
Rectilinear basis	Bit flip	Bit flip
Diagonal basis	No bit flip	Bit flip

Table 2.1: Parity table according to chosen polarisation bases and measured Bell state. Alice and Bob post-select the bits where they chose the same polarisation basis (rectilinear or diagonal) and a successful BSM was announced. Bob then flips his bit accordingly.

This QKD scheme is in effect equivalent to a time reversal of the BBM92 scheme described in the previous section [Xu20]. Instead of Charlie generating an entangled pair to be measured by Alice and Bob, in MDI QKD Alice and Bob generate the two photons, which are then entangled and measured by Charlie. As the BSM only reveals the parity of the two bits, he cannot infer the absolute value of the secret key.

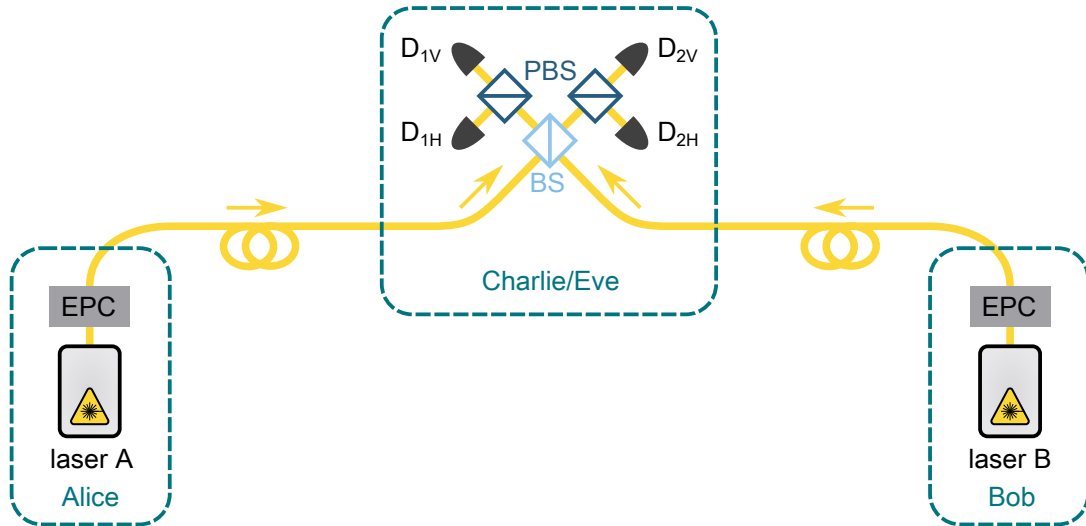


Figure 2.9: (a) Bell state measurement for MDI QKD. Alice and Bob each send a laser pulse with polarisation randomly chosen among  $|H\rangle$ ,  $|D\rangle$ ,  $|V\rangle$ ,  $|A\rangle$ . Charlie/Eve then performs a Bell state measurement (BSM), with simultaneous clicks on detectors  $D_{1H}$  and  $D_{1V}$ , or on  $D_{2H}$  and  $D_{2V}$  signifying projection onto the  $\psi^+ = (|HV\rangle + |VH\rangle)/\sqrt{2}$  Bell state, while simultaneous clicks on  $D_{1H}$  and  $D_{2V}$ , or on  $D_{2H}$  and  $D_{1V}$  indicate the  $\psi^- = \frac{1}{\sqrt{2}}(|HV\rangle - |VH\rangle)$  Bell state. The resulting Bell state indicates the parity of the bits sent by Alice and Bob, allowing them to infer a shared key, secret from Charlie/Eve according to table 2.1.

Crucially, Alice and Bob are able to recognise a dishonest Charlie (i.e. infiltrated by Eve) via the resulting QBER.

The transmission rate in MDI-QKD at short distances is reduced compared to the standard BB84 protocol, as Alice and Bob need to post-select bits with a successful BSM in addition to them choosing the same polarisation basis. Nevertheless, the MDI-QKD turns out to be more robust to noise, enabling longer communication distances than possible via BB84 [Yin16]. In addition, Xu et al. [Xu13] have proposed the addition of a SPDC entangled photon pair source into the protocol for a further extension of the communication distance. In Ch. 6 we theoretically investigate a closely related setup using E-LEDs as an entangled pair source instead.

## 2.6 Quantum repeaters

Finally, a solution to extend quantum communication distances to arbitrary distances is the concept of quantum repeaters [Bri98, San11]. These combine entangled photon pair sources with quantum memories and entanglement distillation to distribute entanglement across arbitrary distances. This is done by iterative short-distance distribution of entanglement between neighbouring nodes, which is then teleported towards the end points via repeated entanglement swapping. Thus, these quantum repeaters can act as untrusted nodes along an arbitrarily long quantum communication channel, maintaining the unconditional secrecy of the transmitted information.

Experimental implementations of a functional quantum repeater have so far remained elusive, although continuous advancements towards a real world implementation have been demonstrated [Cho07, Yua08, Gao12, Kal17a, Bha20].

## 2.7 Summary

In this chapter we presented a brief introduction to some of the relevant frameworks in quantum information. We introduced photons as polarisation qubits and described the use of the radiative cascade in quantum dots to generate polarisation entangled

photon pairs. Throughout this work we rely on the subsequently presented methods to characterise different aspects of quantum light. Altogether, the fast progress and large interest in the fields of quantum information and quantum photonics underlines their promising capabilities for the future. With QKD on the verge of wide-scale deployment, the benefits of such novel technologies is becoming tangible to the every day user.



# 3 | Experimental techniques

After introducing the fundamental framework and mechanism of entangled light generation from quantum dots in the previous chapter, this chapter introduces the experimental techniques to electrically generate single and entangled photons from a QD-LED. In section 3.1 we describe the considerations behind the sample design. In addition to details on the electronic structure and optical cavity, this includes a description of the growth methods and microfabrication techniques to manufacture such a device. This is followed in section 3.2 by a description of the optical measurement setup in order to operate and measure such a QD-LED. There, we also present a deterministic method of recovering the natural polarisation eigenbasis of the QD emission transmission through an optical fibre.

## 3.1 Sample design and fabrication

The epitaxial growth of semiconductor QDs has been demonstrated for a diverse set material systems and growth techniques [Joy04, Sch12]. For the work presented in this thesis we employ strain-grown InAs QDs on GaAs, motivated in particular by the high optical emission quality associated with this method [Kuh15, Din16, Han18, Wan19].

### 3.1.1 Stranski-Krastanov growth of InAs quantum dots

InAs QDs are most commonly grown by employing the Stranski-Krastanov growth mode on a (100)-oriented GaAs substrate [Str37, Bim01, Sau20]. This approach leverages the semiconductor lattice mismatch (in this case 7%) between QD material and substrate. In a first step, a small number of typically 1–2 monolayers of the QD material is deposited on the substrate, forming a uniform 2D layer (Figs. 3.1a

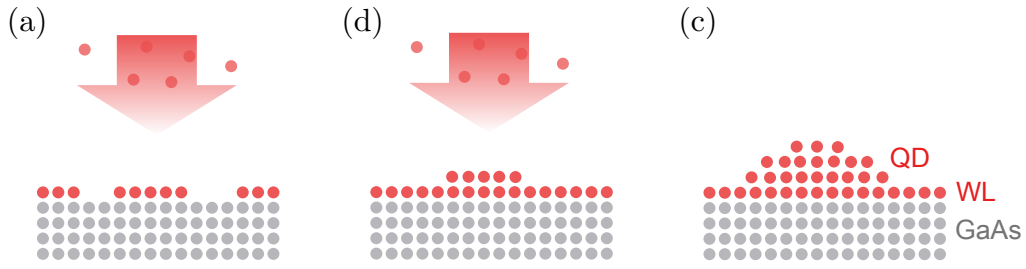


Figure 3.1: Schematic illustration of the Stranski-Krastanov mode during MBE growth. (a) InAs (red) is evaporated onto a GaAs buffer (grey). (b) An atomically thin wetting layer forms. (c) When the wetting layer (WL) surpasses the critical thickness, the InAs organises in islands to reduce strain, forming quantum dots on top of the wetting layer.

and 3.1b) [Ven01, SS17]. In this so-called wetting layer, the lattice mismatch induces a lateral strain. When the wetting layer surpasses a critical thickness, the lateral strain increases to the point where, instead of uniform monolayers, the formation of islands located on top of the 2D layer becomes energetically favourable (Fig. 3.1c) [Str37]. By closely monitoring this transition between 2D layer and confined islands, the size of the QDs can be controlled. The newly formed QDs are then capped in GaAs. Figure 3.2 shows a characteristic emission spectrum from a wafer containing only a layer of SK QDs. The emission from the dots at wavelengths longer than 880 nm is clearly quantised. In contrast, the wetting layer emission at shorter wavelengths produces a continuous spectrum.

Quantum dots grown using this growth method are typically elongated along the (110) crystal axes. Due to the anisotropic exchange interaction, this asymmetry results in a non-zero fine structure splitting (FSS) of the neutral exciton state [Gam96]. However, the amplitude of the FSS correlates with the confinement energy of the quantum dot [You05], empirically exhibiting values of less than  $5\mu\text{eV}$  around an exciton emission wavelength of  $\sim 885\text{ nm}$ .

A variety of alternative growth techniques allow for the creation of quantum dots as well. One example is growth via droplet epitaxy. Originally proposed to enable growth of more symmetric QDs on the (111)-surface, this method has been reported

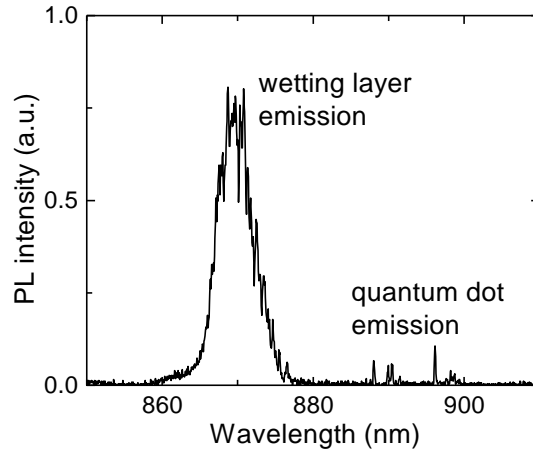


Figure 3.2: Typical photoluminescence (PL) spectrum of a strain-grown quantum dot. Excited via a 780 nm laser diode with the sample at 4.2 K. The quantum dot emission is quantised while the two-dimensional wetting layer produces a continuous emission spectrum.

to enhance QD symmetry on the (100) surface as well [Sch09, Kur13, SS17]. Finally, other examples of recent progress include droplet etching [Huo13, Kei17] and high-temperature droplet epitaxy [Bas18]—each of these growth methods having their own unique set of characteristics.

### 3.1.2 Design of the distributed Bragg reflector

As highlighted in Ch. 2.4.3, the emission efficiency of the QD sample may be enhanced via different approaches. For the samples in this work, we employ planar  $2\lambda$  microcavities made up of typically 6 (18) DBR repeats above (below) the QD layer. Each DBR repeat in turn consists of a pair of Al(Ga)As and GaAs layers with a respective thickness  $d$  of [Bab92]

$$d_{\text{Al(Ga)As/GaAs}} = \frac{\lambda_0}{4n_{\text{Al(Ga)As/GaAs}}}, \quad (3.1)$$

where  $\lambda_0$  is the design wavelength in vacuum and  $n$  is the respective refractive index at the cryogenic operation temperature. When the DBR pairs fulfil this relation, light reflected vertically off the interfaces between the DBR layers interferes constructively, forming an effective mirror for a wavelength range (‘stop band’) around the design

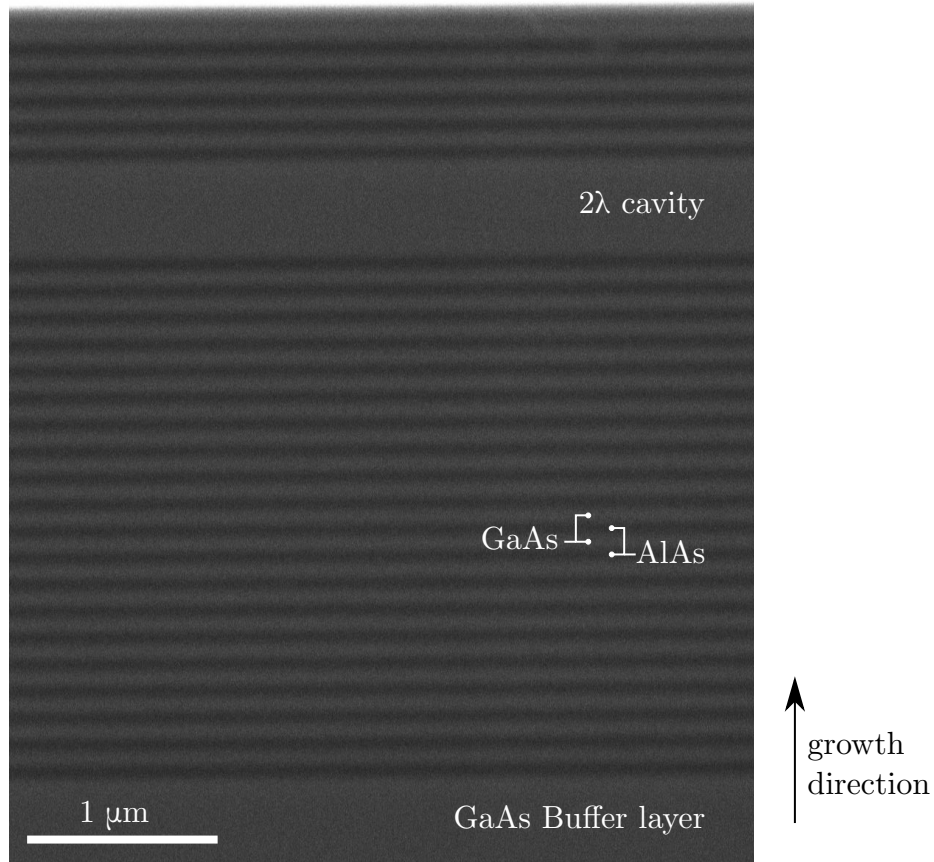


Figure 3.3: Cross-sectional scanning electron microscopy (SEM) micrograph of a cleaved planar microcavity structure, revealing the alternating GaAs/AlAs layers constituting the top and bottom DBR. The quantum dot layer (not resolved here) is grown in the centre of the  $2\lambda$  cavity.

wavelength. The bandwidth  $\Delta\lambda$  of this stop band is given by [Yar89]

$$\Delta\lambda = \frac{\lambda_0}{\pi} \left( n_{\text{Al(Ga)As}} + n_{\text{GaAs}} \right) \left( \frac{1}{n_{\text{Al(Ga)As}}} - \frac{1}{n_{\text{GaAs}}} \right), \quad (3.2)$$

yielding  $\Delta\lambda = 100$  nm for a design wavelength of  $\lambda_0 = 885$  nm at 20 K and an AlAs/GaAs DBR.

Fig. 3.3 shows a cross-sectional SEM micrograph of a full sample structure, resolving the alternating pairs of GaAs and Al(Ga)As in the top and bottom DBR with the  $2\lambda$  GaAs cavity in between. Careful analysis of the micrograph along with statistical

averaging across the highly repetitive layer structure allows for ex-situ monitoring of the MBE DBR growth process.

In order to optically characterise the grown QDs and DBR, we employ a confocal microscopy setup, shown in Fig. 3.4. The sample is mounted in a windowed Helium flow cryostat and cooled to 4 K. To measure the reflectivity spectrum, we illuminate the sample with a broadband near-infrared (NIR) LED. A commercial apochromatic objective mounted outside the cryostat focusses the light to a micrometre-sized spot on the sample surface. The reflectivity spectrum of the DBR structure is highly dependent on the angle of the light impinging on the sample. The larger the numerical aperture of the objective, the smaller the contrast of the features in the reflectivity spectrum. A variable iris allows us to change the beam diameter of the broadband LED after collimation, in turn effectively controlling the numerical aperture of the objective. For photoluminescence (PL) measurements, we use a 780 nm continuous wave (CW) laser diode for above-band excitation, focussed on the sample through the same apochromatic objective. Finally, the reflection and emission spectra are measured in a spectrometer with a diffraction grating of either 600 lines/mm or 1800 lines/mm and a liquid-nitrogen-cooled charge-coupled device (CCD).

A typical reflectivity spectrum of an MBE-grown sample with DBR cavity is shown in Fig. 3.5(a). Due to the limited optical bandwidth of the NIR LED and the spectrometer, the spectral measurement often does not cover the entirety of the stop band. The red line shows a numerical simulation using a transfer-matrix method, reproducing the shape of the experimental spectrum. The simulated spectrum enables fast identification of the features in the experimental spectrum, in particular the wavelength of the cavity resonance and the bandwidth of the stop band.

Fig. 3.5(b) shows a corresponding PL spectrum, measured on the same sample and driven at a low excitation power of  $5\ \mu\text{W}$  via the 780 nm laser diode. The emission is strongly enhanced at wavelengths near the cavity resonance. The quantised emission lines in turn indicate the successful formation of QDs. The spatial density of the QDs can be estimated by tracking the appearance and disappearance of emission lines while laterally moving across the sample. Notably, both DBR cavity resonance

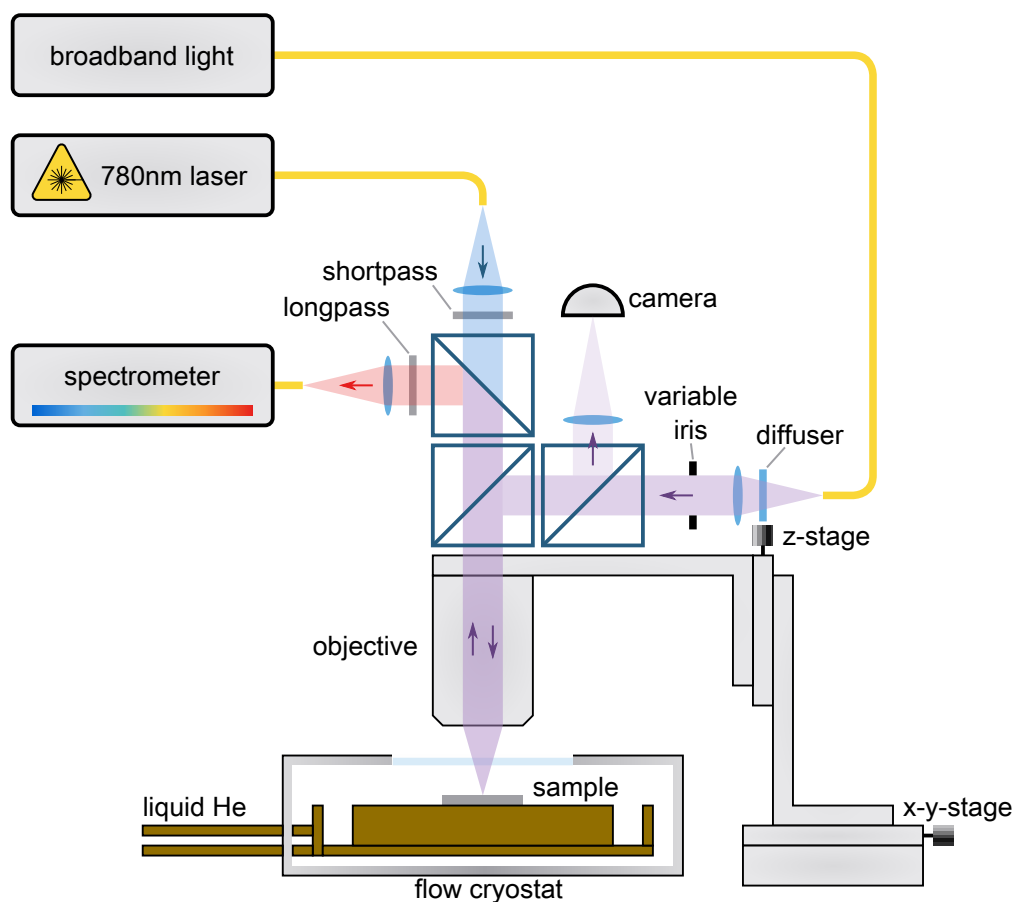


Figure 3.4: Schematic illustration of the experimental setup to optically characterise quantum dot samples. Spectrally resolved measurement of the sample reflectivity is performed via strong illumination from the broadband light source. Photoluminescence spectra are acquired by exciting the quantum emitters via a 780 nm laser diode. The confocal microscopy arrangement combined with the x-y-z-stage allows for spatial selection.

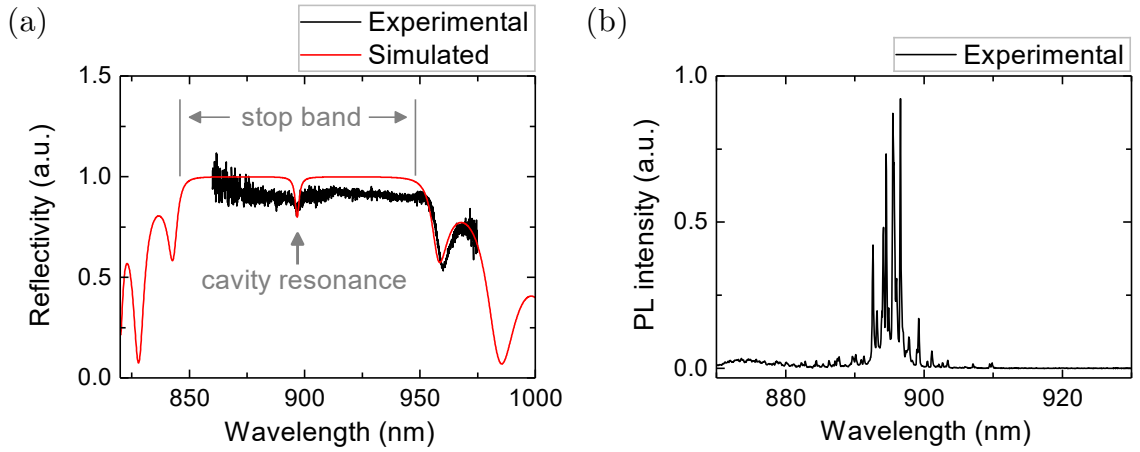


Figure 3.5: (a) Experimental and simulated reflectivity spectrum for a sample at 4 K with a  $2\lambda$  cavity resonance wavelength of 897 nm. The experimental spectrum is normalised via a reference reflectivity measurement on a gold mirror. (b) Measured photoluminescence spectrum of the same sample, revealing quantised emission. The emission intensity is strongly enhanced around the cavity resonance wavelength.

wavelength and QD spatial density will typically vary radially across the wafer. This is caused by a temperature gradient across the wafer during MBE growth, resulting in a radial variation of the layer thicknesses. Thus, pre-selecting suitable areas of the wafer in terms of cavity resonance and QD density is imperative before proceeding with further fabrication.

### 3.1.3 Electronic band structure of a quantum dot LED

In order to excite the emitters electrically, the QD layer is embedded in a p-i-n diode, as illustrated in Fig. 3.6a [Yua02, Sal10]. To create this diode, during growth the last two repeats of the bottom DBR are n-doped and the top DBR is p-doped. The resulting band structure is shown in Fig. 3.6b. The electric field  $F$  across the intrinsic region is given by

$$F = (V_{\text{built-in}} - V_{\text{bias}})/w \quad (3.3)$$

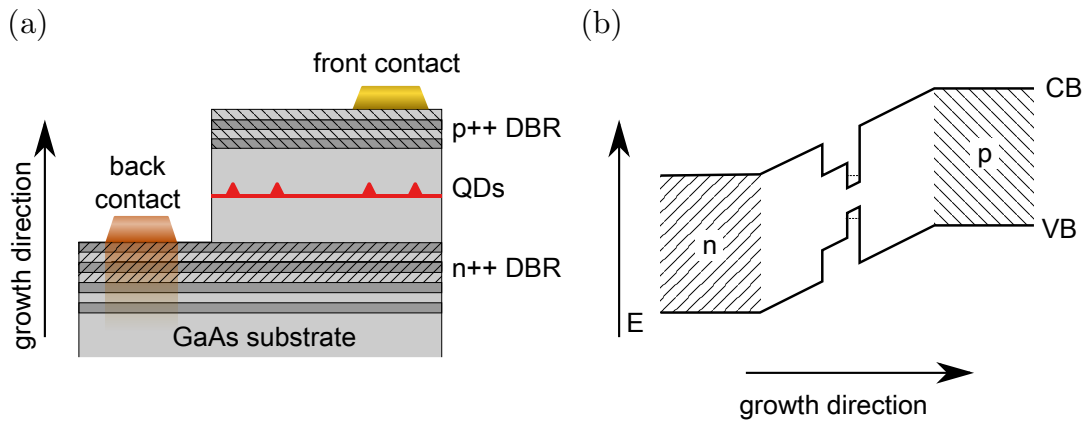


Figure 3.6: (a) Schematic of the sample design. The top and bottom DBR are p-doped and n-doped respectively to form a p-i-n diode structure. The QD layer is embedded in the intrinsic region. External access is provided by metallic front and back contacts. The doped regions are indicated by the hatched areas. (b) Simplified band diagram of the p-i-n diode. The n- and p-doped regions generate a built-in voltage across the intrinsic region. The wetting layer and QDs form a potential trap in the centre of the intrinsic region. When a forward current is injected, charge carriers relax into the QD potential.

with the applied bias voltage  $V_{\text{bias}}$ , the built-in voltage of  $V_{\text{built-in}} = 1.5 \text{ V}$  for GaAs [Var67, Sze98], and the width of the intrinsic region  $w = 2\lambda$ .

When a forward voltage beyond the turn-on voltage is applied, a current flows across the intrinsic region. Charge carriers can then relax into the QD potential, forming excitonic states as described in chapter 2.2.1. Subject to a set of selection rules, the charge carriers can then recombine radiatively, emitting a photon.

A second decay channel can be induced by quantum tunnelling. The intrinsic GaAs region around the quantum dot forms a potential barrier for the trapped charge carriers. By changing the applied voltage, the potential barrier at the position of the QD and, thus, the tunnelling rate of charge carriers out of the QD can be controlled [Hel98, Ben05]. We take advantage of this effect in Ch. 4.2.3 to generate emission pulses with ultrashort decay times.

### 3.1.4 Fabrication of quantum light emitting diodes

We use standard micofabrication techniques to fabricate the sample (see e.g. [Hel01]). Fig. 3.7 describes the steps to etch and metallise the sample via optical lithography. Before each step, the sample is cleaned from debris in acetone and isopropyl alcohol (IPA) followed by nitrogen gas. A positive photoresist is applied evenly to the surface via spin coating, and subsequently soft baked on a hotplate to harden the resist (Fig. 3.7a). The sample is then carefully brought into contact with a patterned photomask and exposed via UV light (Fig. 3.7b). The exposed areas of the resist are then removed by immersing the sample in a development solution (Fig. 3.7c), thus forming the desired pattern with micrometre feature sizes. For photolithography steps requiring micrometer-sized feature resolution, the first exposure may be preceded by an initial exposure and subsequent development of the edge beads formed by the resist during spin coating.

To etch the sample, it is then submerged in a solution of sulphuric acid, hydrogen peroxide and deionised water (Fig. 3.7d). Afterwards, the resist is removed through a lift-off procedure via acetone and IPA, leaving only the etched sample as a result (Fig. 3.7e). To evaporate metal onto the sample surface, after development the sample may be subjected to a plasma ash in order to first remove any residual resist in the developed areas. The sample is then mounted in a high-vacuum bell jar evaporator, and the metal is thermally evaporated onto the sample until the desired thickness is reached (Fig. 3.7f). Finally, the resist is again removed via a lift-off, leaving the evaporated metal only on the desired sample regions (Fig. 3.7g).

The processing sequence to fabricate a QD-LED consists of one etch step to laterally define the diode mesa and two metal evaporation steps for the back and front contact respectively, as shown in Fig. 3.8. After the back contact evaporation, the sample is annealed in a hydrogen/nitrogen gas atmosphere to aid diffusion of the metal into the n-doped DBR layer, reducing the contact resistance [Tah11]. The front contact is not annealed in order to minimise diffusion towards the QD later. After finishing the lithography steps, the semiconductor sample is attached to a chip carrier via

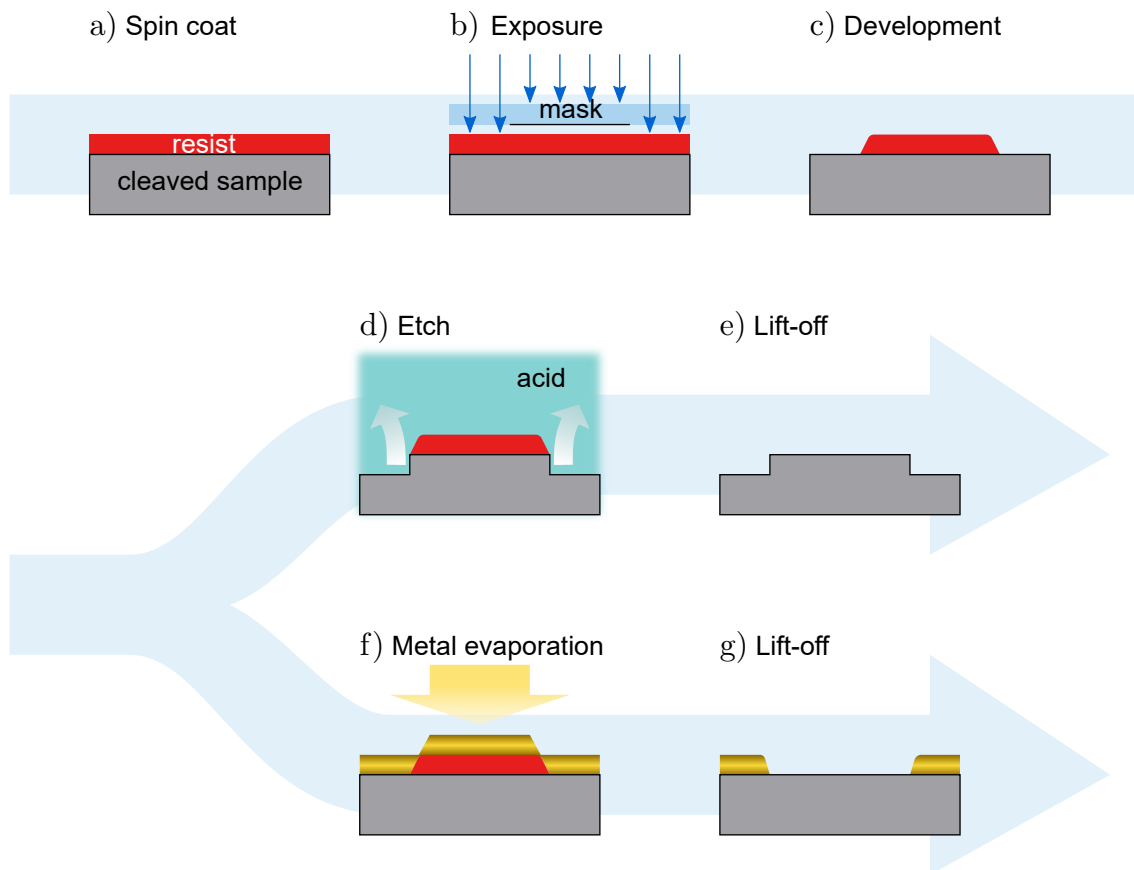


Figure 3.7: Process flow diagram for etching and metal deposition via photolithography, using a positive photoresist. (a) The resist is spin coated onto the sample forming an even layer. The sample is then baked to harden the resist. (b) A photomask is brought into contact with the sample. Subsequently, the exposed regions of the resist are exposed to UV light. (c) A chemical developer removes the exposed regions of the photoresist. (d–e) To remove parts of the sample, an appropriate acid mixture (e.g. sulphuric acid) etches the exposed areas of the sample. (f–g) To metallise the sample, the chosen metal is thermally evaporated onto the exposed surfaces.

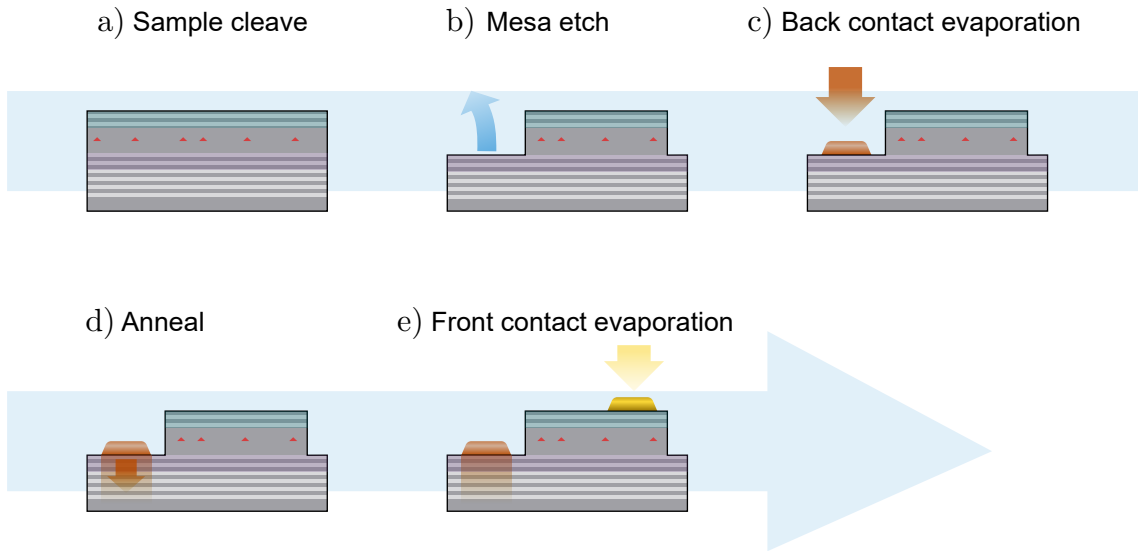


Figure 3.8: Process flow diagram for the microfabrication of a QD-LED. (a) The wafer is cleaved to a suitable lateral size. (b) The lateral diode area is defined via a mesa etch. (c) The back contact is deposited by evaporating AuGeNi. (d) Ohmic contact to the n-doped DBR layers (shaded in purple) is established via annealing of the bottom contact. (e) The top contact is metallised using CrAu or equivalent, establishing electrical access to the p-doped DBR layers (shaded in teal).

an adhesive that is subsequently cured on a hotplate. Finally, the front and back contacts of the diodes are then connected to the electrical leads of the chip carrier via gold ball bonding.

Optical micrographs of a finished device are shown in Fig. 3.9. Although the devices feature a shared back contact, each front contact operates individually, in order to preventing defective diodes from affecting neighbouring devices. A typical QD-LED measures  $100\mu\text{m} \times 200\mu\text{m}$  in lateral area. Consequently, a single chip fits tens of independent diode devices. As seen in panel 3.9b, a bond ball covers approximately half the surface area of a typical diode, leaving the other half for optical access to the QD emission.

Figs. 3.10a and 3.10b show a typical current-voltage curve of a QD-LED cooled to 17.5 K. The turn-on voltage of 1.5 V is similar to the built-in voltage of the diode,

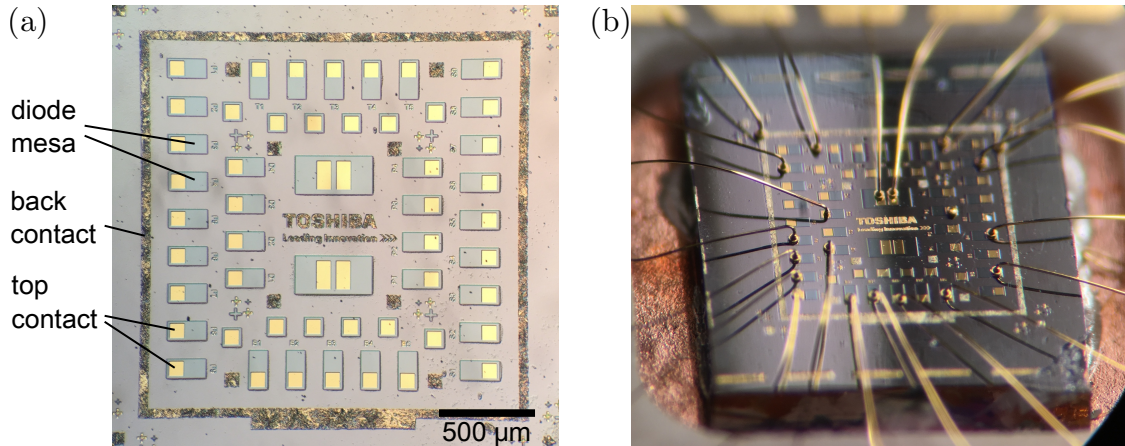


Figure 3.9: Optical micrographs of a fabricated sample. (a) Top-down view of a sample containing multiple QD-LEDs. All LEDs share a mutual back contact. (b) Oblique view of the sample, mounted on a chip carrier. Bond wires establish electrical contact to the carrier metal pads.

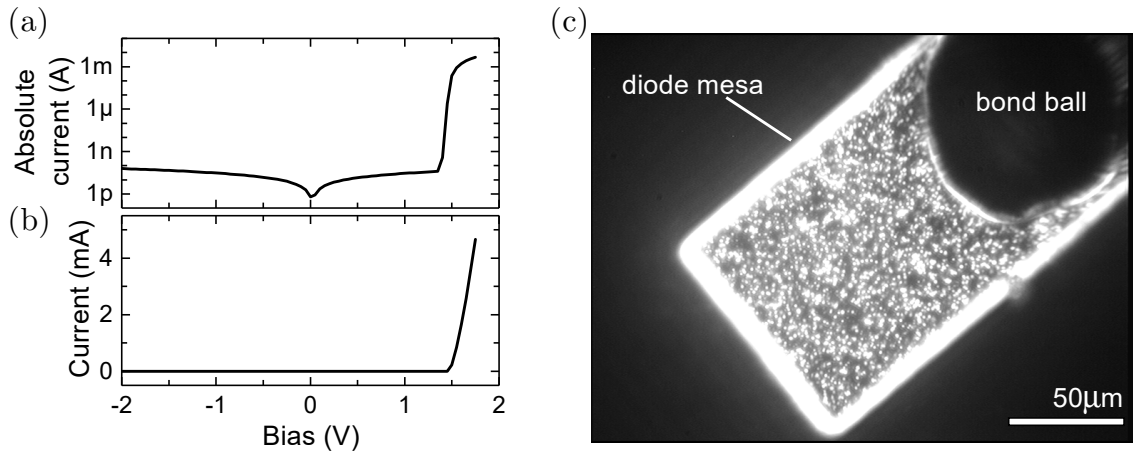


Figure 3.10: Current-voltage curve of an E-LED at  $T = 17.5$  K plotted on a (a) logarithmic and (b) linear y-scale. The turn-on voltage of  $\sim 1.5$  V approximately corresponds to the GaAs band gap at the given temperature. The (absolute) leakage current in reverse bias remains below 0.1 nA for the investigated voltage range. (c) Top-down NIR micrograph of an E-LED during operation at the same temperature. Optical emission from single QDs is spatially resolved on the diode mesa.

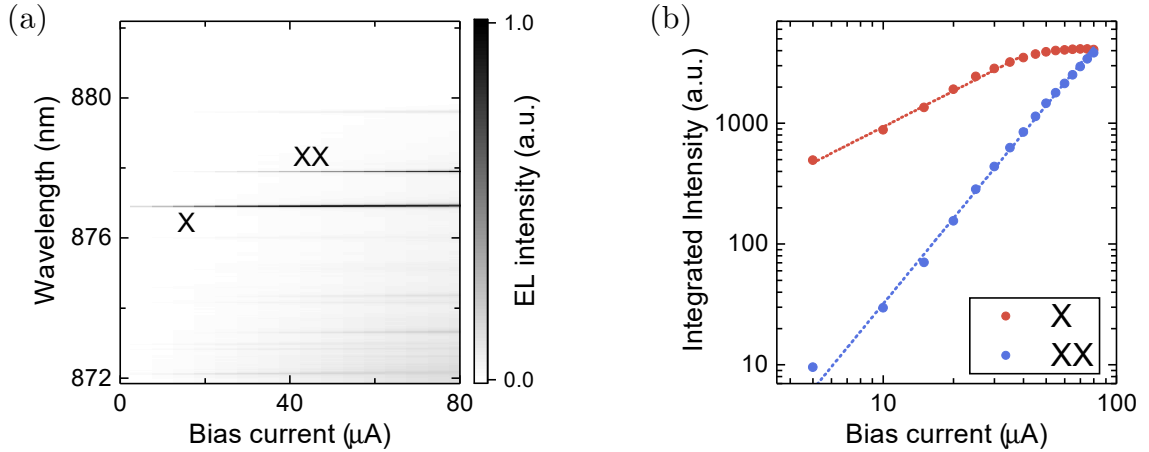


Figure 3.11: (a) Electroluminescence spectrum as a function of applied current. The neutral  $XX$  and  $X$  lines are dominant. (b) Integrated  $XX$  and  $X$  intensity as a function of current. The dotted lines indicate linear fits within the log-log graph. The fitted slopes of  $2.35 \pm 0.03$  and  $0.99 \pm 0.02$  respectively for the  $XX$  and  $X$  lines are close to the expected quadratic and linear current dependencies [Ben05, Ell06].

which in turn is governed by the 1.5 eV band gap of GaAs. The residual resistance in turn-on is typically on the order of tens of Ohms, dominated by the metal to semiconductor contact resistance of the front and back contacts. Well-functioning devices typically exhibit a sub-nanoampere leakage current at reverse biases up to 2V. Fig. 3.10c shows a top-down microscope image of the QD-LED during operation. Local emission from individual, spatially separate QDs is clearly visible. Consequently we are able to spatially filter single QD emission using a typical micro-photoluminescence experimental setup.

Fig. 3.11a shows the luminescence spectrum of an electrically driven QD-LED as a function of the applied bias current  $V_{\text{bias}}$ . The  $XX$  and  $X$  emission is identified via correlation measurements and intensity-current dependencies. Fig. 3.11b shows this current-intensity dependency, extracted from Voigt fits to the individual peaks. Here, the saturation of the  $X$  state is visible at a current of  $70 \mu\text{A}$ , while the  $XX$  only saturates at even higher currents. The spectrum is clearly dominated by these two emission lines, making these devices especially suitable for entangled photon

generation from the  $XX-X$  radiative cascade as described in Ch. 2.2.1. Additional weak emission lines stem from further QD states (see e.g. [Bay02]) or other nearby quantum emitters.

## 3.2 Cryogenic and optical measurement setup

For long-term measurements at cryogenic temperatures, the sample is mounted in a commercial Helium vapour cryostat, as illustrated in Fig. 3.12. This system allows for enhanced isolation from mechanical vibrations, in addition to high cooling power and temperature stability. The 48-inch leg of the cryostat is inserted directly into a 100 L liquid Helium dewar. A vacuum pump draws the Helium through the vaporiser into the main chamber, such that the sample is immersed in Helium vapour. The cooling power is controlled in two ways. Firstly, the Helium flow is controlled via flow valves at the bottom of the insert leg and at the Helium pump (both not shown). Long-term temperature stability is achieved via the heater at the top of the insert leg. The heater is controlled via an active feedback loop in combination with a silicon diode temperature sensor next to the heater and a second sensor underneath the sample platform, providing millikelvin stability of the sample temperature.

High-frequency compatible coaxial cables lead from the chip carrier to an external electrical pulse generator. We collect the QD electroluminescence confocally into a collection fibre. The sample and PCB are fastened to a stack of piezo nanopositioners, allowing for x-y-z control of the sample position w.r.t. the high NA objective lens. Finally, an external broadband light source and camera allow for optical imaging of the sample during operation.

### 3.2.1 Measurement of the fine-structure splitting

The FSS of the QD is measured via the optical setup illustrated in Fig. 3.13. The QD emission spectrum is measured as a function of the angle  $\chi_{\text{QWP}_2}$  of the rotating  $\text{QWP}_2$  in front of the spectrometer. Combined with the static  $\text{LP}_2$ , the rotating  $\text{QWP}_2$  projects the  $XX$  and  $X$  emission onto a continuum of measurement polarisation states.

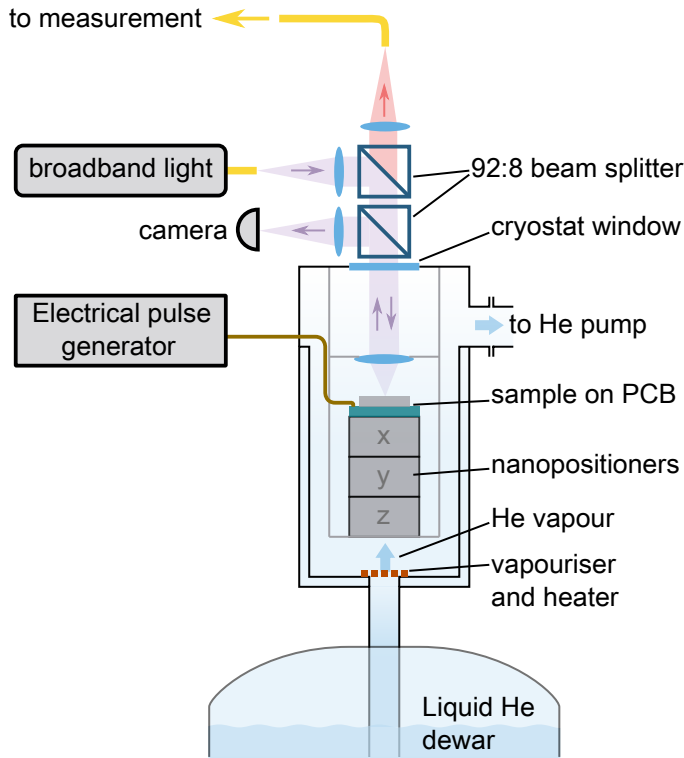


Figure 3.12: Schematic of the cryogenic setup for long-term optical measurements. The sample is mounted in a Helium vapour cryostat, inserted into a liquid He dewar. A vacuum pump draws He vapour into the cryostat chamber, directly cooling the sample. The cryostat is optimised for minimum vibration during operation.

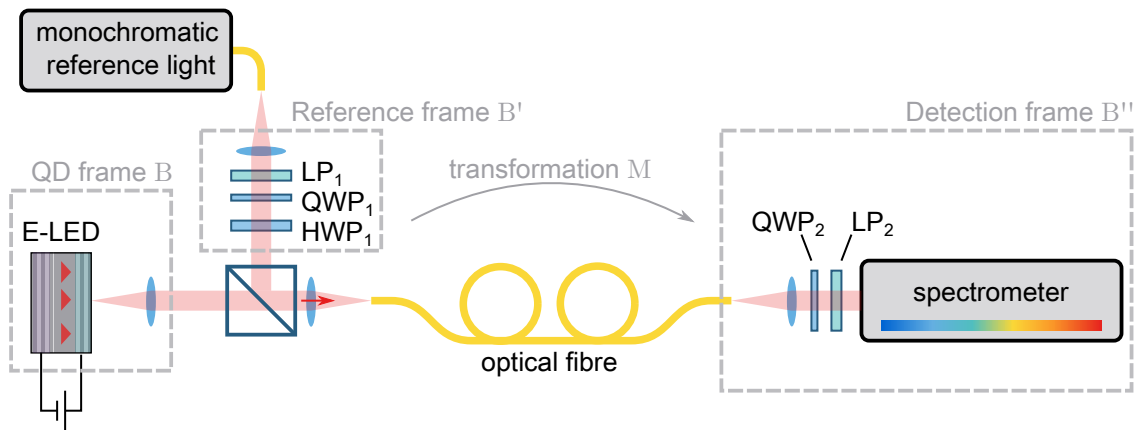


Figure 3.13: Optical setup to measure the FSS splitting and polarisation orientation of the QD emission. The rotatable quarter-wave plate (QWP<sub>2</sub>) and (fixed) linear polariser (LP<sub>2</sub>) in front of the spectrometer act as a polarimeter. A reference light source allows us to calculate the unitary transformation  $M$  on the polarisation state, dominantly caused by fibre birefringence.

Although for a non-zero FSS both,  $XX$  and  $X$  consist of two non-degenerate emission lines each, these are typically not resolved on a standard spectrometer. Nevertheless, when fitting a single Lorentzian to the two combined emission lines, the centre energy shifts as shown in Fig. 3.14a. The energy difference  $\Delta E = E_{XX} - E_X$  between the  $XX$  and  $X$  emission lines as a function of  $\chi_{\text{QWP2}}$  follows the form [SS17]

$$\Delta E(\chi_{\text{QWP2}}) = \bar{E} + S \left( \frac{\alpha}{1 + \alpha} \right) \quad (3.4)$$

where  $S$  is the fine-structure splitting and  $\alpha(\chi_{\text{QWP2}})$  is given by

$$\alpha(\chi_{\text{QWP2}}) = \frac{1}{2} \cos 2\theta (1 + \cos 4\chi_{\text{QWP2}}) + \sin 2\theta \cos \varphi \sin 4\chi_{\text{QWP2}} \quad (3.5)$$

$$- 2 \sin 2\theta \sin \varphi \sin 2\chi_{\text{QWP2}}. \quad (3.6)$$

The parameters  $\theta/2$  and  $\varphi$  are the same as defined in Ch. 2.1.1 and correspond here to the (physical) angle of rotation and phase shift applied to the emission during transmission through the optical setup. Taking the energy difference  $\Delta E$  compensates for systematic errors in measured energy, such as due to beam steering in the spectrometer caused by the rotating wave plate. A fit of this function is plotted in Fig. 3.14a as well, demonstrating the low statistical error for this method even for a  $1.8 \mu\text{eV}$  FSS, measured on a spectrometer with an optical resolution of  $40 \mu\text{eV}$ . As this method of determining the FSS demands only the measurement of a few spectra, it is typically faster than other methods relying on spectrally resolving the two individual non-degenerate  $XX$  or  $X$  emission lines, such as e.g. via a scanning Fabry-Pérot interferometer [Vog07].

### 3.2.2 Calibration of the quantum dot polarisation eigenbasis

As established in Chs. 2.2.1 and 2.3.1, entanglement is measured by correlating the photon pairs in different polarisation bases. Especially for a FSS of at least several  $\mu\text{eV}$ , it is important to accurately calibrate the required polarisation states to track the time-evolving entangled two-photon state.

Therefore, even though the combined QD emission is in general unpolarised [Ste06], it is necessary to translate the natural orientation of the QD polarisation states to

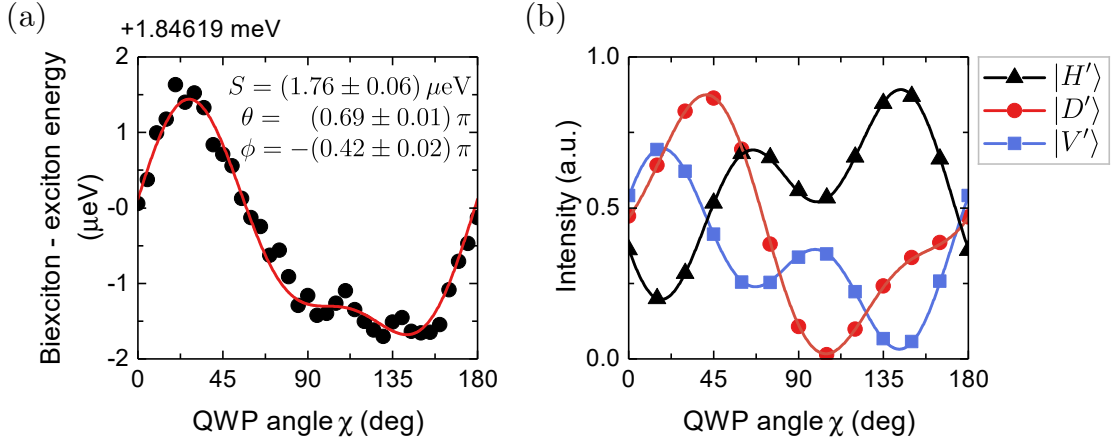


Figure 3.14: Polarimeter measurements to determine FSS and fibre birefringence.

(a) Measured energy difference  $\Delta E$  between biexciton and exciton emission as a function of QWP angle  $\chi$ . Emission energies are determined via single Lorentzian fits to the spectra. Experimental data (black spheres) and fit (red line) (b) Measured intensity of the  $|H'\rangle$ ,  $|D'\rangle$ , and  $|V'\rangle$  polarisation states as a function of QWP angle  $\chi$ . Experimental data (symbols) and fit (lines).

the laboratory reference frame. However, in particular the birefringence of an optical fibre applies an effectively random (but static) rotation to the incoming polarisation. In other words, a unitary transformation  $M$  is applied to the emitted polarisation state. (Note that polarisation-maintaining fibre only preserves the linear polarisations parallel to either the fast or slow axis of the fibre as well, while other polarisations pick up an arbitrary phase offset. Thus it is often preferential to use single-mode fibre in order to prevent the temporary wave packet from dissociating.)

To this end, we implemented a deterministic method of generating the required polarisation states, relying on the measurement of the QD emission and three calibration polarisation states. After generating the required polarisation states from a calibration source, we can then calibrate the detection bases that are used for measuring entanglement.

Firstly, we are able to extract the polarisation of the  $|X_H\rangle$  state when measured in the detection frame  $B''$  via the fit of Eq. (3.4), as shown in Fig. 3.15a. (The designation of this state as either  $|X_H\rangle$  or  $|X_V\rangle$  is effectively a matter of nomenclature.) However,

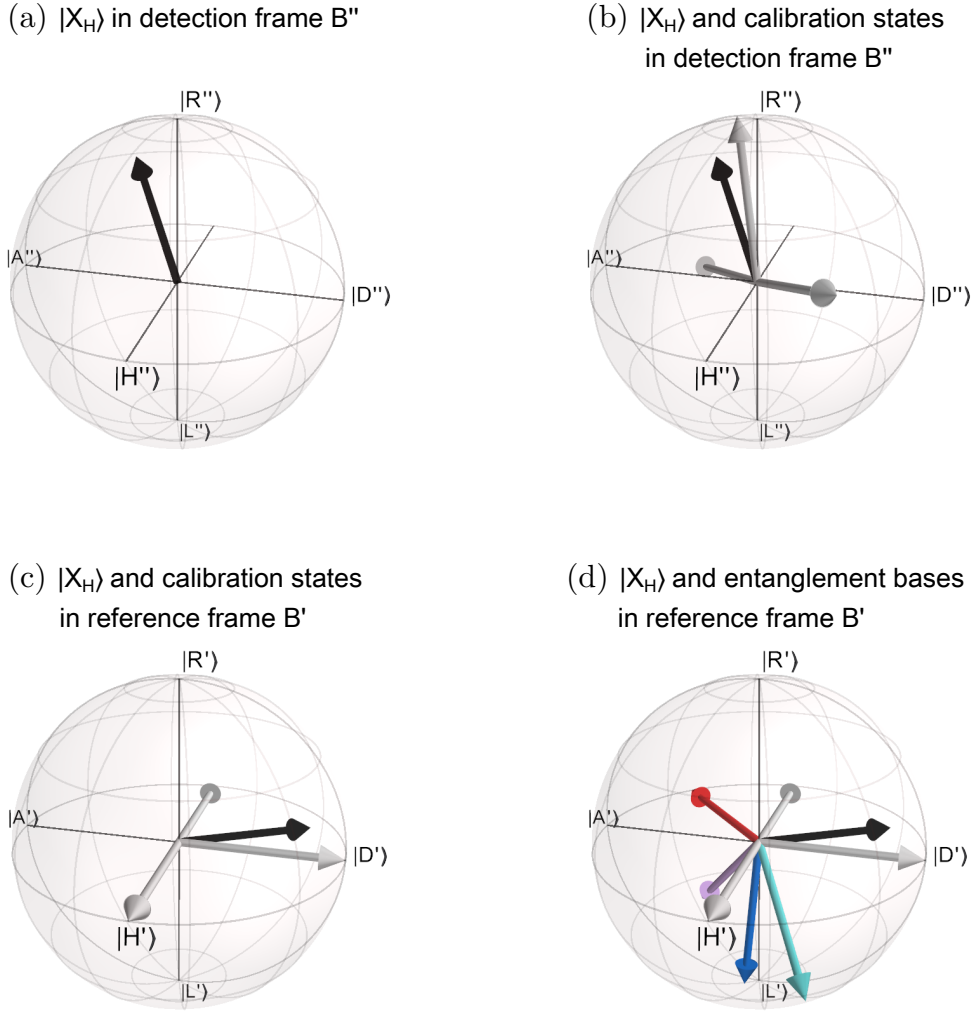


Figure 3.15: Process steps to determine the polarisation bases required to characterise entanglement, plotted on Poincaré spheres. Shown for a QD with a FSS  $10\ \mu\text{eV}$ . (a) The  $|X_H\rangle$  polarisation state emitted from the QD (black arrow) is measured in the detection frame  $B''$ . (b) The polarisations  $|H'\rangle$ ,  $|D'\rangle$ , and  $|V'\rangle$  (grey arrows) are generated in the reference frame  $B'$  and measured in the detection frame  $B''$ . (c) The unitary transformation matrix  $M$  of the optical fibre is calculated. The previously measured polarisations are then transformed from the detection frame to the reference frame via  $M^{-1}$ . (d) The required entanglement bases  $|D\rangle$ ,  $|E_{LD}\rangle$ ,  $|L\rangle$ , and  $|E_{LA}\rangle$  (red, purple, blue, and teal respectively) are calculated in the reference frame.

from this single point of reference it is not possible to determine the rotation for an arbitrary input state.

Thus, for the second step, we generate additional calibration polarisation states in what we label as the reference frame  $B'$  (see Fig. 3.13). To do so, we use the linear polariser  $LP_1$  and rotatable half-wave plate  $HWP_1$  mounted to the top of the cryostat to sequentially generate the polarisation states  $|H'\rangle$ ,  $|D'\rangle$ , and  $|V'\rangle$ . These calibration inputs are sent through the same optical fibre, applying the rotation  $M$ , and measured again via the polarimeter detection setup. As the calibration states consist of only a single polarisation state at a time, in this case the total intensity instead of the centre wavelength follows Eq. (3.4)f (cf. [SS17]). A typical measurement including fit is shown in Fig. 3.14b, again allowing us to extract the rotation  $\theta/2$  and phase shift  $\varphi$  from reference frame  $B'$  to detection frame  $B''$  (Fig. 3.15b).

For the third step we then calculate the transformation matrix  $M$  of the optical fibre such that  $M B' = B''$  for an arbitrary polarisation state. We first determine the parameters

$$\begin{aligned} k_1 &= \frac{h'_{1,B''}}{h'_{2,B''}}, & k_2 &= \frac{v'_{1,B''}}{v'_{2,B''}}, \\ k_3 &= \frac{d'_{1,B''}}{d'_{2,B''}}, & k_4 &= \frac{k_3 - k_2}{k_1 - k_3}, \end{aligned} \quad (3.7)$$

where  $h'_1$  and  $h'_2$  are the two components of the Jones vector  $|H'\rangle$  as measured in the detection frame  $B''$ , and likewise for  $d'_{1,B''}$ ,  $d'_{2,B''}$ ,  $v'_{1,B''}$ , and  $v'_{2,B''}$ . The unitary transform matrix  $M$  then comes to [Jon47, Hef92]

$$M = \eta \begin{pmatrix} k_1 k_4 & k_2 \\ k_4 & 1 \end{pmatrix}, \quad (3.8)$$

where the scaling factor  $\eta$  is given by [Jon47]

$$|\eta|^2 = \frac{2}{1 + |k_2|^2 + |k_4|^2 + |k_1|^2 |k_4|^2}. \quad (3.9)$$

We can then apply the inverse  $M^{-1}$  of this transformation matrix to evaluate the measured polarisation in the reference frame instead of the detection frame, as shown in Fig. 3.15c. As we can see in the figure, the  $|H'\rangle$ ,  $|D'\rangle$ , and  $|V'\rangle$  calibration

states are rotated back to their initial polarisations. Furthermore, we now know the orientation of the  $|X_H\rangle$  state generated from the QD in the reference frame  $B'$ . Thus we can easily compute the required rotation angles of QWP<sub>1</sub> and HWP<sub>1</sub> to reconstruct polarisation states originally defined in the QD eigenbasis.

Finally, we compute the QWP<sub>1</sub> and HWP<sub>1</sub> angles to generate the  $|D\rangle$ ,  $|E_{LD}\rangle$ ,  $|L\rangle$ , and  $|E_{LA}\rangle$  states in the frame of the QD. In the presented setup, the sample and the reference frame are connected via free-space, low-birefringence optics only. As a consequence, a linear QD  $|X_H\rangle$  state remains approximately linearly polarised in the reference frame as well, as it does not pick up any circular components from potential phase delays. As a result, we can now calculate  $|D\rangle$  in the reference frame as the orthogonal of the  $|X_H\rangle$  state and the  $|L'\rangle$ -axis. From  $|H\rangle$  and  $|D\rangle$ , the remaining required polarisation states  $|E_{LD}\rangle$ ,  $|L\rangle$ , and  $|E_{LA}\rangle$  are then straightforwardly computed in similar fashion.

After numerically calculating the entanglement polarisation states, we can determine the required wave plate rotation angles  $\chi_{\text{QWP1}}$  and  $\chi_{\text{HWP1}}$  to physically generate these polarisation states from the reference light. This is most easily expressed via spherical coordinates of the polarisation state on the Poincaré sphere:

$$\chi_{\text{QWP1}} = -\frac{\beta'}{2} \quad (3.10)$$

$$\chi_{\text{HWP1}} = -\frac{\alpha'}{4} - \frac{\beta'}{4}, \quad (3.11)$$

with the azimuth angle  $\alpha'$  and elevation angle  $\beta'$  of the respective polarisation state in the reference frame. A wave plate angle of 0 corresponds to alignment of the respective wave plate fast axis with the linear polariser LP<sub>1</sub>. Alternatively, in terms of physical rotation angle  $\theta/2$  and phase delay  $\varphi$  (also in the reference frame) this can be expressed as

$$\chi_{\text{QWP1}} = \frac{1}{2} \arctan \frac{\sin \theta \sin \varphi}{\sqrt{\cos^2 \theta + \sin^2 \theta \cos^2 \varphi}} \quad (3.12)$$

$$\chi_{\text{HWP1}} = -\frac{1}{4} \arctan (\tan \theta \cos \varphi) + \frac{1}{2} \chi_{\text{QWP1}}. \quad (3.13)$$

This method has been employed over multiple measurement runs, demonstrating high reproducibility. For a given sample, the calculated wave plate angles  $\chi_{\text{QWP1}}$  and

$\chi_{\text{QWP1}}$  varied by less than  $0.3^\circ$  across measurements repeated over several months, even when the transformation matrix  $M$  of the optical fibre varied as the fibre was repeatedly adjusted.

Potential systematic errors affecting this method are dominated by the following: Firstly, the method relies on accurate optical retardance of the involved wave plates at the given wavelength. This is easily ensured by using commercially available precision optics. Secondly, for QDs with a near-zero FSS, the emitted  $XX$  and  $X$  eigenstates may have a circular component [Ste12a], such that the measured QD eigenstate is no longer in the HV basis. However, this could be counteracted by reconstructing the  $|H\rangle$  state of the QD by projecting the measured elliptic  $|X\rangle$  eigenstate onto the linear plane, and thus removing the circular component. Overall, as these errors are straightforward to detect and counteract, this method has shown to be a reliable and deterministic approach to accurately selecting the polarisation bases to measure entanglement from QDs.



# 4 | High-bandwidth pulsed single-photon sources

This section describes the design, fabrication, and operation of an ultrafast single-photon LED. Selected results of this section have been published in Ref. [Mül20]. The sample was grown by Ian Farrer and David A. Ritchie; and processed by Joanna Skiba-Szymanska, Jonathan R. A. Müller, and Ginny Shooter. Optical experiments and data analysis were realised by Jonathan R. A. Müller with valuable contributions from R. Mark Stevenson and Ginny Shooter with guidance from Andrew J. Shields.

In order to employ single photon LEDs in applications such as quantum key distribution, it is desirable to achieve pulsed operation with high repetition rates. Contemporary QKD systems based on weak coherent laser pulses employ clock rates in the GHz range [Yua18, Boa18, Min19]. Consequently, this chapter focuses on the high-bandwidth electrical generation of single photons. We begin by introducing the requirements for a high-bandwidth QD LED from an electrical standpoint, starting from a simple circuit model. This is then followed by the introduction of a low-capacitance, high-bandwidth QD LED design, together with the associated fabrication process. Subsequently, we focus on the resulting temporal control of the optical emission, via fast initialisation pulses and rapid tunnelling of charge carriers. Finally, we demonstrate the generation of single photon emission with ultra low time jitter at a record 3.05 GHz clock rate.

## 4.1 Low-capacitance diode design

The temporal shape of the optical emission from a QD LED is directly controlled via the voltage applied to the diode. Naturally, for voltages above turn-on, a current

flows and the QDs emit light. As demonstrated in Refs. [Ben05] and [Har13], the optical emission can be quenched by reducing the voltage significantly below turn-on. By doing so, the width of the potential barrier trapping the carriers is reduced, thus inducing quantum tunnelling of the charge carriers out of the QD [Fry00a].

Consequently, in order to operate the QD LED at ultrafast clock frequencies, a first requirement is an LED design that is capable of sufficiently fast electrical switching times. An equivalent circuit diagram for a p-i-n diode is shown in Fig. 4.1. For a depleted diode, the shunt resistance  $R_S$  typically reaches a resistance of  $\gg 1 \text{ M}\Omega$  (cf. I-V curve of Fig. 3.10a), such the remaining circuit effectively turns into a simple RC circuit. We can then estimate the cutoff frequency  $f_{\text{cutoff}}$  via

$$f_{\text{cutoff}} = \frac{1}{2\pi R_P C}. \quad (4.1)$$

Here  $R_P$  is the parasitic resistance, dominated by the front and back contact resistance.  $C$  is the capacitance of the depleted diode, given by [Sze98]

$$C = \varepsilon_0 \varepsilon_{\text{GaAs}} \frac{A}{w} \quad (4.2)$$

with the vacuum permittivity  $\varepsilon_0$ , the relative GaAs permittivity  $\varepsilon_{\text{GaAs}} = 12.36$  (at liquid Helium temperature [Str76]), and intrinsic region thickness  $w$ . The parameter  $A$  is the lateral active area of the diode, corresponding to the lateral geometric area where n-doped and p-doped layer overlap vertically. For a standard QD LED as described in Ch. 3.1.4, with  $A = 100 \mu\text{m} \times 200 \mu\text{m}$  and an intrinsic region thickness equal to the  $2\lambda$  cavity (disregarding diffusion of dopants), we calculate  $C = 4 \text{ pF}$ . For a typical contact resistance on the order of  $100 \Omega$ , Eq. (4.1) yields a cutoff frequency

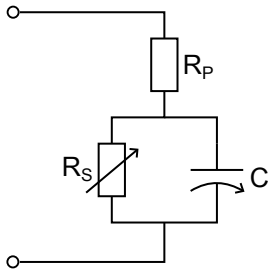


Figure 4.1: Equivalent circuit diagram of a p-i-n diode [Gop88]. The capacitance  $C$  and shunt resistance  $R_S$  vary with the applied voltage. For a depleted diode, the shunt resistance is typically  $\gg 1 \text{ M}\Omega$ . The parasitic resistance  $R_P$  is static, dominated by contact resistance.

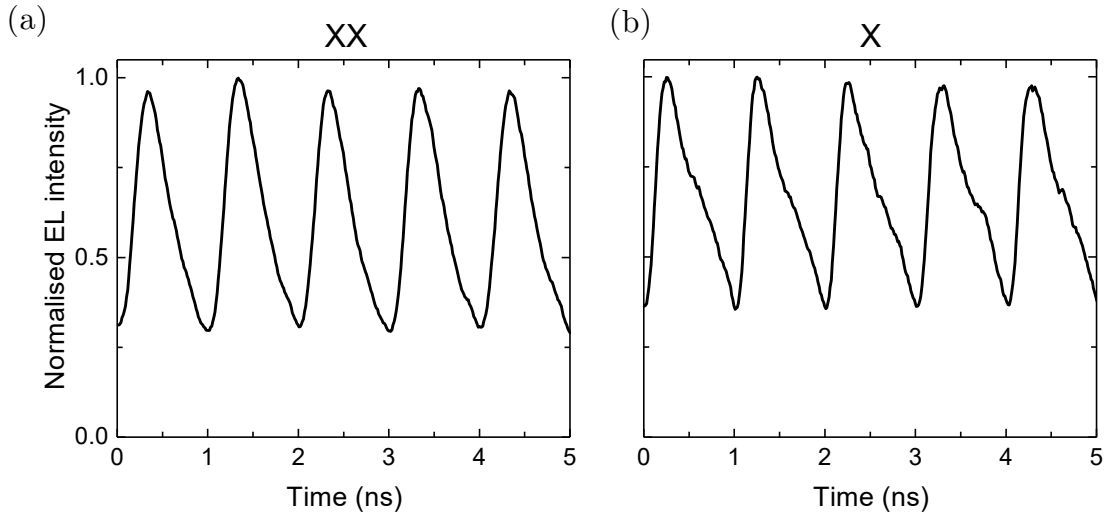


Figure 4.2: Normalised EL emission of the (a) biexciton and (b) exciton on a standard  $100\ \mu\text{m} \times 200\ \mu\text{m}$  QD LED, electrically driven via a 1 GHz square wave (50% duty cycle) with a 2.0 V amplitude and a  $-0.2\ \text{V}$  DC bias. Despite the large electrical pulse amplitude, the emission is not fully quenched between clock cycles.

of only 0.4 GHz. Note that the diode capacitance changes with the applied voltage, as charge carriers populate the intrinsic region [Sze98]—here we calculate this limit only for the case of a depleted diode. Nevertheless, at low-temperature clocked operation a significant part of the clock cycle would be spent with the diode below turn-on voltage with an effectively depleted intrinsic region, making the cutoff frequency for a depleted diode a valuable parameter for practical applications.

Thus, it becomes clear that the slow cutoff frequency of this conventional LED design makes it unsuitable for applications with gigahertz clock rates. This is highlighted in Fig. 4.2, showing such a standard QD LED driven by an electrical 1 GHz square wave with a 2 V amplitude and a  $-0.2\ \text{V}$  DC bias. Although the gigahertz-clocked character of the emission is already visible, we are unable to induce sufficient tunnelling of the charge carriers out of the QD—despite the large voltage modulation. Fitting exponential decays to the data yields decay times of  $\tau_{XX} = 434\ \text{ps}$  and  $\tau_X = 380\ \text{ps}$ , not substantially reduced from typical radiative lifetimes. This indicates the voltage

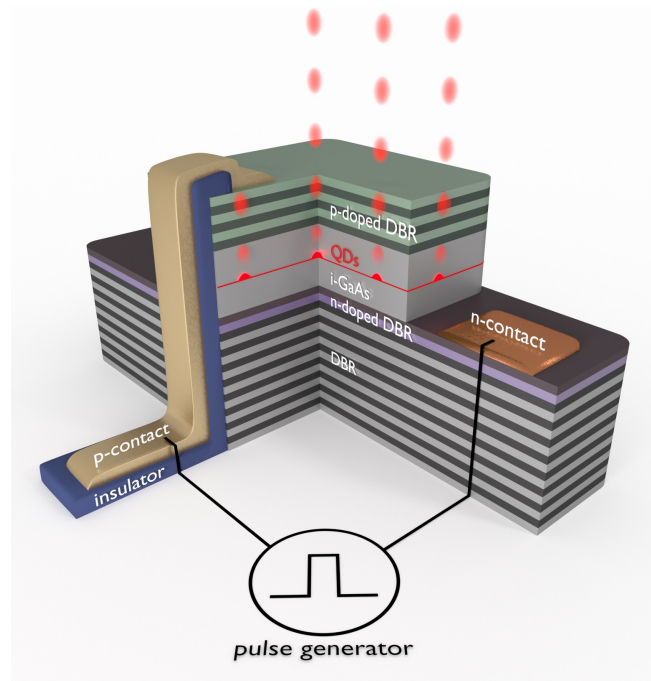


Figure 4.3: Schematic illustration of the device cross section (not to scale). Charge carriers are supplied to the QD by inducing an electrical current across the intrinsic region (i-GaAs). A lateral size of the diode mesa as small as  $10\ \mu\text{m} \times 10\ \mu\text{m}$  and high-bandwidth optimized packaging (not shown) allow for GHz-clocked operation.

across the diode does not substantially reduce below the turn-on voltage between driving pulses. Consequently, without strong tunnelling the emission is not quenched fully in between subsequent driving pulses.

#### 4.1.1 Design and fabrication of a high-bandwidth QD LED

To enable GHz repetition rates on QD LEDs, it is imperative to optimize the device for a fast electrical response to the input pulses. In particular, to achieve a suitable optical response from the sample, it is desirable to not only deliver a sinusoidal electrical signal to the position of the QDs, but to have control over the pulse shape and width. Thus, the electrical bandwidth needs to include not just the base repetition frequency, but higher order harmonic frequencies as well.

As Eqs. (4.1) and (4.2) show, the cutoff frequency is governed by the parasitic resistance  $R_P$ , thickness  $w$ , and the lateral diode area  $A$ . For an improved diode design, we first focus on the lateral diode area. In the current design, the diode requires a minimum lateral area of approximately  $100\ \mu\text{m} \times 100\ \mu\text{m}$  to provide sufficient area for a top contact pad that is large enough to enable bonding (see Fig. 3.9b). To remove this limitation, we employ the design illustrated in Fig. 4.3. Prominently, the p-contact bond pad is moved from the top of the diode to the side. As the p-contact is no longer above the n-type layer (as opposed to e.g. in Refs. [Yua02] and [Böc08]), it no longer contributes to diode capacitance. Instead, only a thin track leads from the contact to the p-doped region of the semiconductor at the top of the diode structure. A similar approach has been taken in Ref. [Ben05], although we explore diode areas with substantially smaller footprints down to  $10\ \mu\text{m} \times 10\ \mu\text{m}$ .

As the parasitic resistance  $R_P$  is dominated by the contact resistance of the metal contact, this parameter offers little room for improvement. Nevertheless, we introduce PdGeTiPt p-contacts to the design, to potentially improve the resulting contact resistance [Jon97]. Notably, the reduced diode mesa area and resulting smaller p-contact area leads to an increased contact resistance. The contact resistance resulting from the n-contact, on the other hand, remains unaffected by the reduce mesa area. Thus, since the total parasitic resistance scales less than directly proportionally with the p-contact resistance, overall a reduced diode mesa area still implies a faster cut-off frequency. Finally, an increased cavity thickness  $w$  would inversely reduce the diode capacitance. However, an increased cavity thickness reduces the optical extraction efficiency of the cavity design [Bar02]. In addition, as highlighted e.g. by Kantner et al. [Kan17], charge carriers (especially holes) require a not insignificant amount of time to populate the QD layer after diode turn-on, limited by the respective mobility. For the given  $2\lambda$  cavity this is already on the order of several picoseconds [Kan17], such that an increased cavity thickness (by multiples of  $\lambda/2$ ) could be detrimental. Thus, we keep the cavity thickness at  $2\lambda$ .

The fabrication process is illustrated in Fig. 4.4. The sample heterostructure is grown via MBE, using the same layer structure as described in Ch. 3.1, and subsequently

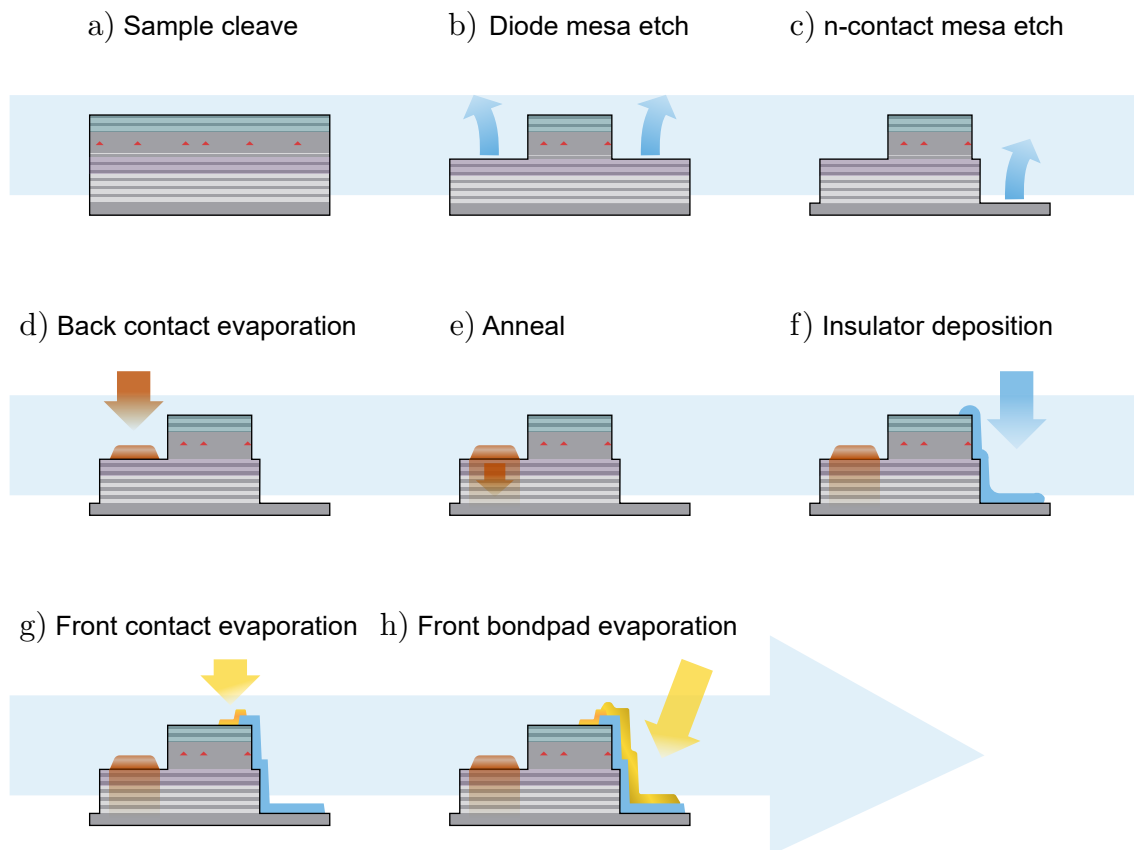


Figure 4.4: Process flow diagram for the fabrication of a low capacitance QD-LED.

(a) The wafer is cleaved to a suitable lateral size. (b) The lateral diode area is defined via a pillar etch. (c) A further mesa consisting of the pillar plus the bottom contact pad is etched. (c) The back contact is deposited by evaporating AuGeNi. (d) Ohmic contact to the n-doped DBR layers (shaded in purple) is established via annealing of the bottom contact. (f) The side wall of the pillar is insulated via SiN deposition. (e) A small top contact using PdGeTiPt is evaporated onto the pillar. (f) A larger CrAu bondpad is evaporated, leading up to the top contact.

cleaved to a suitable size for further processing (Fig. 4.4a). Then the lateral area of the diode (e.g.  $10\ \mu\text{m} \times 10\ \mu\text{m}$ ) is defined in a first etch (Fig. 4.4b). Subsequently the sample, excluding the diode mesa and a mesa for the n-contact, is etched again (Fig. 4.4c). In a first evaporation step, AuGeNi is deposited as n-contact (Fig. 4.4d) and subsequently annealed for Ohmic access to the n-doped layer (Fig. 4.4e). In order to prevent a short between n-doped layer and a subsequent p-contact, an insulating layer is required on the side wall of the diode. This is achieved via a layer of silicon nitride on the side walls, formed by chemical vapour deposition followed by inductively coupled plasma etching (Fig. 4.4f). Finally, the p-contact is evaporated onto the structure. This is done in two steps: First, a layer of PdGeTiPt on top of the diode mesa establishes low-resistance Ohmic contact to the p-type layer [Jon97] (Fig. 4.4g). To evaporate a continuous metal track leading down the side wall of the diode, the sample is attached to a tilted, continuously rotating sample holder during evaporation. In a second step, the CrAu bond pad is evaporated next to the diode mesa, including a thin connection to the p-contact (Fig. 4.4h). These two separate evaporation steps combine the superior Ohmic contact of PdGeTiPt with the empirically superior bonding compatibility of CrAu.

Fig. 4.5a shows an SEM image of a fabricated device with a schematic illustration shown in Fig. 4.5b. These images highlight the possible reduction in lateral diode active area enable by moving both bond pads to the side of the diode. Thus we can combine sizeable bond pads with a small diode area. At the same time, the electronic band structure of the diode remains effectively unchanged from that described in Ch. 3.1.3. Notably, the smaller area of the scaled down device design reduces the fabrication yield of new devices. On the one hand, the smaller feature size requires tighter tolerances during fabrication. On the other hand, the number of available QDs reduces with the diode area, requiring high yield wafers. However, this was counteracted by careful fine tuning of the diode design and fabrication protocol.

A series of device designs with different diode areas were tested. The smallest diode has an active area of only  $10\ \mu\text{m} \times 10\ \mu\text{m}$ . For an intrinsic region thickness of 480 nm, this would yield an estimated junction capacitance of 20 fF in depletion

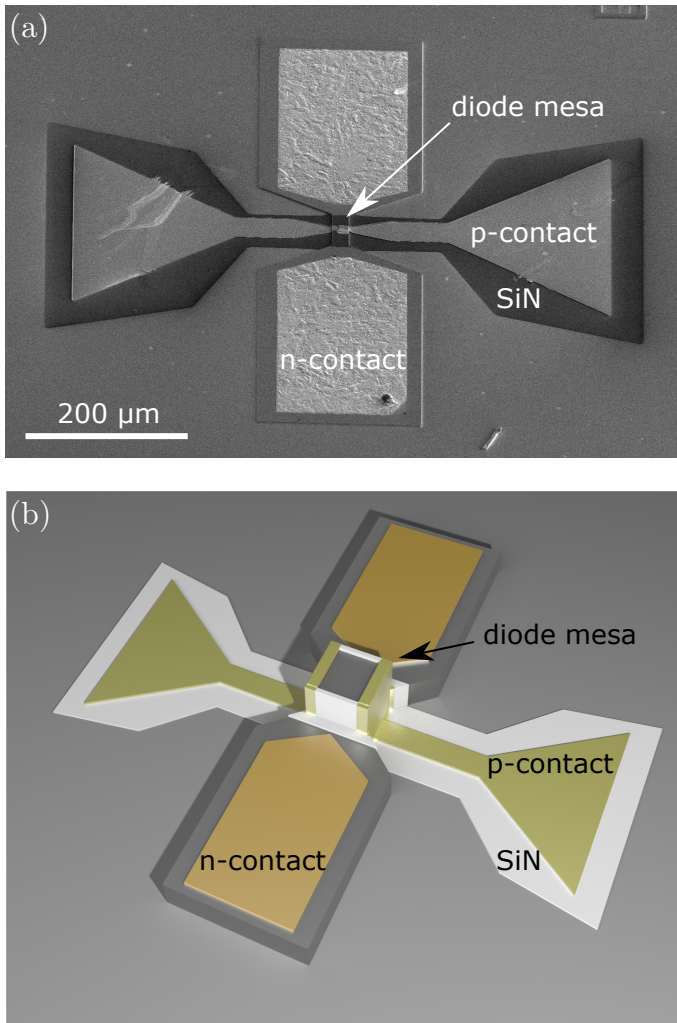


Figure 4.5: (a) SEM micrograph of fabricated device. (b) Illustration of the device design with exaggerated vertical scale.

via Eq. 4.2, reduced by an estimated order of magnitude from preceding designs [Ben05, War07, Lin19]. Due to the finer feature size of this diode, the measured contact resistance varied more strongly between different fabrication runs. With a typical contact resistance of  $R = 500 \Omega$  for such a diode, via Eq. 4.1 we estimate a cutoff frequency on the order of  $f_{\text{cutoff}} = 15 \text{ GHz}$ , sufficient for fine control of driving signals at base frequencies significantly above 1 GHz.

After microfabrication, the n- and p-type contacts are bonded to a custom designed printed circuit board (PCB) for electrical access. The PCB is single-sided and interfaces an array of micro-coaxial connectors with impedance-matched signal and ground transmission line pairs on FR4 glass epoxy for high frequency operation.

## 4.2 Experimental operation of gigahertz-clocked quantum light sources

After describing the design and fabrication of a high-bandwidth QD LED, we now focus on the experimental operation and characterisation of such a device. In particular, we explore the close electrical control on the optical emission via fast current injection and non-radiative recombination.

### 4.2.1 Experimental setup

The diode was mounted in a Helium vapour cryostat as described in Ch. 3.2. A major restraint to the cryostat setup is the electrical connection to the QD sample. Typically, the wiring cross-section to the sample device is kept as small as possible, in order to decouple the sample from outside vibrations and reduce heat transfer. However, this wiring was found to be incompatible with gigahertz-clocked driving frequencies. Fig. 4.6 shows oscillograms of the pulse generator output, recorded with a 16 GHz oscilloscope after attenuation through different cable configurations. Typically the electrical connection to the sample chip carrier was made using enamelled copper wire, allowing fast and flexible reconfiguration when needed. However, the electrical signal is heavily attenuated from the original output (panel a) after passing through the cryostat configuration including the copper wire (panel b). Driving pulses with a low duty cycle are particularly challenging as this requires the transmission of higher order harmonic frequencies as well, compared to pure sine waveforms.

The custom-designed PCB includes ultraminiature coaxial connectors, allowing for impedance matched delivery of the pulse generator signal all the way to the interface with the bond wires. The bond wires then carry the signal over the last few millimetres to the QD-LED top and bottom contacts. This enabled the final cryostat setup to closely resemble the situation in panel (c). Approximating the driving pulse with a Gaussian fit function, the temporal FWHM remains effectively unchanged at 100 ps between panels (a) and (c)—in reasonable agreement with the 50 ps nominal

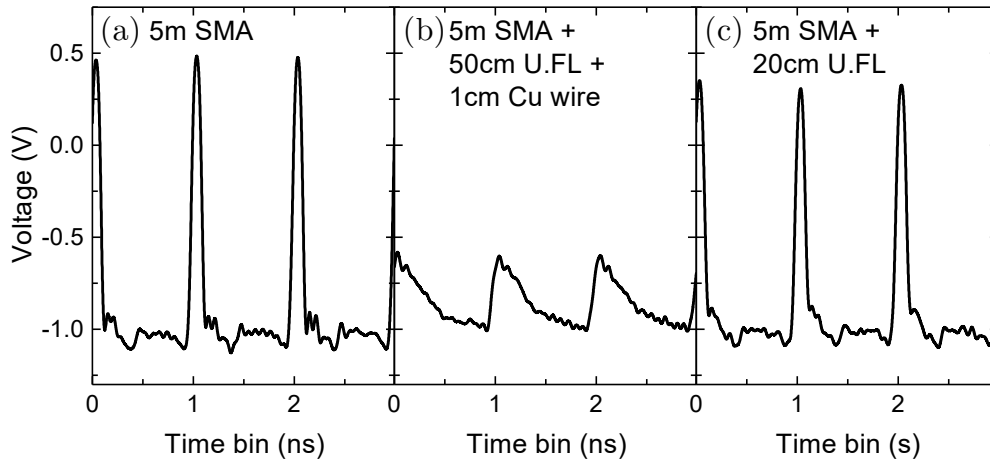


Figure 4.6: Oscilloscope of the electrical pulse generator output after attenuation through different system setups. The pulse generator was set to nominally emit 2 V, 1 GHz pulses at a 5% ( $\cong 50$  ps) duty cycle and a  $-1$  V DC bias. (a) After passing through 5m of standard coaxial SMA cable rated for frequencies up to 18 GHz. (b) After passing through typical cryostat wiring. (c) After standard miniature coaxial cable with U.F.L-type RF connectors, approximating the final cryostat setup.

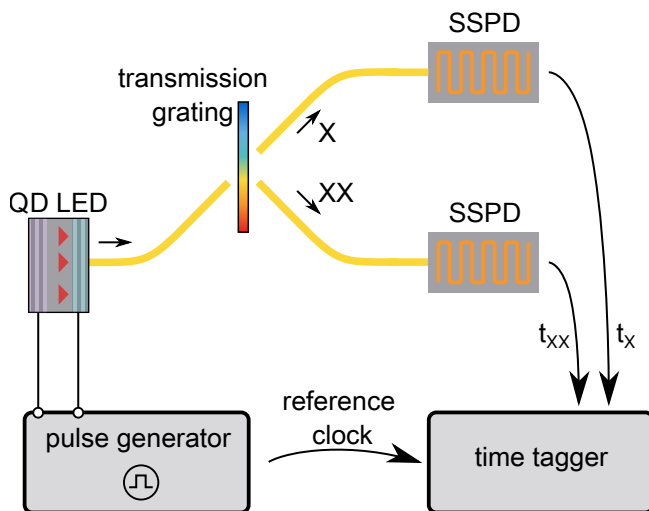


Figure 4.7: Optical setup for time-correlated single photon counting. The QD LED was electrically driven via a pulse generator. The XX and X emission was spatially separated via a transmission grating before detection via SSPDs. The detection time w.r.t. the clock of the electrical pulse generator was recorded via a time tagger.

duty cycle after taking into account the  $16 \text{ GHz} = 62.5 \text{ ps}$  analogue bandwidth of the oscilloscope. Careful optimisation of the sample stage assembly subsequently allowed us to maintain the mechanical and temperature stability of the setup despite the increased electrical wiring cross-section. The GHz-clocked electrical driving voltage pulses were supplied via a 3.35 GHz pulse generator.

Note that, as the resistance of the QD LED varies with the applied voltage, the sample itself is not impedance matched to the pulse generator source. Instead, below turn-on the megaohm shunt resistance leads to a high impedance bridging of the sample, resulting in an effective voltage across the depleted diode approximately double that of the nominal setting (as the pulse generator is calibrated only for a  $50 \Omega$  load impedance). Thus, e.g. the turn-on voltage of approximately  $1.4 \text{ V}$  is reached at a nominal pulse generator setting of  $0.70 \text{ V}$ . In this chapter all quoted voltages refer to the nominal voltage setting on the pulse generator.

The optical setup to characterise the temporal evolution of the QD is shown in Fig. 4.7. We used superconducting single-photon detectors (SSPDs) combined with a multi-channel, time-correlated single-photon-counting module (time tagger) to detect the emitted photons with an overall timing resolution of  $50 \text{ ps}$  full width at half maximum (FWHM) (Fig. 4.8). The photon detection times were then recorded in  $4 \text{ ps}$  bins and w.r.t. the clock of the electrical pulse generator.

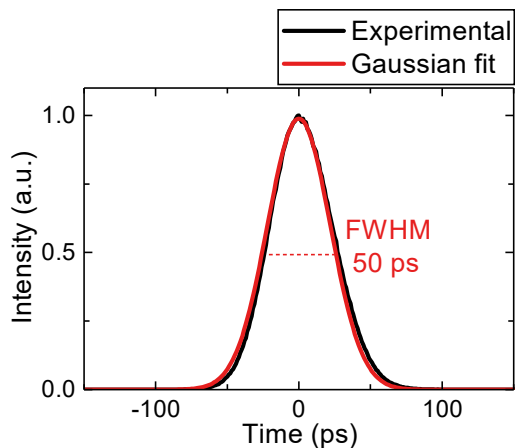


Figure 4.8: Typical instrument response of the SSPD and time-correlated single-photon-counting module to a femtosecond reference laser pulse. A Gaussian fit reveals a timing jitter of approximately  $50 \text{ ps}$  FWHM.

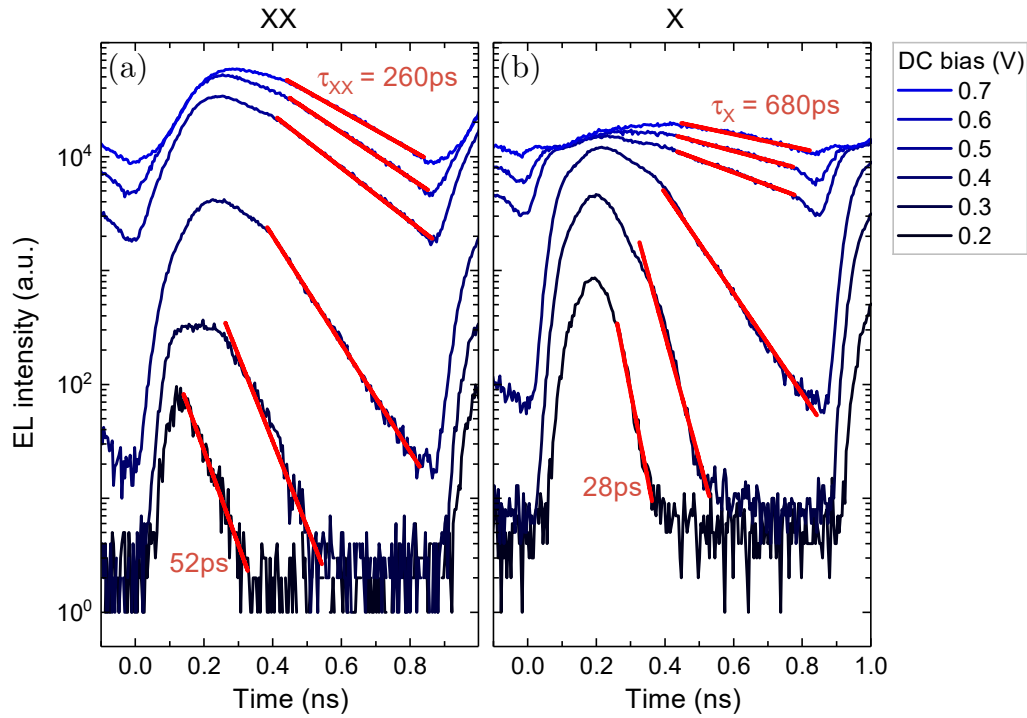


Figure 4.9: Time-resolved pulsed (a) biexciton and (b) exciton EL emission for different DC biases and fixed peak voltage. Mono-exponential fits (red lines) are used to extract the associated decay times.

## 4.2.2 Ultrafast control of the tunnelling rate

To characterise the capability of the fabricated diode, we record the emission EL of the device electrically driven at a 1.15 GHz clock rate (870 ps clock period) via rectangular pulses with a 10% = 87 ps duty cycle. We fix the peak voltage during the pulse to 1.5 V and repeat the measurement while varying the DC bias from the turn-on voltage of 0.70 V down to 0.20 V.

The resulting time-resolved emission intensity is shown in Fig. 4.9. The data highlights the strongly improved reactance of the low-capacitance diode design and the electrical setup. This becomes especially visible when compared to the data of the standard design, driven over a much larger voltage range (as shown in Fig 4.2).

When varying the DC bias from 0.70 V to 0.20 V, the measured decay time of the biexciton shortens from 260 ps by a factor of 4 down to 68 ps. The exciton decay time shortens from 680 ps down to 28 ps, a reduction by a factor of 30. Evidently, this

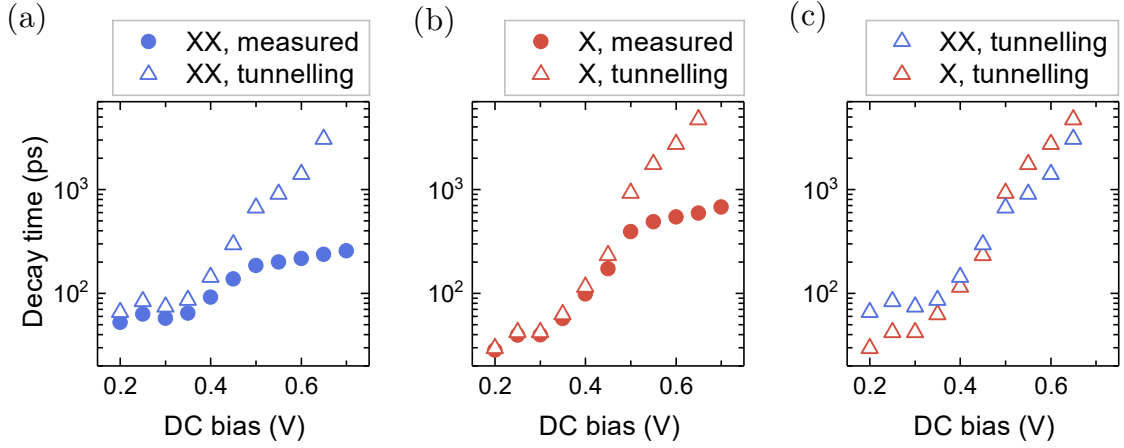


Figure 4.10: Measured decay times and estimated tunnelling times as a function of DC bias for the (a) biexciton and (b) exciton emission line. (c) Comparison of the biexciton and exciton tunnelling times from the previous panels.

allows for full quenching of the emission via rapid tunnelling of the charge carriers out of the QD. We use the relation

$$\frac{1}{\tau_{\text{measured}}} = \frac{1}{\tau_{\text{radiative}}} + \frac{1}{\tau_{\text{tunnelling}}} \quad (4.3)$$

to estimate the tunnelling time  $\tau_{\text{tunnelling}}$  via the measured decay time  $\tau_{\text{measured}}$  and the radiative decay time  $\tau_{\text{radiative}}$ , similar to Ref. [Har13]. For this measurement, we estimate the radiative decay time via the measured decay time at a DC bias equal to the turn-on voltage 0.70 V.

The resulting time constants are shown in Fig. 4.10. As expected for both, biexciton and exciton, the further the bias voltage is decreased from the turn-on, the more the tunnelling time decreases (corresponding to an increase in tunnelling rate) [Hel98, Fry00a, Har13]. As highlighted in Fig. 4.10c, the extracted tunnelling times follow a very similar trend for biexciton and exciton. The tunnelling times only diverge at bias voltages  $\leq 0.3$  V, potentially limited by the timing resolution of the experimental setup. Naively one would expect a biexciton tunnelling time reduced by a constant factor of 2 compared to the exciton, as the biexciton has twice as many charge carriers as the quantum dot—although potentially hampered by an increased ionisation energy from the electrons to the wetting layer for the biexciton [Fry00a].

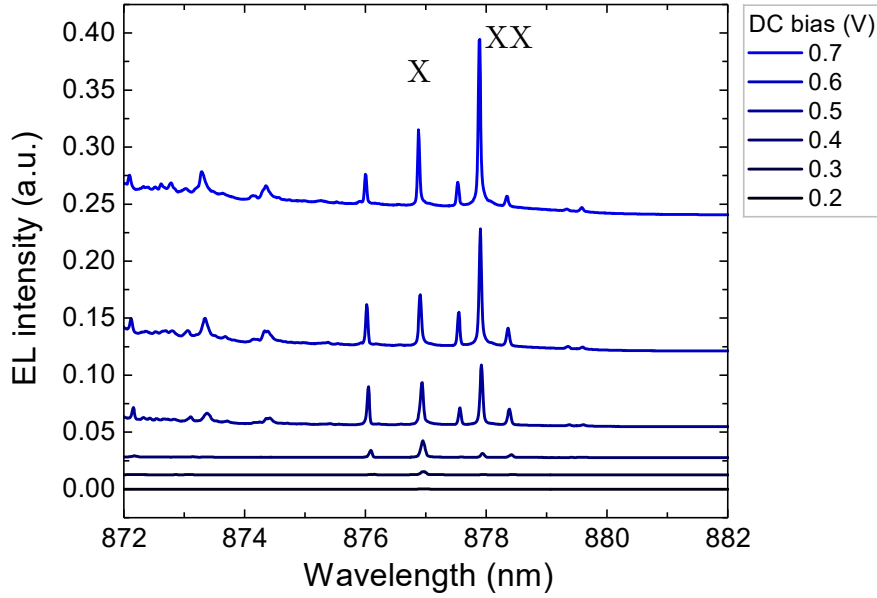


Figure 4.11: EL spectra as a function of DC bias and a fixed peak voltage. The spectra are offset from each other for visibility. The EL intensity reduces for reducing DC biases, dominated by non-radiative recombination via quantum tunnelling.

However, due to the non-uniform high-frequency electrical response of the driving setup, the experimental data and extracted tunnelling times do not offer sufficient measurement statistics to reveal this feature with statistical significance.

Corresponding spectra for the different DC biases are shown in Fig. 4.11, measured under the same driving conditions as for Fig. 4.9. For reducing DC biases, the EL intensities of the  $XX$  and  $X$  emission lines clearly reduce. Modelling the radiative and non-radiative recombination as competing exponential processes characterised by their respective decay times gives an estimate for the fraction of (bi-)excitons recombining radiatively of

$$\eta_{\text{radiative}} = \frac{\tau_{\text{tunneling}}}{\tau_{\text{tunneling}} + \tau_{\text{radiative}}} \quad (4.4)$$

for a given DC bias. For a DC bias of 0.2 V, this estimate yields values of 3% and 16% for the  $XX$  and  $X$  emission respectively, with the remaining carriers recombining non-radiatively.

Fig. 4.12a shows the measured EL intensity quantified via Lorentzian fits to the spectral emission peaks. For a DC bias of 0.2 V, the  $XX$  and  $X$  emission intensity reaches  $2 \times 10^{-5}$  and  $4 \times 10^{-3}$  of the respective intensity at a DC bias equal to the turn-on voltage. This drop in intensity is significantly lower than the above estimate. We attribute this to reduced effective peak voltages during the initialisation pulse. Although the nominal peak voltage is kept constant throughout the measurement series, the fast but finite electrical reactance of the diode likely reduces the effective peak voltage of electrical pulse trains with low DC biases.

The respective fitted centre wavelength and FWHM are shown in Figs. 4.12b and 4.12c. The centre wavelength shifts to longer wavelengths for lower DC biases due to the Stark effect [War07, Har13]. As the voltage changes from the fixed initialisation voltage down to DC bias within a clock cycle, the emission wavelength varies with the emission time. For the same reason, the recorded emission appears to be spectrally broadened for lower DC biases [War07]. In contrast, natural linewidth broadening due to the reduced decay time likely only plays a secondary role—e.g. a decay time of 28 ps (such as the  $X$  at 0.2 V) corresponds to a natural linewidth of 0.03 nm.

### 4.2.3 Pulsed generation of single photons at a 3 GHz clock rate

In a next step we substantially increase the clock rate for the pulsed, electrical operation of the device for ultrafast clocked applications. The device was driven at 3.05 GHz with driving pulses of amplitude  $V_{\text{pulse}} = 1.43$  V and nominal duty cycle of 7.5% ( $\sim 25$  ps). A DC bias voltage of  $V_{DC} = 0.15$  V is chosen to be far below the turn-on voltage  $V_T = 0.70$  V of the diode. Thus, charge carriers quickly tunnel out of the QD potential between driving pulses, quenching the optical emission [Ben05, Har13].

A time-resolved measurement of the resulting  $X$  electroluminescence is shown in Figs. 4.13a and Fig. 4.13a. We observe high contrast optical pulses with almost three orders of magnitude modulation of the emission intensity. Approximating the optical

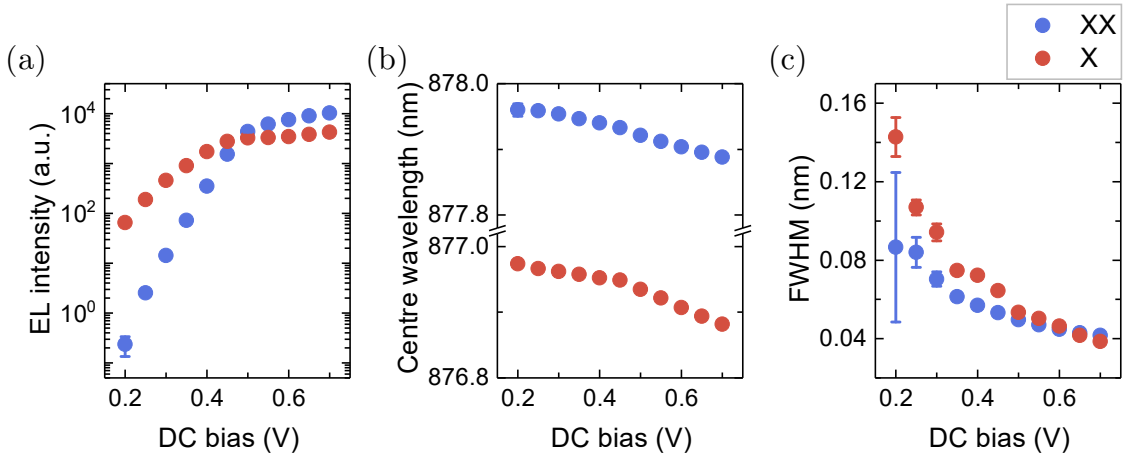


Figure 4.12: Emission characteristics extracted via Lorentzian fits to the biexciton and exciton emission lines of the measured spectra. (a) EL intensity is significantly reduced at low DC biases. (b) The centre wavelength shifts to lower energy for reduced DC biases due to the Stark effect [Fry00b, War07]. (c) FWHM. The QD emits while the voltage changes from the fixed initialisation voltage to the DC bias, leading to a spectrally broadened emission peak due to the Stark effect [War07].

emission pulse with a Gaussian temporal shape yields a FWHM of  $(100 \pm 2)$  ps, and fitting an exponential decay yields a lifetime of approximately 15 ps. This is in stark contrast to the 680 ps radiative lifetime as measured at 1 GHz, highlighting significant control over the emission time jitter. This strong reduction in decay time suggests non-radiative decay processes are dominant, attributed to efficient tunnelling of the charge carriers out of the QD enabled via a fast electrical response [Ben05].

The corresponding second order auto-correlation  $g^{(2)}(t)$ , measured for the same driving conditions, is shown in Fig. 4.13b. A value of  $g^{(2)}(0) = 0.268 \pm 0.002$  of the integrated zero-delay peak demonstrates the single photon character of the emission. The noticeable anti-bunching of the peaks adjacent to the zero-delay could imply the existence of long-lived charged or dark states [Ben05]. To our knowledge, this is the fastest reported clock rate for the generation of single photons [Buc12, Har13], entering the “super high frequency” radio band (SHF, comprising the 3–30 GHz

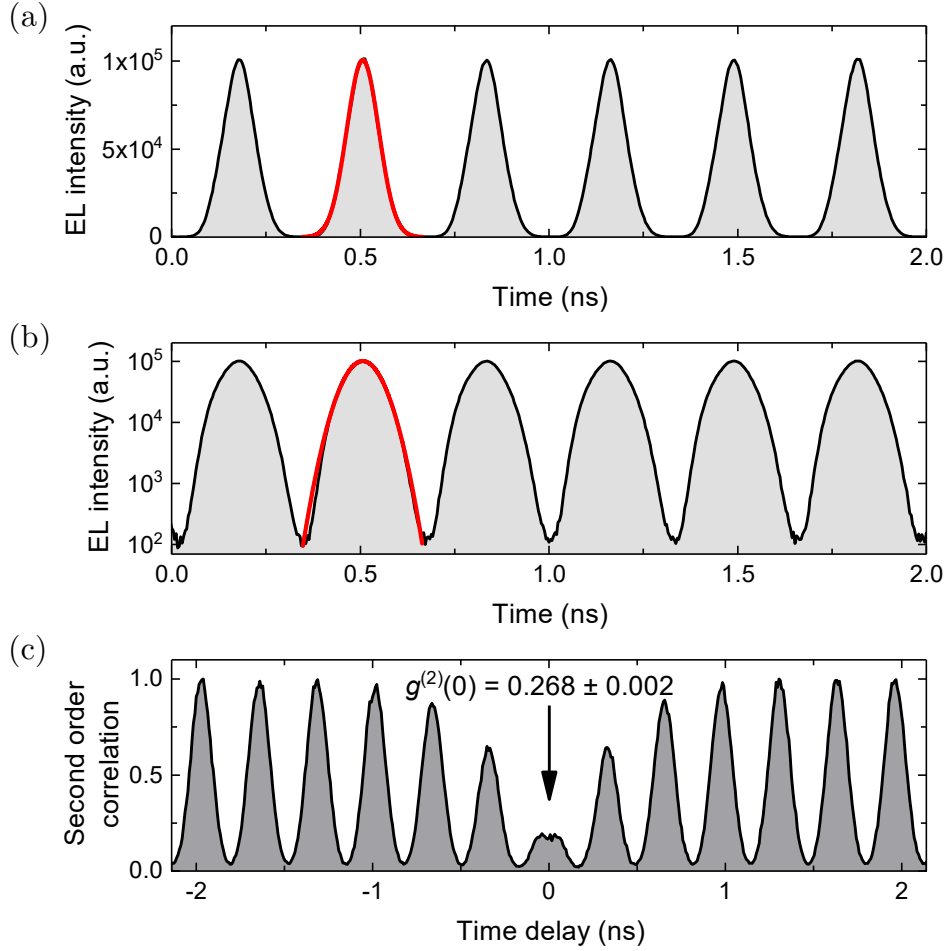


Figure 4.13: Gigahertz-clocked single photon generation. (a) Time-resolved electroluminescence of the  $X$  emission line driven at a 3.05 GHz clock frequency. A Gaussian fit (red line) reveals a FWHM of  $(100 \pm 2)$  ps. (b) Same data as in previous panel, now plotted on a logarithmic y-scale. The emission is modulated by almost three orders of magnitude within a clock period. (c) Corresponding second order correlation  $g^{(2)}$  measured for the same driving conditions. A value of  $g^{(2)}(0) = 0.268 \pm 0.002$  for the zero-delay peak indicates single-photon emission.

range [Int15]) for the first time. For comparison, the existing record of 2 GHz-clocked single photon generation has been presented by Hargart et al. [Har13]. In their reported experiment the single photon emission is modulated by only a factor of less than 20 during a 2 GHz driving period. Thus, the almost three orders of magnitude modulation we have reported above represents a modulation enhanced by a factor of  $\sim 50$  at a clock rate increased by a factor of more than 1.5, compared to the previous experiment. In addition, this strong modulation of the optical emission indicates that the sample could be driven at frequencies substantially higher than the presented 3 GHz. This could be verified in a future experiment using an electrical pulse generator capable of generating faster clock rates. In the same vein, a detection system with a time jitter further reduced from the current 50 ps FWHM could aid in revealing even faster modulation of the single-photon emission.

Via Eq. 4.4 we can estimate the fraction of exciton recombining radiatively as  $\eta_{\text{radiative}} = 2\%$ . The remaining 98% recombine non-radiatively due to the high tunnelling probability. Overall, although the photon collection efficiency is reduced when reducing the decay times in this driving mode, this could be partially compensated by correspondingly increased clock rates. Moreover, depending on the application, the reduced timing uncertainty of the emission could prove beneficial [Har13].

#### 4.2.4 Multiphoton contributions due to re-excitation

A spectrum of the emission, driven under these same conditions, is shown in Fig. 4.14a. Here, the Stark shift is strong enough to produce a splitting of the peak, most likely into emission at the initialisation voltage and emission at DC bias, similar to the situation in Ref. [War07]. (Note that the FSS of the QD was measured to be  $10\ \mu\text{eV} \approx 0.006\ \text{nm}$ , much smaller than the splitting observed from the Stark effect.)

Under these driving conditions the  $X$  emission peak splits into two components, emission during the driving pulses and emission after the driving pulses (Fig. 4.14a, inset). The latter is shifted to longer wavelengths as the reduced voltage between driving pulses induces a relative Stark shift [War07]. By comparing the EL intensity

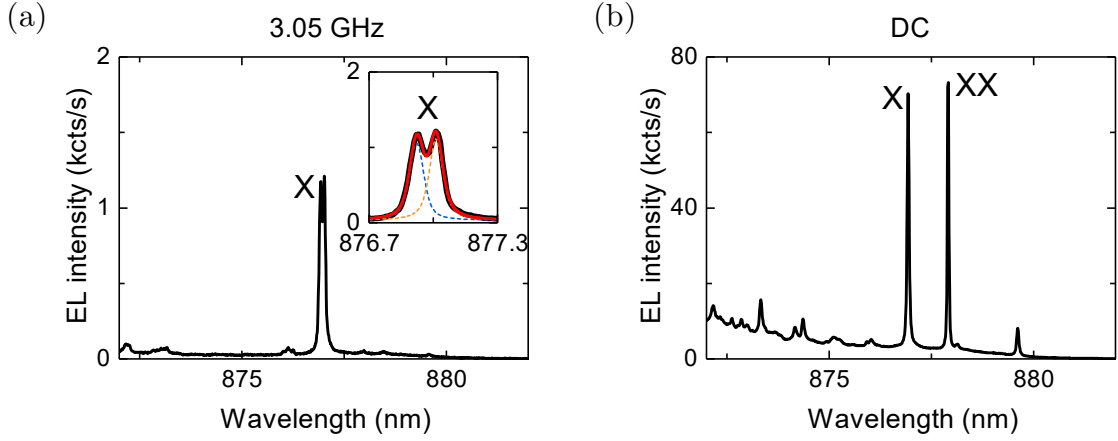


Figure 4.14: EL spectra for different driving conditions. (a) Spectrum at the conditions for 3.05 GHz-clocked single photon emission. The inset is a zoom-in on the  $X$  emission line, revealing double peak due to a temporal Stark shift [War07, Ben08]. The red line is a double Voigt fit (individual Voigt curves in blue and orange) to the spectrum. (b) Driven in DC near the  $X$  saturation current.

of the two components, we can estimate an upper bound for the contribution of re-excitation during the driving pulse to the non-zero  $g^{(2)}(0)$ . According to the double Voigt curve fit to the spectrum, emission during (after) the driving pulse contributes 48 % (52 %) to the total  $X$  emission. In the limit of strong pumping to the  $X$  state, such that re-excitation during the driving pulse is fast compared to the radiative lifetime, we can approximate a Poissonian contribution to the zero-delay peak of the  $g^{(2)}$ , written as the photon state [Scu97]

$$|\phi_{|\alpha|^2}\rangle = e^{-|\alpha|^2/2} \sum_{n=0}^{\infty} \frac{\alpha^n}{\sqrt{n!}} |n\rangle \quad (4.5)$$

where  $|\alpha|^2$  is the mean photon number. In contrast, QD emission after the driving pulse is emitted in the single photon Fock state  $|1\rangle$ , as re-excitation is suppressed. With the total two-photon state in a clock period as a superposition of these two components, weighted by the respective relative contribution to the measured spectrum (and disregarding absolute scaling w.r.t the vacuum state, as it does not

affect the  $g^{(2)}(0)$  value)

$$|\psi\rangle = |\phi_{0.48}\rangle + 0.52|1\rangle \quad (4.6)$$

we can calculate

$$g^{(2)}(0) = \frac{\langle\psi|\hat{a}^\dagger\hat{a}^\dagger\hat{a}\hat{a}|\psi\rangle}{\langle\psi|\hat{a}^\dagger\hat{a}|\psi\rangle^2} = 0.23 \quad (4.7)$$

for the zero-delay peak, where  $\hat{a}^\dagger$  and  $\hat{a}$  are the creation and annihilation operators respectively. Comparing this to the measured  $g^{(2)}(0)$  of  $0.268 \pm 0.002$  as described in the previous section, we conclude that re-excitation during the driving pulse is likely the dominating contribution to the non-zero  $g^{(2)}$ , with background emission constituting only a secondary factor. As is evident from the estimation here, the strong tunneling induced in this mode, reducing the intensity of the single photon emission, magnifies the relative contribution of re-excitation. Multiphoton emission due to re-excitation could potentially be lowered by further reducing the temporal duration of the initialisation pulse. However, a quantitative experimental comparison of driving pulse length is challenging, as electrical resonances distort the voltage that is effectively applied across the intrinsic diode region. Note that finite carrier mobilities means that it takes on the order of 10 ps to deplete the QD layer from charge carriers after the end of the electrical initialisation pulse [Kan17]. To what degree charge carriers would repopulate the QD during this time period then likely depends on the exact experimental settings.

As the nominal voltage generated at the pulse generator is distorted during propagation to the diode active region, it would be interesting to determine the effective voltage across the intrinsic region from the measured spectral Stark shift. However, for above-band optical excitation, we did not detect any  $X$  photoluminescence when applying DC biases far enough below turn-on, as optically excited charge carriers preferentially formed other excitonic configurations [War00].

As concluded above, an additional contribution to the non-zero component of the  $g^{(2)}(0)$  value is likely background wetting layer emission. Fig. 4.14b shows the sample driven electrically near  $X$  saturation, highlighting the existence of background

emission. This could be improved via a future sample containing QDs with less spectral overlap with the wetting layer.

## 4.3 Conclusion

In this chapter we reported the design and fabrication of a QD LED that enables super-high-frequency operation for the 3.05 GHz-clocked generation of single photons for the first time. For electrically driven devices, a key achievement is the high bandwidth entangled-LED mesa structure itself, which places no particular constraints on the optical device design or collection optics. As a result, the design could be combined with other approaches to enhance the decay rate and reduce the timing jitter. In particular, the design offers potential for integration with optical cavities, allowing for enhanced radiative decay rates via the Purcell effect [Dou10, Din16, Liu18, Liu19, Wan19]. Considering the presented single photon emission with a 100 ps temporal FWHM, further enhancements could enable driving frequencies significantly beyond the demonstrated 3.05 GHz.

For practical applications, another major achievement is the precise temporal control of the charge carrier injection and non-radiative recombination. We take further advantage of the capabilities of this ultrafast QD LED in the next chapter, where we use the same device to demonstrate the possibility of high brightness and high fidelity generation of entangled photons via gigahertz-clocked driving pulses.



# 5 Entangled photon generation beyond the continuous driving limit

This section describes theoretical and experimental results on entangled photon generation via an active reset of an atom-like few-level system. Key results presented in this section have been published in Ref. [Mül20]. The sample was grown by Ian Farrer and David A. Ritchie; and processed by Joanna Skiba-Szymanska, Jonathan R. A. Müller, and Ginny Shooter. Optical experiments, data analysis, and the theoretical model were realised by Jonathan R. A. Müller with valuable contributions from R. Mark Stevenson and with guidance from Andrew J. Shields.

In this chapter we focus on the dynamics behind entangled photon generation from a few-level quantum system. The generation of entangled photons from quantum dots in particular has recently been the subject of rapid progress, with experimental implementations demonstrating entangled photon generation with high fidelities [Hub18a] and collection efficiencies [Che18, Liu19, Wan19]. These achievements have relied on advances in quantum dot growth, optical excitation techniques, and device design. However, another factor that has received little attention is the temporal driving technique.

In the following, we investigate how the temporal driving method affects the emission rate and entanglement fidelity of entangled photons generated from an atom-like quantum system, in this case a quantum dot. Crucially, we demonstrate how the system may emit entangled photons at a higher emission rate and fidelity when the QD is reinitialised while still optically active, compared to an optimally continuously driven system. In the first part of this chapter, we employ a rate equation model

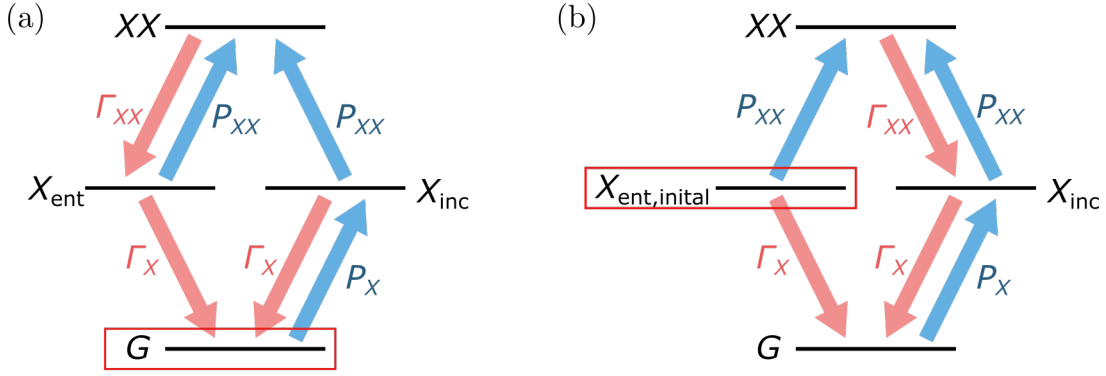


Figure 5.1: Schematic of the rate equation model. (a) Starting from the ground state. The population is transferred between the different levels via the pump rate  $P_{XX/X}$  and the radiative decay rate  $\Gamma_{XX/X}$ . A photon is emitted whenever the system decays radiatively (orange arrows). (b) Describing entanglement to an initial emitted  $XX$  photon, starting in the entangled exciton state. Here,  $X_{ent,initial}$  describes entanglement only to the initially emitted  $XX$  photon, not to any other biexciton photons.

to explore the system dynamics. Subsequently, we demonstrate the possibility of entangled pair rates beyond the continuous driving limit, for strong and weak pumping. In the second part, we then support the theoretical predictions via an experimental implementation of this novel gigahertz-clocked driving technique in the weak pumping regime.

## 5.1 Rate equation model

We begin by considering the excitation and radiative cascade dynamics of an atomic three-level system [Asp81], as in this case, of a QD. As described in Ch. 2.2.1, the biexciton state decays via an intermediate neutral exciton superposition state, resulting in two consecutively emitted, polarization-entangled photons [Ben00, Ste06].

To capture these entanglement dynamics in a numerical model, in addition to the biexciton state  $XX$  and the ground state  $G$ , we differentiate between entangled neutral exciton state  $X_{ent}$ , non-entangled neutral exciton state  $X_{inc}$ . Here,  $X_{ent}$  is defined

as an exciton state entangled to a previously radiatively emitted biexciton photon. Hence, rather than focussing on the polarisation or spin state of the exciton, we instead model the entanglement property of the neutral exciton (cf. [Ste12a]).

The resulting four-level rate equation system is visualized in Fig. 5.1a and can be written as

$$\begin{aligned}
 \frac{d}{dt}XX(t) &= -\Gamma_{XX} \cdot XX(t) + P_{XX} \cdot [X_{\text{inc}}(t) + X_{\text{ent}}(t)] \\
 \frac{d}{dt}X_{\text{ent}}(t) &= \Gamma_{XX} \cdot XX(t) - (\Gamma_X + P_{XX}) \cdot X_{\text{ent}}(t) \\
 \frac{d}{dt}X_{\text{inc}}(t) &= -(\Gamma_X + P_{XX}) \cdot X_{\text{inc}}(t) + P_X \cdot G(t) \\
 \frac{d}{dt}G(t) &= \Gamma_X \cdot [X_{\text{inc}}(t) + X_{\text{ent}}(t)] - P_X \cdot G(t),
 \end{aligned} \tag{5.1}$$

where  $P_{XX/X}$  are the time-dependent pump rates for the respective eigenstate, and  $\Gamma_{XX/X}$  are the corresponding radiative decay rates. The terms  $XX(t)$ ,  $X_{\text{ent}}(t)$ ,  $X_{\text{inc}}(t)$ , and  $G(t)$  are the respective populations of the corresponding QD states. The pump terms describe the system for any non-resonant pumping, i.e. either electrical or non-resonant optical excitation. In the following analysis, we mostly focus on the electrical excitation case, although the discussion can be easily adapted to the non-resonant optical excitation case as well. We also focus on situations where the voltage across the diode is either at or above the turn-on voltage. Thus, unlike the situation in the previous chapter, tunnelling of the charge carriers out of the quantum dot is assumed to be negligible [Fry00a]. Moreover, in this idealised model we omit dephasing via spin scattering from  $X_{\text{ent}}$  to  $X_{\text{inc}}$  for now. Finally, we can calculate the time-dependent emission rate of polarization-entangled photon pairs as  $\Gamma_{\text{pair}} = \Gamma_X \cdot X_{\text{ent}}(t)$ .

## 5.2 Active reset driving for superequilibrium entangled pair rates

To further investigate the system dynamics, we assign the experimentally observed radiative decay rates  $\Gamma_{XX} = \tau_{XX}^{-1} = (300 \text{ ps})^{-1}$  and  $\Gamma_X = \tau_X^{-1} = (500 \text{ ps})^{-1}$  (cf. Fig. 5.11)

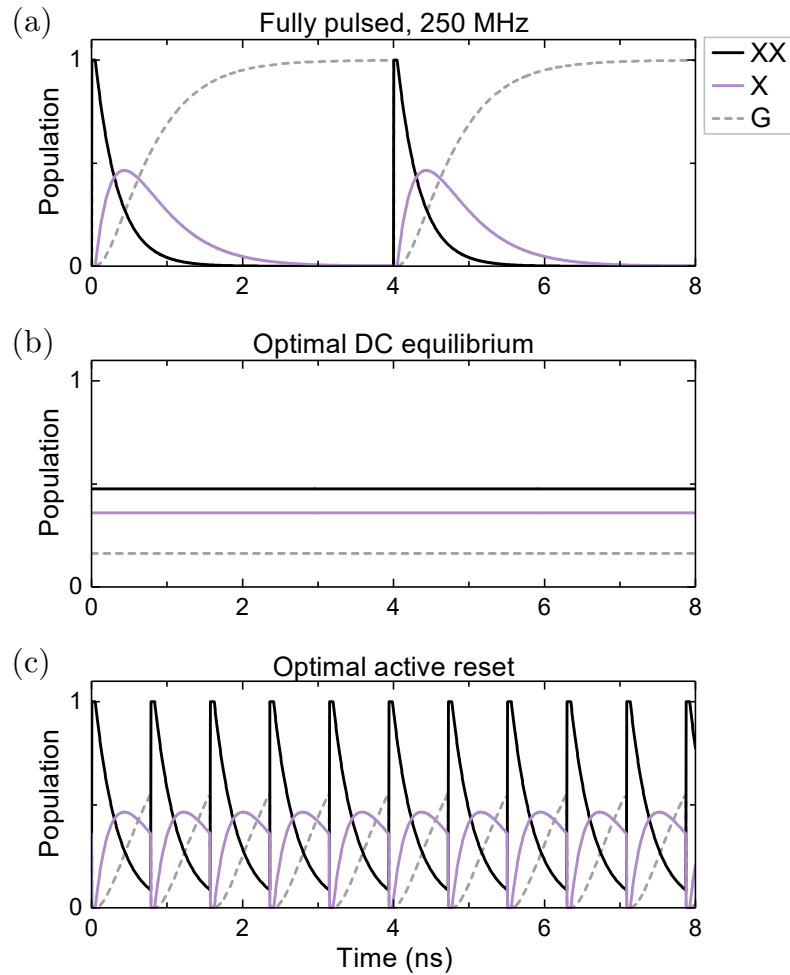


Figure 5.2: QD populations for different driving modes, calculated via a rate equation model. (a) Conventional full-cycle pulsed driving. The QD is reinitialised after the population has reached zero. (b) Conventional DC driving. Populations are shown for the DC pump rate that maximizes the entangled pair emission rate. (c) Active reset regime. The quantum dot is reinitialised into the biexciton state before the QD population reaches zero.

and subsequently solve the rate equations numerically using standard methods [Vir20]. Fig. 5.2a shows the modelled biexciton, exciton, and ground state population, driven at a slow 250 MHz clock rate via 50 ps rectangular initialisation pulses. Although not modelled here, a lower limit for the duration of an electrical initialisation pulse is given by the time the charge carriers take to populate the QD layer when exposed to a typical forward voltage. This is on the order of 10 ps, governed by finite carrier mobility in the semiconductor [Kan17]. We approximate the modelled pump rate as  $P_{XX/X} \rightarrow \infty$  during the driving pulse to ensure pumping to the biexciton state and  $P_{XX/X} = 0$  for the remainder of the clock period (corresponding to the system in the flat-band condition). When the QD is excited to the  $XX$  state in the limit of low driving frequency, practically complete radiative decay to the ground state is observed during a clock cycle. However, a substantial fraction of the clock cycle is spent at the tail of the emission cascade with high ground state population and low emission brightness.

In contrast, for continuous driving the QD population is in equilibrium, with the  $XX$  and  $X$  states always populated and an always non-zero emission intensity. Fig. 5.2b shows the equilibrium QD population at the optimum distribution (here referred to as ‘optimal DC’), i.e. at the pump rate that maximises the entangled pair generation rate. To find the optimal DC driving conditions, the pump rates  $P_{XX}$  and  $P_X$  are set to be equal  $P_{XX} = P_X = P$  [Hei17]. Fig. 5.3 shows the resulting QD population equilibrium and entangled pair generation rate as a function of the pump rate. If  $P_{XX}$  is increased beyond the DC optimum, re-excitation of the  $X_{\text{ent}}$  state to the  $XX$  state dominates, reducing  $X_{\text{ent}}$  and thus entangled pair emission. Crucially, at the DC power that maximises the entangled pair emission rate, the distribution of the QD population in the DC equilibrium means that only a minority (43% in this case) of the emitted photons form part of a biexciton-exciton cascade, resulting in a reduced relative fraction of entangled pair emission.

We now introduce a novel active reset (AR) driving scheme based on two core considerations: Firstly, to reset entanglement at a given clock cycle, the QD does not need to return to the ground state. Instead, it is sufficient to reinitialise directly to the

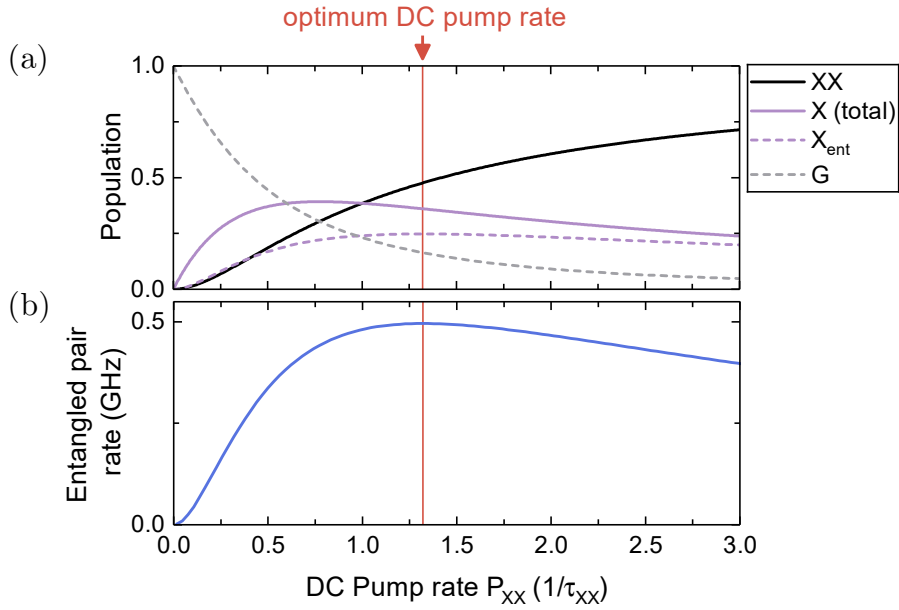


Figure 5.3: Optimum entangled pair generation in equilibrium. (a) QD equilibrium population and (b) entangled pair generation rate as a function of DC pump rate  $P$  of the system. In the given model, the system reaches an optimum equilibrium entangled pair rate of 496 MHz at a pump rate of  $P_{\text{optimum}} = 1.71 P_{X,\text{sat}} = 1.32/\tau_{XX}$ .

biexciton state—the initial state of the biexciton-exciton cascade—while the QD is still optically active. Secondly, resetting the QD before the population has fully cascaded to the ground state allows for an increased entangled-pair emission brightness, as the low-brightness periods in the tail of the emission are eliminated.

Fig. 5.2c shows the quantum dot driven in the AR regime at a fast 1.27 GHz clock rate. The QD is perpetually kept in an optically active state with high  $XX$  or  $X$  populations and low ground state population below 0.56—eliminating dark periods and resulting in a high emission brightness. For entangled photon pairs generated from solid state sources, the entanglement fidelity will typically reduce for an increasing emission delay between the two photons, owing to the interaction of the QD with the solid-state environment [Ste12a, Tro14]. By reinitialising the QD state early, the generation of weakly entangled pairs at longer emission delays can be avoided.

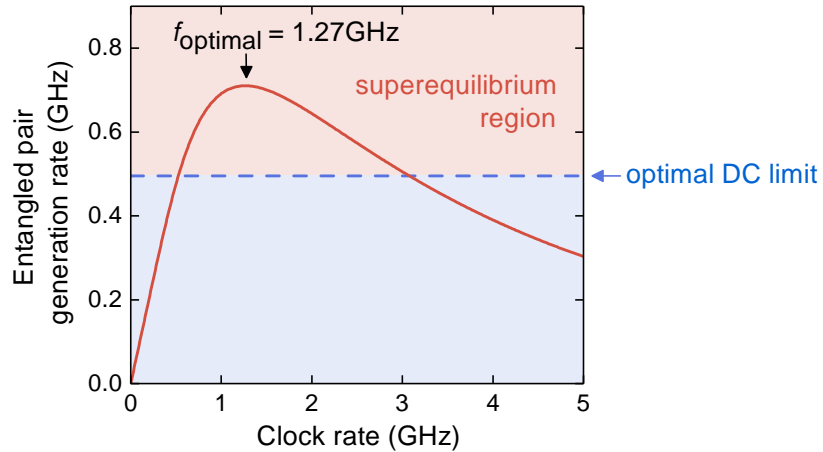


Figure 5.4: Superequilibrium entangled pair rate for active reset driving. Modelled time-averaged entangled photon pair generation rate as a function of driving clock rate. The pair generation rates accessible in DC driving are indicated by the light-blue-shaded area. An optimum clock rate is given at 1.27 GHz, where the entangled pair rate exceeds the optimum DC rate by 43%.

A key consideration for AR driving is the optimum clock rate required to maximize the number of entangled photon pairs over time, highlighted in Fig. 5.4. Kantner et al. [Kan17] have shown that for the generation of single photons, an optimum clock rate exists, after which the emission rate decreases. We find an analogous result for the case of entangled photon generation. At clock periods longer than the lifetimes of both, biexciton and exciton, the entangled-pair generation rate naturally scales approximately linearly with the repetition rate. At faster clock rates, the pair generation rate in turn reduces due to the non-zero lifetime of the excitonic states, as the delayed emission of the entangled photon pair is interrupted prematurely before the radiative cascade completes. Perhaps surprisingly, as the figure shows we find a range of frequencies between 520 MHz and 3.07 GHz for which the entangled pair generation rate becomes superequilibrium, exceeding the equilibrium limit for continuous driving. For the investigated radiative decay rates, the entangled pair generation rate reaches a maximum at a clock rate of  $f_{\text{optimal}} = 1.27$  GHz where it exceeds the optimum DC pair generation rate by 43%. At this frequency, the clock period is close to the combined lifetime ( $\tau_{XX} + \tau_X$ ) of the two transitions. Even the

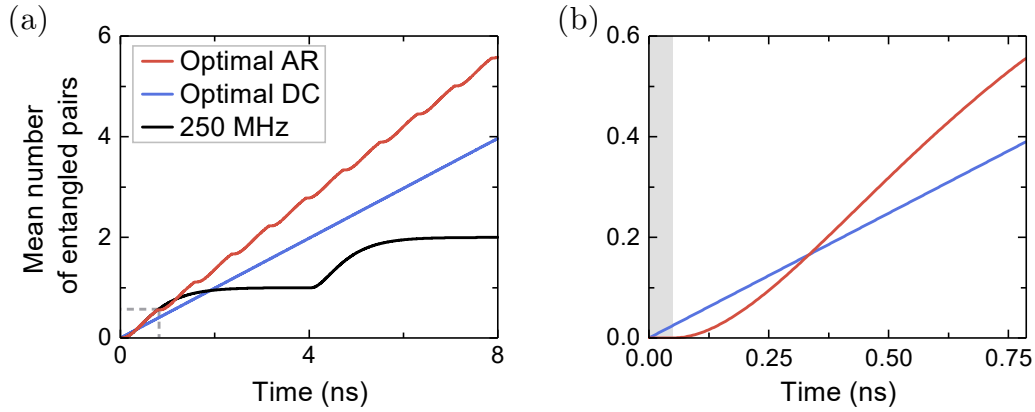


Figure 5.5: Mean cumulative number of entangled photon pairs emitted over time for the driving modes of Fig. 5.2. (a) Shown for multiple clock periods and (b) magnification of the first 1.27 GHz clock period, marked by the dashed grey rectangle in panel a. The grey-shaded region in panel b marks the 50 ps initialisation pulse in AR driving. Despite an initially lower entangled pair generation, AR driving exceeds the optimum DC pair generation by 43 % after one clock period.

highest-clocked experimental demonstrations operate at clock rates below 500 MHz, with none approaching the optimum [Ste12b, Zha15].

The mean number of emitted entangled pairs  $\langle N_{\text{pair}}(t) \rangle$  until time  $t$  is easily calculated by integrating the time-dependent entangled pair rate

$$\langle N_{\text{pair}}(t) \rangle = \int_0^t \Gamma_{\text{pair}}(t') dt' \quad (5.2)$$

and shown in Fig. 5.5 for the different driving modes. This plot again highlights the superequilibrium entangled pair rates in AR, producing more entangled photons than both, DC or fully pulsed driving. Note that for AR driving, due to the early reinitialisation of the QD state, the mean number of emitted photon pairs per clock cycle is less than one (0.56 in this model) at  $f_{\text{optimal}}$ . In contrast for the 250 MHz clock rate, (asymptotically) one entangled pair is emitted each clock cycle. Notably, panel 5.5b highlights the dynamics of AR driving within a clock period: During the strong initialisation pulse, the entangled pair emission is zero, giving the continuous DC driving a head start at the beginning of the clock period. However, during

the subsequent free evolution in AR driving, the system is free from detrimental reexcitation, leading to an overall superior mean entangled pair emission by the end of the clock period. In practice, further external factors affect the overall efficiency as well, such as device electrical bandwidth and collection efficiency (cf. Chs. 4.2.3 and 2.4.3).

### 5.2.1 Superior entanglement fidelity via active reset

Next, we focus on the resulting entanglement fidelity. A measurement of the two-photon state is given by the subsequent detection of an  $X$  photon after a  $XX$  photon. To reflect this, we modify the rate equation 5.1 such that, instead of starting from the ground state, the starting point is the emission of a  $XX$  photon, with the QD system now in an entangled exciton state  $X_{\text{ent,initial}}$ . Furthermore, a subtle change in the definition of the rate equation levels is required. We now differentiate the two  $X$  levels regarding their entanglement to the already emitted  $XX$  photon only—not to any other  $XX$  photon. As a consequence, once the system has left the  $X_{\text{ent,initial}}$  state there is no return to this state, because future  $XX$ - $X$  cascades will not be entangled to the initially emitted  $XX$  photon. The resulting rate equation is visualized in Fig. 5.1b, and can be written as [Ste12a]

$$\begin{aligned}
 \frac{d}{d\tau} XX(\tau) &= -\Gamma_{XX} \cdot XX(\tau) + P_{XX} \cdot (X_{\text{inc}}(\tau) + X_{\text{ent}}(\tau)) \\
 \frac{d}{d\tau} X_{\text{ent}}(\tau) &= -(\Gamma_X + P_{XX}) \cdot X_{\text{ent}}(\tau) \\
 \frac{d}{d\tau} X_{\text{inc}}(\tau) &= \Gamma_{XX} \cdot XX(\tau) - (\Gamma_X + P_{XX}) \cdot X_{\text{inc}}(\tau) + P_X \cdot p_G \\
 \frac{d}{d\tau} G(\tau) &= \Gamma_X \cdot (X_{\text{inc}}(\tau) + X_{\text{ent}}(\tau)) - P_X \cdot G(\tau).
 \end{aligned}
 \tag{5.3}$$

In addition, we are now computing the system as a function of the time delay between  $XX$  and  $X$  emission  $\tau = t_X - t_{XX}$  instead of absolute time, and are consequently calculating the derivative w.r.t.  $\tau$  as well.

We can then calculate the two-photon density matrix as a function of time delay after the emission of an  $XX$  photon via

$$\begin{aligned}\hat{\rho}(\tau) &= \frac{X_{\text{ent,initial}}(\tau) \hat{\rho}_{\text{ent}} + X_{\text{inc}}(\tau) \hat{\rho}_{\text{mm}}}{X_{\text{ent,initial}}(\tau) + X_{\text{inc}}(\tau)} \\ &= k_{\text{ent}} \hat{\rho}_{\text{ent}} + k_{\text{mm}} \hat{\rho}_{\text{mm}},\end{aligned}\tag{5.4}$$

with the density matrices for the entangled state  $\hat{\rho}_{\text{ent}}$  and a maximally-mixed state  $\hat{\rho}_{\text{mm}}$  defined as

$$\hat{\rho}_{\text{ent}} = \frac{1}{2} \begin{pmatrix} 1 & 0 & 0 & 1 \\ 0 & 0 & 0 & 0 \\ 0 & 0 & 0 & 0 \\ 1 & 0 & 0 & 1 \end{pmatrix} \quad \text{and} \quad \hat{\rho}_{\text{mm}} = \frac{1}{4} \begin{pmatrix} 1 & 0 & 0 & 0 \\ 0 & 1 & 0 & 0 \\ 0 & 0 & 1 & 0 \\ 0 & 0 & 0 & 1 \end{pmatrix}\tag{5.5}$$

respectively, as well as the (time-dependent) fraction of entangled  $k_{\text{ent}}$  and maximally-mixed photon pairs  $k_{\text{mm}}$

$$k_{\text{ent}} = \frac{X_{\text{ent,initial}}(\tau)}{X_{\text{ent,initial}}(\tau) + X_{\text{inc}}(\tau)}\tag{5.6}$$

$$k_{\text{mm}} = \frac{X_{\text{mm}}(\tau)}{X_{\text{ent,initial}}(\tau) + X_{\text{inc}}(\tau)}.\tag{5.7}$$

Note that both, the numerator and the denominator of  $k_{\text{ent}}$  and  $k_{\text{mm}}$  are time-dependent. In the density matrix representation, the fidelity  $f$  to a maximally entangled two-photon state  $\rho_{\text{ent}}$  is defined via [Joz94]

$$f := \left[ \text{tr} \sqrt{\sqrt{\hat{\rho}_{\text{ent}}} \hat{\rho} \sqrt{\hat{\rho}_{\text{ent}}}} \right]^2.\tag{5.8}$$

Inserting Eq. (5.4) then gives

$$\begin{aligned}f(\tau) &= \left[ \text{tr} \sqrt{\sqrt{\hat{\rho}_{\text{ent}}} (k_{\text{ent}} \hat{\rho}_{\text{ent}} + k_{\text{mm}} \hat{\rho}_{\text{mm}}) \sqrt{\hat{\rho}_{\text{ent}}}} \right]^2 \\ &= \left[ \text{tr} \sqrt{k_{\text{ent}} \sqrt{\hat{\rho}_{\text{ent}}} \hat{\rho}_{\text{ent}} \sqrt{\hat{\rho}_{\text{ent}}} + k_{\text{mm}} \sqrt{\hat{\rho}_{\text{ent}}} \hat{\rho}_{\text{mm}} \sqrt{\hat{\rho}_{\text{ent}}}} \right]^2 \\ &= \left[ \text{tr} \sqrt{k_{\text{ent}} \hat{\rho}_{\text{ent}}^2 + k_{\text{mm}} (\hat{\rho}_{\text{ent}}^2/4)} \right]^2 \\ &= k_{\text{ent}} + \frac{k_{\text{mm}}}{4}.\end{aligned}\tag{5.9}$$

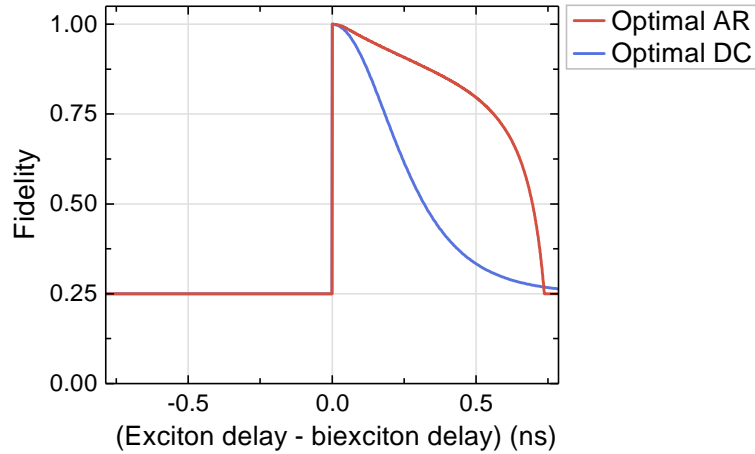


Figure 5.6: Fidelity to a maximally entangled Bell state vs emission delay between exciton and biexciton, for optimal AR driving (red) and optimal DC driving (blue). AR driving maintains a high fidelity even for a maximized pair emission rate.

As one would expect, we verify that a fully entangled state produces a fidelity of 1, while a maximally-mixed state produces a fidelity of 0.25. Here we performed the fidelity calculation for the case of an emitter with zero FSS, producing entangled photons in the static  $\phi^+$  Bell state. For an arbitrary FSS replacing the definition of  $\rho_{\text{ent}}$  with an evolving two-photon state (see Eq. (2.15)) yields the same overall result for Eq. (5.9) after subsequent projection onto that same time-evolving entangled two-photon state.

To factor in the time-dependent pump rate in AR driving, we subsequently need to multiply the posterior populations calculated via Eq. (5.3) by the prior probability of measuring the system in the initial state  $X_{\text{ent,initial}}$ . This is given by the probability of detecting an  $XX$  photon at absolute time  $t$ , defined via  $\Gamma_{XX} XX(t)$  (where  $XX(t)$  is calculated by solving Eq. (5.1)).

The resulting entanglement fidelities for the optimum AR and DC conditions are shown in Fig. 5.6. Notably, the fidelity in AR driving is significantly increased over the DC fidelity. This stems from the fact that the fidelity in optimum AR driving is limited only by additional  $XX$  emission during the short (50 ps) initialisation pulse. Yet at the end of the clock period, the strong initialisation pulse reliably destroys any

remaining entanglement by transferring the QD population back to the  $XX$  state. When integrating the fidelity over all two-photon coincidences within a clock cycle, the overall fidelity in AR driving comes to 89.4%. The entanglement fidelity in DC driving, in contrast, is fundamentally limited by constantly competing, uncorrelated emission from continuous excitation. Consequently, the overall fidelity integrated over the same time period comes to 72.7%, significantly reduced from the value in AR driving. Altogether, this model demonstrates the feasibility of overcoming the limits on entanglement fidelity and entangled-pair brightness imposed by DC or full-cycle pulsed driving.

### 5.2.2 Active reset in the weak pumping regime

In the previous sections we focussed exclusively on the strong pumping regime for active reset driving, where the entangled pair emission saturates as shown in Fig. 5.7. Unlike continuous driving (see Fig. 5.3), in AR driving there is thus no optimum pumping rate, as any sufficiently strong pumping rates will produce the saturation entangled pair rate. In this case of strong pumping rates during initialisation, we can always expect the QD to be in the  $XX$  state after the initialisation pulse. As a consequence, the entanglement is naturally destroyed at the end of the clock period by transferring the remaining entangled exciton population  $X_{\text{ent}}$  back into the  $XX$  state. However, such strong pumping rates are not always accessible experimentally. In particular for non-resonant excitation (incl. electrical excitation), undesirable optical emission from the wetting layer may become dominant at high pumping rates.

In the following we investigate the system dynamics for reduced pumping rates during the initialisation pulse. At reduced pumping rates, a non-zero  $X_{\text{ent}}$  population carries over to the next clock cycle, as shown in Fig. 5.8a. Consequently, the two-photon emission is partially correlated at the end of a clock cycle, remaining above the value of 0.25 for maximally mixed emission (black line in Fig. 5.8b). However, depending on the physical implementation this could be potentially alleviated by dephasing during initialisation, such as observed due to charge noise [Tro14]. We model this

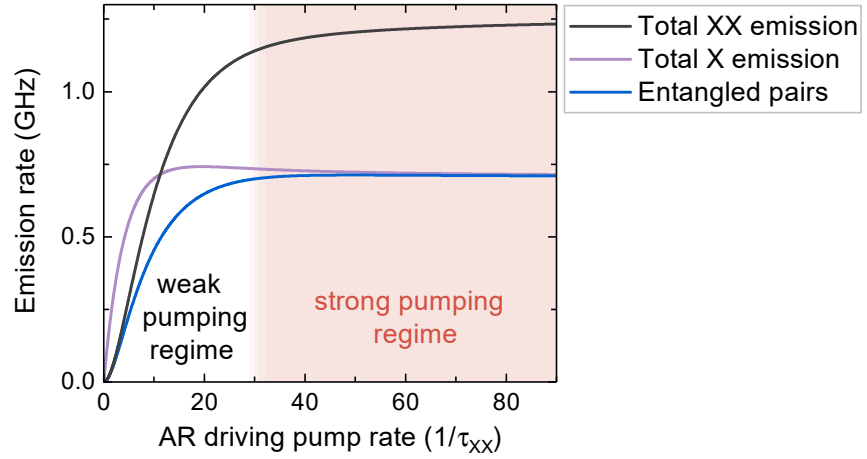


Figure 5.7: Time-averaged emission intensity in AR driving as a function of pump rate  $P$  during the initialisation pulse. The entangled pair emission plateaus when the biexciton is reliably initialised each clock cycle (region shaded in light-pink).

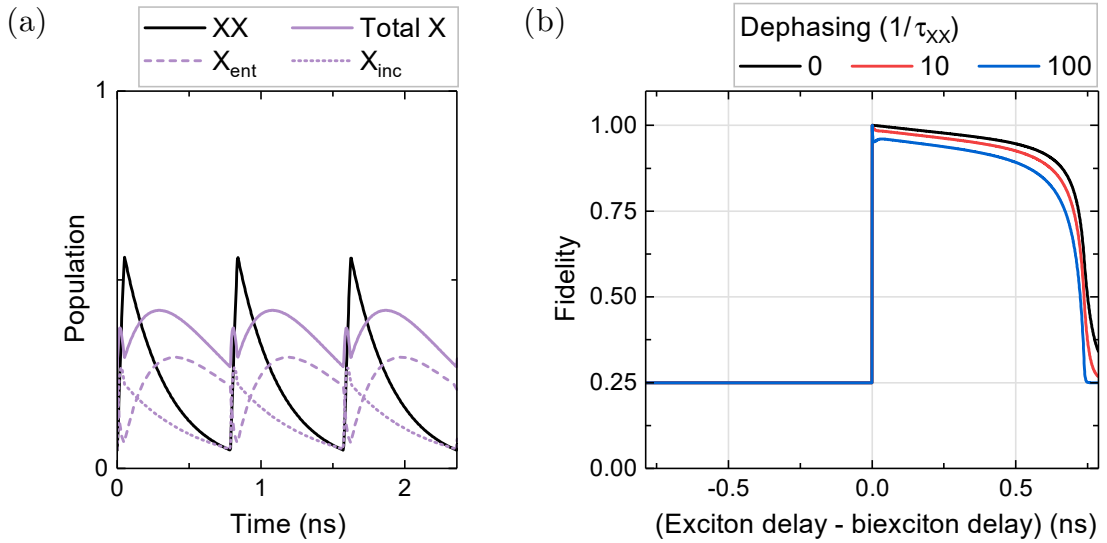


Figure 5.8: (a) QD populations in AR driving at a reduced driving pump rate of  $P_{XX/X} = 10\Gamma_{XX}$  and no dephasing. The entangled exciton population  $X_{\text{ent}}$  does not reach zero during initialisation. (b) Fidelity to a maximally entangled Bell state for different dephasing rates during initialisation. At zero dephasing, the emission is still partially correlated at the end of a clock period (positive end of the x-axis).

by adding a spin scattering rate from  $X_{\text{ent}}$  to  $X_{\text{inc}}$  during the initialisation pulse to the rate equation model. For a moderate dephasing rate (red line in Fig. 5.8b), the remaining correlation is nearly fully eliminated at the end of the clock cycle. Thus, even though in the weak pumping regime the entanglement is not inherently destroyed between clock cycles, the dephasing dynamics of the system may be sufficient to compensate for this. At the same time, even strong dephasing during initialisation only moderately reduces the fidelity (blue line). Likewise, the calculated overall fidelity reduces only moderately to 93.0% for strong dephasing, from 97.4% at zero scattering, highlighting the robustness of AR driving. As a side note: the substantial  $X_{\text{inc}}$  population in Fig. 5.8a may lead one to expect lower fidelities in the weak driving regime. However, those clock cycles where the QD is in the  $X_{\text{inc}}$  state are the ones where it does not reach the  $XX$  state. Consequently, in these clock cycles no two-photon coincidence is registered due to the lack of  $XX$  photon, and thus the measured entanglement fidelity is not impacted. Similarly, the security of a potential QKD protocol remains unaffected as no entanglement will be distributed in these clock cycles.

A central motivation for AR driving is the generation of entangled pairs at superequilibrium rates, i.e. at higher emission rates than possible in continuous DC driving. Naturally, at reduced AR pump rates, the entangled pair rate does not necessarily exceed the DC optimum. For closer investigation, Figs. 5.9a and 5.9b show the modelled entangled pair rate for AR and DC driving in the weak pumping regime. To produce the respective  $XX/X$  emission intensity as plotted on the x-axes, the pump rates of AR and DC driving are each adjusted accordingly, while keeping all other parameters unchanged. Crucially, this figure demonstrates that for any chosen exciton or biexciton intensity, AR driving produces more entangled photons than continuous DC driving. In other words, AR driving consistently maintains the superequilibrium entangled pair rates in the weak pumping regime as well. For identical  $XX$  intensities, AR driving produces the same number of entangled pairs as DC driving in the limit of zero intensity, up to 1.51 times near  $XX$  saturation. For identical  $X$  intensities, the entangled pair rate in AR driving reaches from 1.22 times

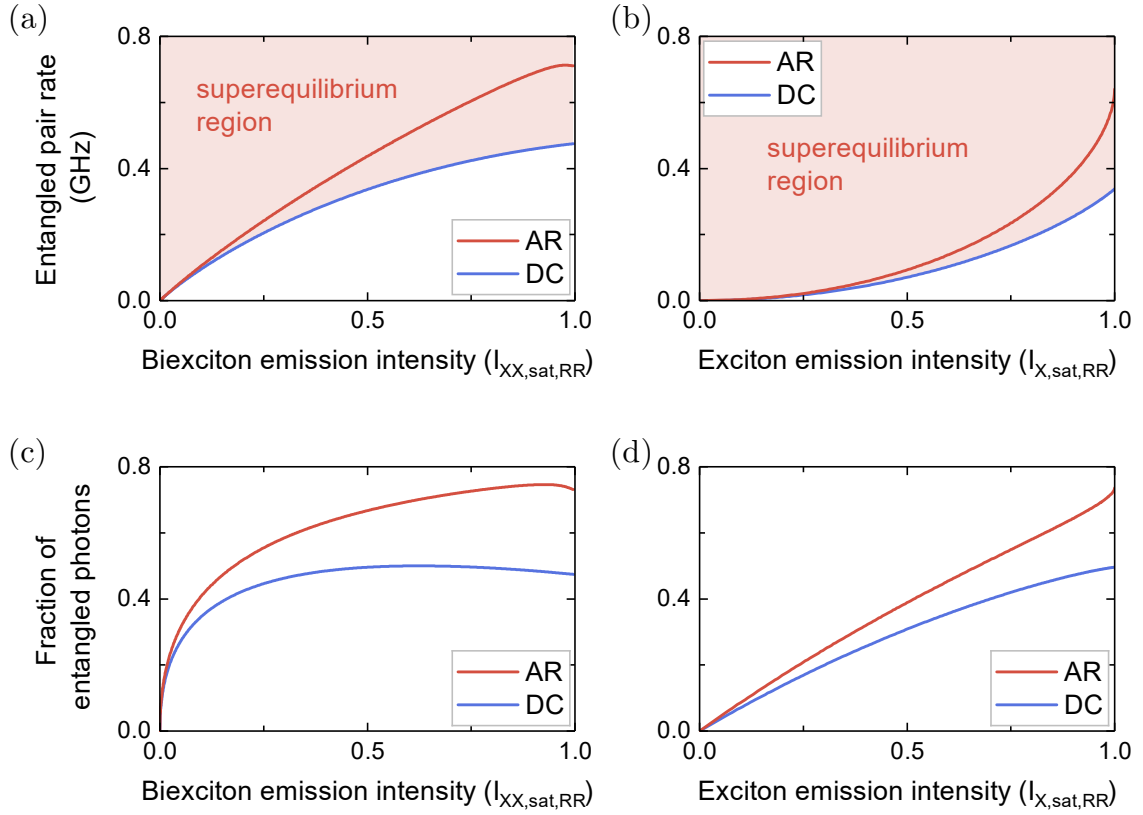


Figure 5.9: Modelled entangled pair rate as a function of (a) biexciton emission intensity and (b) exciton emission intensity. AR driving produces superequilibrium entangled pair rates (exceeding the respective rate in DC, light-pink shaded region) for all driving conditions. (c) and (d) Efficiency of entangled photon generation. Emitted entangled photons as a fraction of all emitted  $XX$  and  $X$  photons, as a function of exciton emission intensity and biexciton emission intensity. AR driving is consistently more efficient than DC driving. X-axis emission intensities are given in terms of the biexciton and exciton saturation intensity in AR driving,  $I_{XX,sat,AR}$  and  $I_{X,sat,AR}$ , respectively (cf. Fig. 5.7). The clock frequency in AR driving is fixed to 1.27 GHz, only the driving pump rate is varied.

the DC rate in the limit of zero intensity up to 1.89 more at saturation. Note that for both, AR driving and DC driving, the maximum entangled pair rate only occurs beyond the  $X$  saturation intensity and is therefore not shown in this plot.

Likewise, Figs 5.9c and 5.9d show that AR driving produces entangled photons more efficiently than DC driving. Thus, altogether AR driving produces more entangled photons while, at the same time, producing less non-entangled photons as well.

## 5.3 Experimental active reset

After establishing the theoretical advantages of AR driving via the rate equation model, we now turn our attention towards the experimental implementation of AR driving, in a proof-of-principle demonstration.

### 5.3.1 Driving conditions

We employ the same high-frequency optimised QD LED presented in Ch. 4, mounted in the Helium vapour cryostat and cooled to 6 K. Fig. 5.10 shows the EL spectrum in different driving modes. The biexciton and exciton emission was centered at 876.8 nm and 877.8 nm respectively. Near  $X$  saturation in DC (5.10a), in the employed sample the spectrum exhibits a substantial background contribution from the wetting layer. In addition to running the diode in AR, we performed a reference DC measurement for comparison.

The AR and DC experiments were performed in the weak pumping regime to mitigate background contribution. The DC current was set to 27 % of the  $X$  saturation current, or approximately 17 % of the predicted optimum DC pumping intensity. The driving voltage for the AR measurement was chosen such that the resulting integrated exciton and biexciton emission lines reach 100.4 % and 115.5 % intensity, respectively, compared to the DC setting (Figs. 5.10b and 5.10c). To this end, the sample was electrically excited at a clock rate of 1.15 GHz ( $T = 868$  ps period) with initialization pulses of amplitude  $V_{pulse} = 0.6$  V and nominal duty cycle 5% ( $\sim 43$  ps). The DC bias of  $V_{DC} = 0.6$  V just below the turn-on voltage was chosen to ensure that, outside

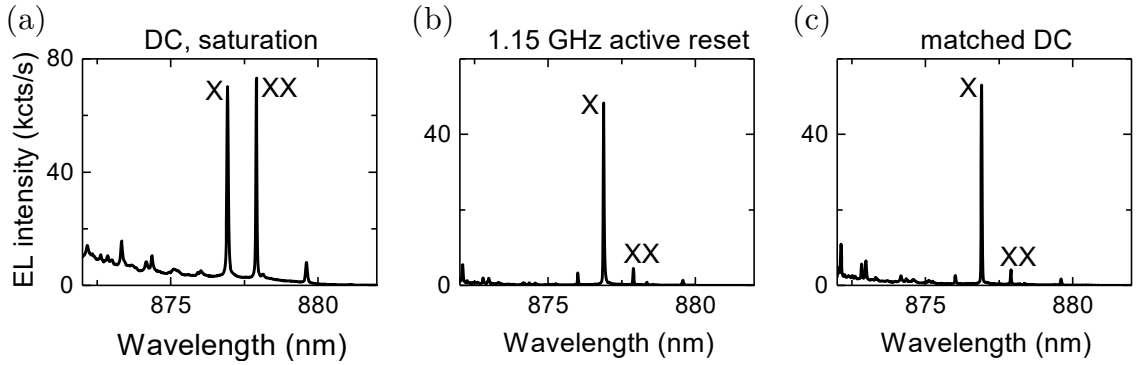


Figure 5.10: EL spectra for different driving conditions. (a) Driven in DC near the  $X$  saturation current. (b) Spectrum at the chosen active reset conditions. (c) Spectrum at the reference DC conditions matched to the AR settings. Note that in AR driving the  $X$  peak is slightly broadened compared to the DC settings, thus appearing lower despite a near-identical total intensity when integrated over the linewidth.

of the initialisation pulse, the diode remains below turn-on even at high frequency driving.

Figure 5.11 show the time-resolved EL for the biexciton and exciton transitions under fully pulsed excitation and under the chosen active reset driving conditions. The  $XX$  lifetime remains largely unaffected, while a weak decrease of the  $X$  lifetime implies a low tunneling rate out of the QD. The emission intensity for both transitions remains non-zero throughout, operated in the weak pumping regime analogous to the situation described in Fig. 5.8a.

The clock rate of 1.15 GHz chosen for experimental AR was slightly reduced from the theoretical optimum of 1.27 GHz to ease requirements on the device bandwidth and avoid electrical resonances. Fig. 5.12 highlights that the theoretical model still predicts an entangled pair generation rate of more than 99% of the optimal value for this reduced clock rate, remaining within the superequilibrium regime.

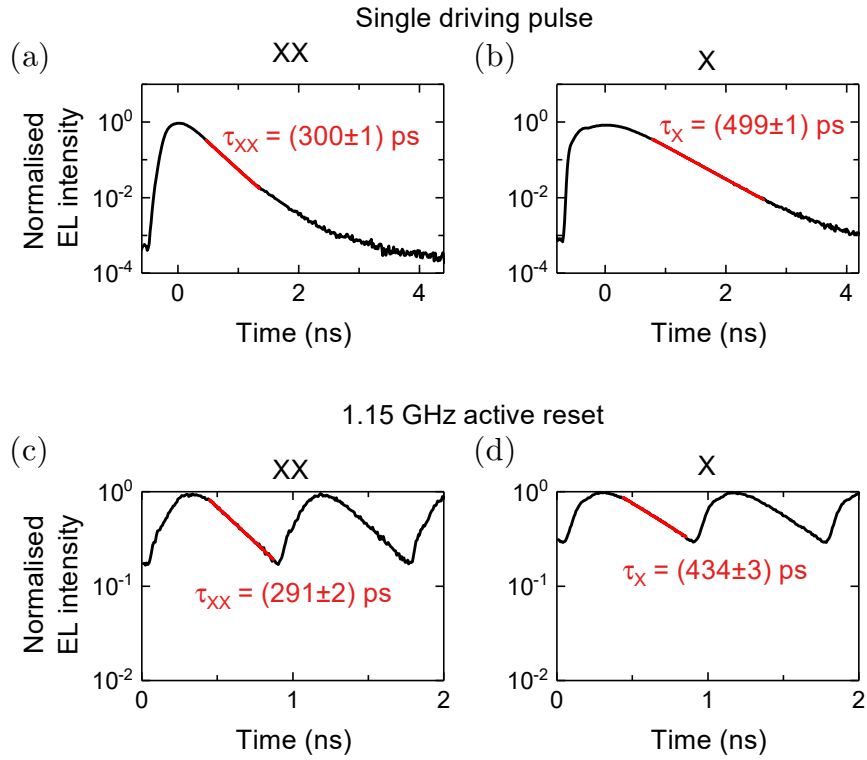


Figure 5.11: EL intensity as a function of time. (a) biexciton and (b) exciton emission line under excitation from a single 200 ps electrical driving pulse. (c) biexciton and (d) exciton emission line at the chosen active reset settings. In this case the EL emission is re-initialized before the QD population reaches zero. Mono-exponential fits used to extract the lifetimes are shown in red.

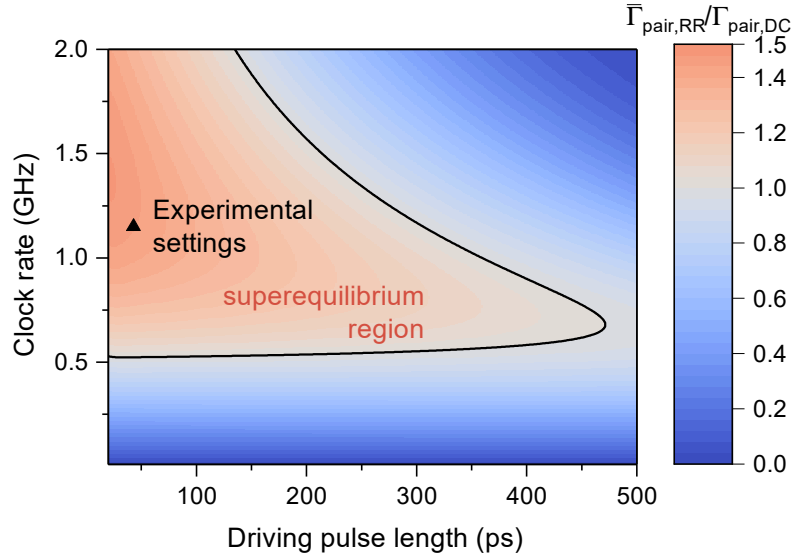


Figure 5.12: (Time-averaged) entangled pair generation advantage  $\bar{\Gamma}_{\text{pair,RR}}/\Gamma_{\text{pair,DC}}$  as a function of clock rate and driving pulse length for optimum pumping rates. The red sections mark the superequilibrium region where active reset allows for enhanced entangled pair generation rates compared to optimum equilibrium parameters. Fig. 5.4 is a cross-section of this figure at a fixed driving pulse length of 50 ps. The triangle marks the nominally employed experimental settings.

### 5.3.2 Optical setup

The E-LED emission was collected confocally as described in Ch. 3.2. The subsequent optical measurement setup is illustrated in Fig. 5.13. The eigenbasis of the QD was determined as described in Ch. 3.2.1, and we subsequently measured the  $XX$  and  $X$  emission in five orthogonal polarisation bases to calculate the fidelity to a maximally entangled Bell state (see Eq. (2.15)). The SSPD detection times  $t_{XX}$  and  $t_X$  were recorded in 2 ps bins w.r.t. the clock signal of the pulse generator using a multi-channel, time-correlated single-photon-counting module [Wah98]. Overall, the detection system had a time jitter of 50 ps FWHM. The relative time delays of the three SSPDs channels were calibrated using a pulsed diode laser. Finally, the

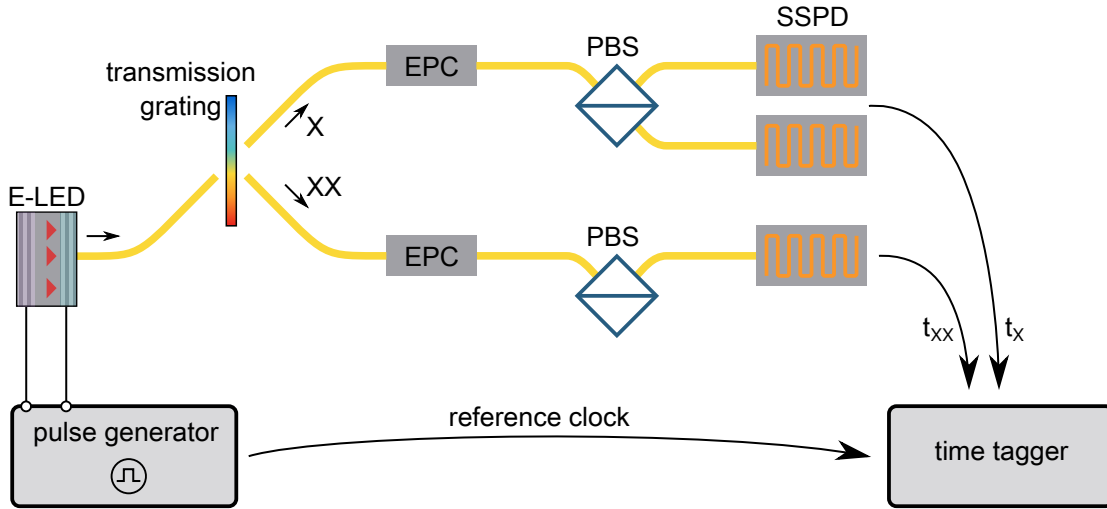


Figure 5.13: Optical setup to characterise active reset driving. The E-LED was driven by the electrical pulse generator. The resulting  $XX$  and  $X$  emission was spatially separated via a transmission grating. The emission was projected onto the desired polarisation basis via the electrically driven polarisation controllers (EPCs) and polarising beam splitters (PBSs), and subsequently detected via the SSPDs. The detection time of all biexciton photons  $t_{XX}$  and exciton photons  $t_X$  was recorded w.r.t. the clock of the pulse generator.

detection events of the independent SSPD channels were downsampled to 16 ps bins and correlated during post-processing.

## 5.4 Experimental results

To gain an understanding of the measurement results, we first analyse the data acquired during DC driving. Figs. 5.14a and 5.14b show the resulting normalised biexciton-exciton second-order correlation function  $g^{(2)}(t_{XX}, t_X)$  as a function of  $XX$  emission time ( $t_{XX}$ ) and  $X$  emission time ( $t_X$ ) relative to the clock of the (in this case constant) voltage source. The modelled second-order correlation is calculated following the rate equation methodology explained at the beginning of this chapter. The intermediate time-resolved QD populations are convolved with the experimental 50 ps Gaussian timing jitter of the detectors. To determine the pump rate we insert

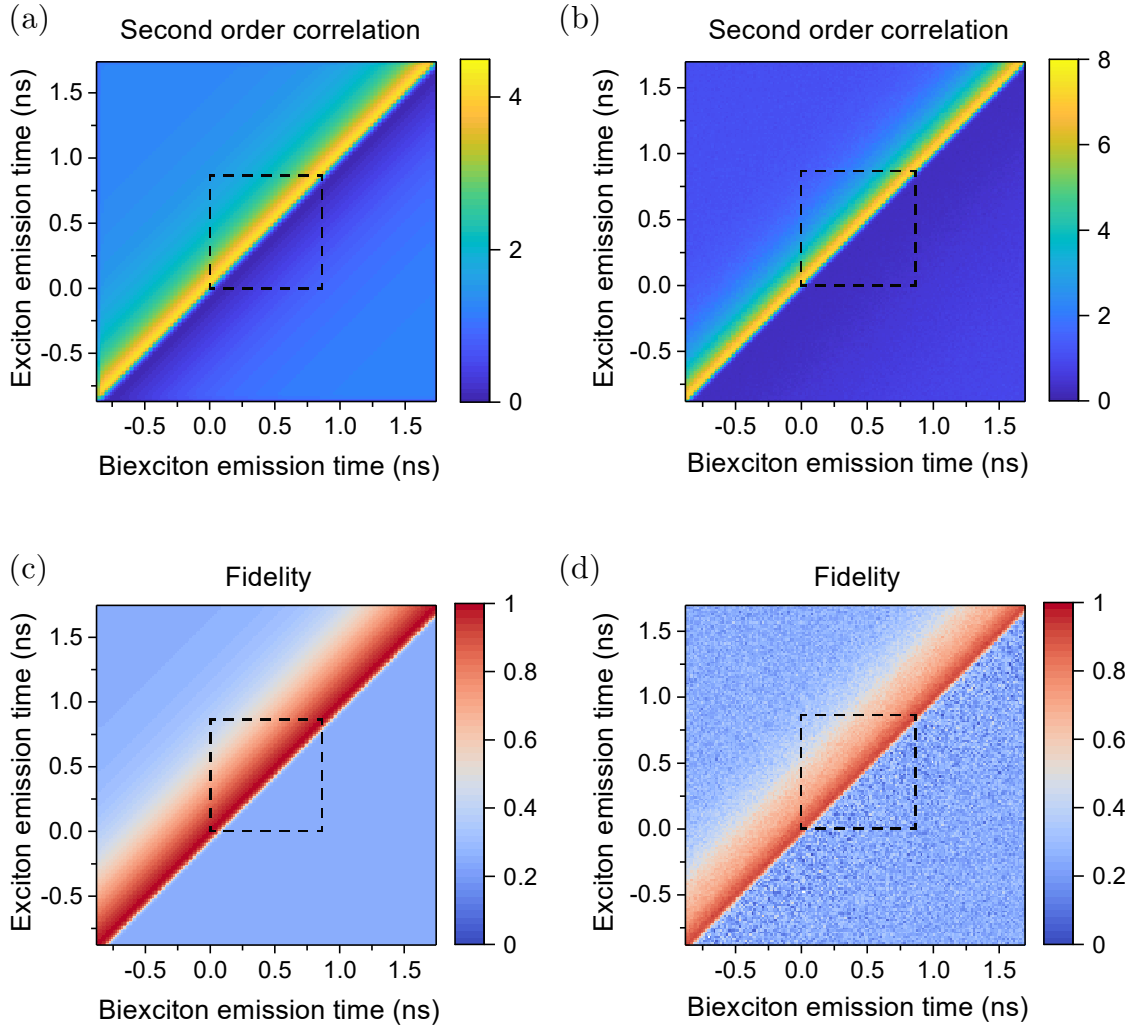


Figure 5.14: Generation of entangled photon pairs in DC driving. (a) Modelled and (b) experimental unpolarised biexciton-exciton second order correlation  $g^{(2)}(t_{XX}, t_X)$  as a function of biexciton emission time  $t_{XX}$  and exciton emission time  $t_X$ . (c) Modelled and (d) experimental corresponding fidelity to a maximally entangled evolving Bell state  $f(t_{XX}, t_X)$ . The fidelity remains highly entangled within the driving cycle, and is sharply quenched towards the end of the cycle  $t_X \rightarrow T$ . The total fidelity within a 1.15 GHz period (dashed black square) is  $(71.2 \pm 1.0)\%$ . The data are plotted in bins of  $16 \text{ ps} \times 16 \text{ ps}$ ; experimental bins with insufficient photon counts are coloured in white.

the experimentally used value of 27 % of the saturation pump rate into the model. The modelled correlations serve only as a qualitative reference, as a precise fit of all involved parameters was not performed at this point. In particular, external noise contributions were modelled via a flat  $0.2\Gamma_{XX}$  chosen as the dephasing term. As is, the modelled correlations serve as a useful tool to understand the origin of various features in the experimental measurement.

Due to the cascaded emission of the  $X$  photon after the  $XX$  photon, the correlation events within a clock period are naturally biased towards the upper triangle region where  $t_X > t_{XX}$ . In the DC measurement, the driving voltage is invariant over time, thus the second order correlation is translationally symmetric along the diagonal.

Figs. 5.14c and 5.14d show the fidelity to a maximally entangled evolving Bell state, extracted from co- and cross-polarized correlations measured in the respective polarization bases as laid out in Eq. (2.15) and with a QD fine structure splitting of  $S = 10\mu\text{eV}$ . Notably the model qualitatively reproduces the features of the experimental data. Although there is no inherent clock cycle in this DC measurement, for comparison with AR driving the dashed black square in each of the panels marks the boundaries of a single 1.15 GHz clock period. Naturally, the entanglement fidelity is not confined to the clock cycle. Nevertheless for comparison, the overall fidelity, integrated over all two-photon coincidences within this clock period comes to  $(71.2 \pm 1.0)\%$ . The error is estimate by assuming Poissonian detection statistics and taking into account systematic errors in the polarisation calibration. The fidelity reaches a maximum value of  $(92.5 \pm 1.9)\%$  in the  $(16\text{ps} \times 16\text{ps})$  bin with the highest entanglement.

In analogy to the DC measurement, Figs. 5.15a and 5.15b show the resulting normalised biexciton-exciton second-order correlation function for the AR experiment. The GHz-clocked character of the driving mode is directly apparent, as the driving voltage is no longer invariant over time. Consequently, the correlation is segmented into separate clock cycles. At the same time, unlike for fully pulsed driving, the  $g^{(2)}$  value remains non-zero throughout the clock cycle.

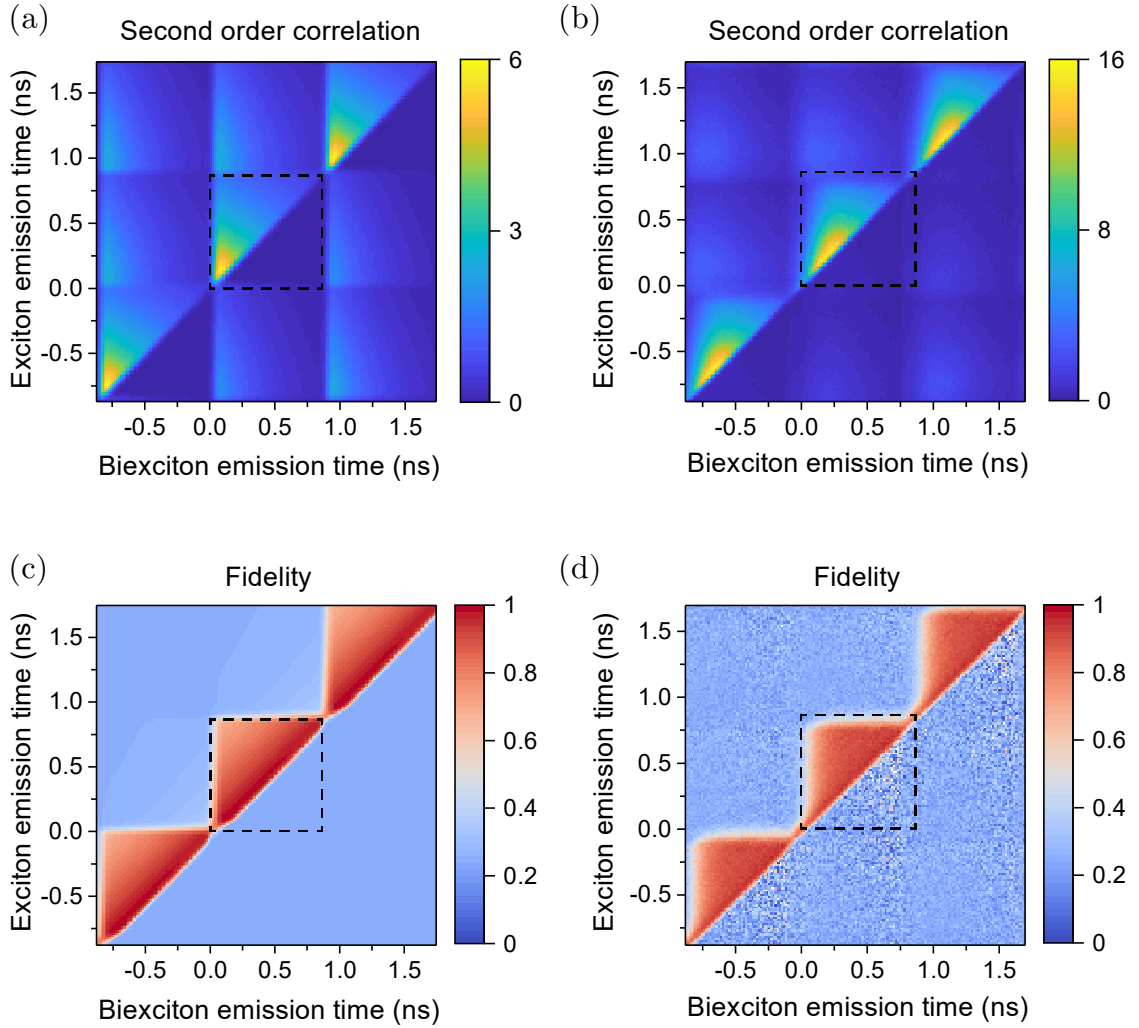


Figure 5.15: Generation of entangled photon pairs at a 1.15 GHz repetition rate. The dashed black square highlights photon pairs emitted within the same driving cycle. (a) Modelled and (b) experimental unpolarised biexciton-exciton second order correlation  $g^{(2)}(t_{XX}, t_X)$  as a function of biexciton emission time  $t_{XX}$  and exciton emission time  $t_X$ . (c) Modelled and (d) experimental corresponding fidelity to a maximally entangled evolving Bell state  $f(t_{XX}, t_X)$ . The fidelity remains highly entangled within the driving cycle, and is sharply quenched towards the end of the cycle  $t_X \rightarrow T$ . The total measured fidelity within a cycle is  $(79.5 \pm 1.1)\%$ . The data are plotted in bins of  $16 \text{ ps} \times 16 \text{ ps}$ ; experimental bins with insufficient photon counts are coloured in white.

Figs. 5.15c and 5.15d show the corresponding fidelity to a maximally entangled evolving Bell state. For the rate equation model, the dephasing rate during the initialisation pulse was set to  $10\Gamma_{XX}$ . The resulting modelled fidelity is in qualitative agreement with the experimental data. If we choose a lower dephasing rate during initialisation in the model, the polarisation correlation carries on beyond the boundaries of the clock period. This indicates that the experimental quenching of the entanglement could be aided by dephasing within the system.

The emission reaches a maximum measured fidelity of  $(95.8 \pm 1.3)\%$  and remains above the classical limit of 50% for the majority of the cycle, indicating electrically driven photon pair generation at a record 1.15 GHz clock rate. The maximum fidelity is similar to the maximum value of  $(92.5 \pm 1.9)\%$  in DC driving, in agreement with the presented theoretical model as neither driving mode limits the maximum entanglement fidelity at zero exciton-biexciton emission time delay (cf. Fig. 5.6). The overall entanglement fidelity, integrated over all photon pairs detected within the same driving cycle (including the ‘lower triangle’ at  $t_X < t_{XX}$ ), comes to  $f = (79.5 \pm 1.1)\%$ . For an entanglement-based QKD protocol, this value yields a quantum bit error rate of  $(13.6 \pm 0.7)\%$  [Sca09], well within the 27.6% limit required for secure quantum communication [Cha02]. Notably, no postselection is required in this driving mode — weakly entangled photon pairs at longer time delays are avoided naturally, as the entanglement is actively reset at the beginning of each cycle. Finally, at the edges of the driving cycle, the entanglement is abruptly reduced towards the classically uncorrelated value of 25%. Crucially, the measured overall entanglement fidelity significantly exceeds the overall fidelity of  $f_{DC} = (71.2 \pm 1.0)\%$  for the DC measurement.

An essential factor for the performance of QKD systems are independent polarizations for photons emitted across subsequent clock cycles, in order to maintain a low quantum bit error rate [Sca09]. Fig. 5.16 shows the mean entanglement fidelity as a function of the number of clock cycles between  $XX$  photon and  $X$  photon detection. Importantly, only photon pairs emitted within the same clock cycle are entangled. Photon pairs emitted across different clock cycles in turn yield a mean fidelity close

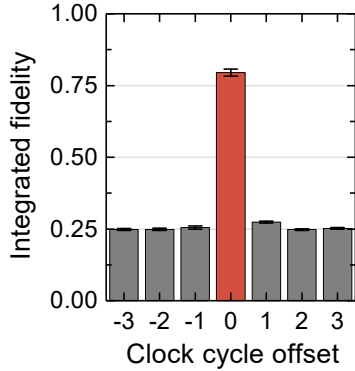


Figure 5.16: Reliable reset of entanglement. Integrated measured entanglement fidelity in AR driving as a function of clock cycles between biexciton emission and exciton emission. The integrated fidelity is non-classical only for photon pairs emitted within the same clock cycle.

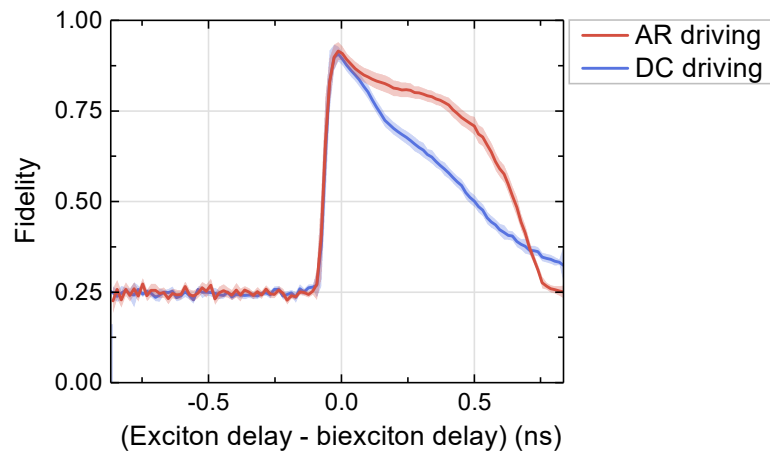


Figure 5.17: Comparison of the entanglement fidelity for AR and DC driving. Histogram of the measured entanglement fidelity as a function of the exciton photon detection delay after the biexciton photon,  $t_{X-XX} = t_X - t_{XX}$ . The fidelity in AR driving for coincidences emitted within the same cycle (red line) remains substantially higher than in DC driving (blue line) for the majority of the cycle. Shaded ribbons indicate the respective estimated standard error based on Poissonian detection statistics and estimated setup drifts in polarization.

to the 25% mark of fully uncorrelated light. This implies that the QD state is reset efficiently at the beginning of each cycle, such that the entanglement does not carry over from one clock cycle to the next. Though reinitialisation to the  $XX$  state is dominant, other unentangled initial states may be formed due to the statistical nature of non-resonant excitation, in particular in the weak pumping regime.

For pairs detected within the same clock cycle, the measured fidelity as a function of time delay between the two photons (shown in Fig. 5.17) resembles the concave shape predicted via the rate equation model in Fig. 5.6. For time delays approaching the end of the 868 ps repetition period, entanglement is quickly quenched. As we are operating the weak pumping regime, this could be a combination of efficient reinitialisation and dephasing, as discussed in Ch. 5.2.2. Remarkably, as predicted the measured fidelity in AR driving remains non-classical for longer time delays than in DC driving. At the same time, the fidelity in DC driving remains significantly above 25% at the end of the repetition period, thus carrying over an undesirable polarization correlation into the next clock cycle.

#### 5.4.1 Experimental superequilibrium entangled pair rates

Finally, we return to the theoretical prediction of superequilibrium entangled pair rates in AR driving compared to DC. We compare the measured entangled photon pair intensity in AR and DC, accumulated as a function of time delay relative to the clock signal, shown in Fig. 5.18. The number of entangled photon pairs is estimated by approximating the QD emission as a mixed state consisting of maximally entangled, and uncorrelated photon pairs (cf. Eq. (5.9)). The data were normalized by the total number of detected two-photon coincidences in the respective experimental run, such that the number of entangled pairs can be compared for the same emission intensity in both AR and DC. This compensates for the slightly reduced biexciton intensity in the matched DC driving mode as well as any drifts in setup efficiency between the two runs. The form of the curves resembles those in Fig. 5.5, with a constant pair emission rate for DC driving. For AR the rate is highest during the central part of the clock period. The measurements show an entangled photon

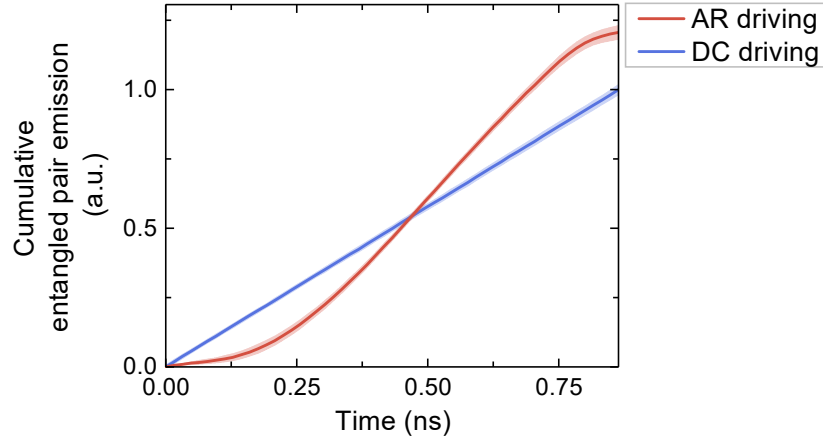


Figure 5.18: Cumulative entangled pair emission. Plotted over one 1.15GHz cycle, adjusted by the overall two-photon coincidences in the respective experiment, and subsequently normalised to the cumulative entangled-pair emission in DC. After one clock cycle, AR driving yields  $(21 \pm 3)\%$  more entangled pairs. Error bars and shaded ribbons indicate the respective estimated standard error based on Poissonian detection statistics and estimated setup drifts in polarization.

pair rate enhanced by  $(21 \pm 3)\%$  for 1.15 GHz AR driving compared to continuous driving in DC, of similar order to the 43% predicted for optimum driving conditions. The absolute detected entangled pair rate was  $(156 \pm 3)$  Hz for the DC equilibrium. For AR driving the entangled pair rate, after normalising to the same number of total two-photon coincidences as in DC, was  $(188 \pm 3)$  Hz. The detected entangled pair count rate scales with the square of the overall collection efficiency. Thus, an optimized collection efficiency would bring the detection rates closer to the near-GHz internal entangled pair generation rates of the QD system itself.

When matching the DC exciton intensity to AR at the employed driving intensities, the theoretically predicted relative AR advantage is 11 %, as shown in Fig. 5.19. In this metric as well we expect an enhanced efficiency for AR driving over DC for any non-zero pump rate. The relative efficiency  $\gamma_{\text{AR}}/\gamma_{\text{DC}}$  appears to scale almost linearly with the DC pump rate. We attribute the increased experimentally measured advantage of  $(21 \pm 3)\%$  to external dynamics affecting the system, such as higher charge noise in DC due to the continuous electrical current. Notably, spin scattering

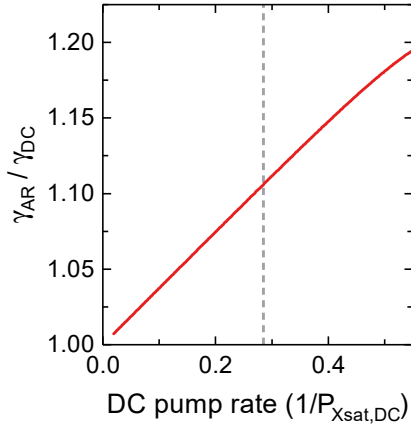


Figure 5.19: Modelled ratio of AR to DC entangled pair generation efficiency.  $\gamma$  is the respective entangled pair rate normalised by the total two-photon coincidences. In AR, the driving pump rate is matched such that the total  $X$  intensity equals that of the respective DC pump rate, as done in the experiment. The dashed vertical line marks the experimentally chosen pump rate.

due to interaction of the QD with the solid-state environment plays a role in practice [Tro14], potentially magnified by the increased charge noise. Thus the presented proof-of-principle experiment in the weak pumping regime is a reliable predictor for the expected performance advantage at optimum driving parameters for a QD sample suitable for high pumping rates.

## 5.5 Compatibility with optical biexciton initialisation

The discussed AR scheme and the associated benefits offer the chance for additional investigation. Notably, the scheme could be combined with optical pumping of the biexciton state instead of electrical pumping. In particular two-photon excitation has been shown to enable high-fidelity generation of entangled photons from quantum dots [Hub18a]. In the AR scheme, the only partially populated ground state hinders a full population transfer to the biexciton state purely via Rabi flopping. However, compatible alternatives are given by two-photon excitation via adiabatic rapid passage [Glä13b, Kal17b] and phonon-assisted two-photon excitation [Glä13a, Ard14, Bou15], both of which are in principle capable of transferring partial ground and exciton populations to the biexciton state.

## 5.6 Conclusion

The theoretical and experimental results of active reset driving presented in this chapter provide fundamental insight into the dynamics of a non-resonantly driven few-level quantum system. Most notably, we motivated how the system may generate entangled photon pairs at a superior emission rate when driven for only a fraction of the time, compared to driving the system in a continuous equilibrium. In an experimental implementation of AR driving in the weak pumping regime, we demonstrated an entangled pair rate enhanced by  $(21 \pm 3)\%$  compared to a continuously driven reference measurement. In addition, this experiment constituted the electrically driven entangled photon generation at a record 1.15 GHz clock rate while maintaining a  $(79.5 \pm 1.1)\%$  overall fidelity, compatible in principle with entanglement-based QKD.

The insights presented in this chapter present ample opportunity for further research. A natural progression of the experimental work is a demonstration of AR driving in the strong pumping regime, where we predict a strictly superior entangled pair rate compared to the optimum continuously driven entangled pair rate. As discussed, in addition to electrical driving this could be achieved via non-resonant optical or quasi-resonant optical excitation. Another area of interest is the effect of active reset driving on other quantum optical properties of the emission, namely on coherence and indistinguishability. In particular for electrical driving, a reduced charge noise outside of the initialisation pulse could potentially lead to superior results in both metrics while maintaining superior emission rates compared to low frequency, fully pulsed driving.

Furthermore, the considerations in this chapter place little restraints on the external entanglement source design. The approach is therefore compatible with a wide variety of other techniques to enhance the source brightness, such as micropillars [Dou10, Din16], broadband antennas [Che18], circular Bragg grating cavities [Liu19, Wan19], or photonic crystals [Arc14]. Notably, this driving scheme could benefit from Purcell-enhanced radiative decay rates some of these approaches provide, reducing the

radiative lifetime and shifting the optimum AR clock rate to even higher frequencies. The measurements in this chapter were performed on a sample with a FSS of  $10\mu\text{eV}$ , requiring reconstruction of the time-evolving entanglement fidelity. For QD samples with reduced FSS [Tro14], monitoring the static entanglement fidelity would be sufficient, simplifying both data analysis and integration in future photonic applications.

Finally, entangled-LEDs operated in the active reset regime may benefit the overall performance of entanglement-based photonic applications. The gigahertz-clocked generation of entangled photon pairs combined with the enhanced entanglement fidelity and source brightness compared to equilibrium operation is of particular interest for entanglement-based QKD protocols, quantum relays, and future implementations of a quantum repeater.

# 6 Entangled LEDs for measurement-device-independent QKD

This section describes theoretical results on the integration of E-LEDs in MDI-QKD. The theoretical model, methodology, computations and analysis were realised by Jonathan R. A. Müller with valuable insight from R. Mark Stevenson and Nathan Walk, and with guidance from Andrew J. Shields.

The integration of QD emitters in QKD schemes has been a topic of continuous interest over the years [Dzu15, Bas21, Sch21]. A major benefit of this approach is the prospect of multi-fold key rate improvements over the use of laser-generated WCPs due to sub-Poissonian photon statistics [Wan08, Cha20, Kup20].

A popular class of QKD schemes is formed by MDI-QKD, eliminating the susceptibility to detector side-channel attacks. In order to extend the maximum communication distance of traditional MDI-QKD, Xu et al. have proposed the addition of an entangled photon source to the scheme, acting as an additional untrusted relay [Xu13]. In the proposal, the authors focussed on the use of SPDC sources for the generation of entangled photons. As the authors point out, however, the inherent probability of multi-photon-pair emission from SPDC increases the QBER, thus limiting the achievable key rate in this scheme. This limitation could, in principle, be overcome by instead leveraging the sub-Poissonian photon statistics of an E-LED.

In this chapter we theoretically explore the integration of such an E-LED source in the MDI-QKD scheme. In the first half of the chapter, we present the envisioned QKD scheme and theoretical model. In the second half we present and analyse the numerically computed results for such an implementation.

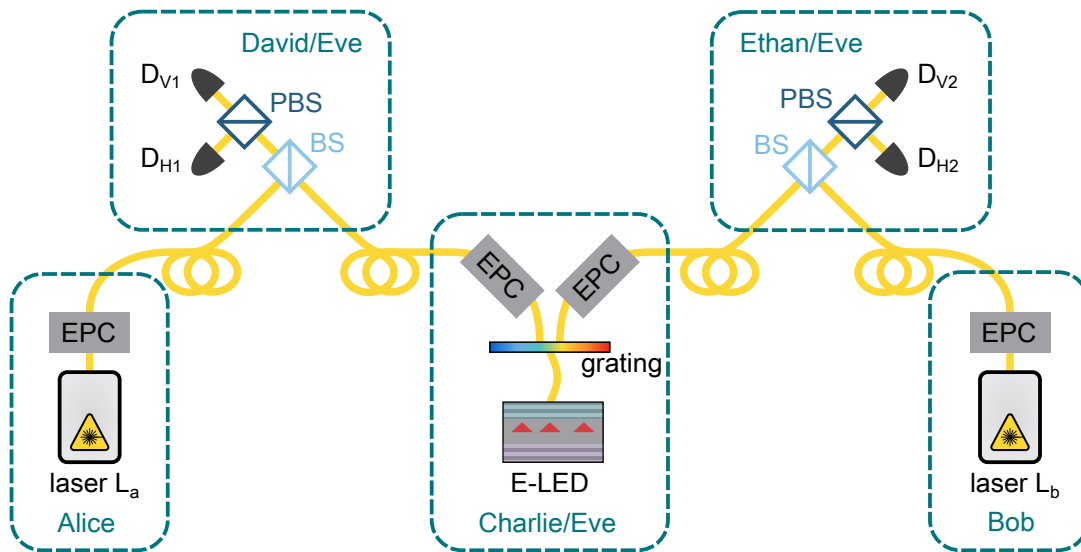


Figure 6.1: Measurement setup for entanglement-based MDI-QKD using an E-LED.

Alice and Bob send out a bit, encoded as a WCP in either the rectilinear or diagonal basis, following the BB84 protocol. At the same time, Charlie generates an entangled  $XX$ - $X$  pair. David then performs a BSM on Alice's photon and the  $XX$  photon; and separately Ethan performs a BSM on Bob's photon and the  $X$  photon. Successful measurement of both Bell states then indicates even parity of Alice's and Bob's bits, subject to QBER.

## 6.1 Entanglement-based MDI-QKD protocol

A simple experimental setup to realise this entanglement-based MDI-QKD (E-MDI-QKD) scheme is illustrated in Fig. 6.1, modified from the proposal by Xu et al. [Xu13]. The original MDI-QKD scheme (cf. Fig. 2.9) is extended by an untrusted entangled-pair node (Charlie) as well as a second untrusted BSM (Ethan). The E-MDI-QKD protocol is as follows:

1. Alice and Bob each send out one bit, polarisation-encoded as a WCP in either the rectilinear or diagonal basis (chosen randomly)
2. At the same time Charlie generates an entangled  $XX$ - $X$  pair, sending one photon each to David and Ethan.

3. BSMs are then performed on Alice’s photon and the  $XX$  photon; and separately on Bob’s photon and the  $X$  photon.
4. David and Ethan broadcast successful BSMs using classical channels
5. Alice and Bob use classical communication to post-select events where they used the same polarisation basis and where David and Ethan performed successful BSMs. For these events they now share a secret bit-string (subject to QBER and privacy amplification), even in the case where Charlie, David, and Ethan are all controlled by an untrusted adversary Eve. The untrusted parties only know that Alice and Bob’s bits have even parity, but not whether a given bit is a 1 or 0.

Compared to the implementation by Xu et al. [Xu13], we have replaced the SPDC source by an E-LED. For simplicity, instead of allowing for measurement of both,  $|\psi^+\rangle$  and  $|\psi^-\rangle$  at the David and Ethan nodes, we exclusively consider projection onto the  $|\psi^+\rangle$  state. Although this reduces the key-rate by a factor of 4, this simplification does not affect the overall communication distance, nor the success rate or security of the protocol. The results can then be trivially extended back to the case where both,  $|\psi^+\rangle$  and  $|\psi^-\rangle$  are measured.

Table 6.1 summarises the resulting bit parity: whenever a successful  $|\psi^+\psi^+\rangle$  measurement is announced, Alice and Bob expect to share the same bit. Notably the parity

	$ \psi^+\psi^+\rangle$ Bell state
Rectilinear basis	Even bit parity
Diagonal basis	Even bit parity

Table 6.1: Parity table according to chosen polarisation bases and measured Bell state for zero FSS. Alice and Bob post-select the bits where they chose the same polarisation basis (rectilinear or diagonal) and successful BSMs onto  $|\psi^+\psi^+\rangle$  are announced. As a result, their bits share the same parity. The bit-parity is derived in appendix A.1.

table differs from that of Xu et al. [Xu13] as SPDCs emit into the  $\frac{1}{\sqrt{2}}(|HV\rangle + |VH\rangle)$  state, requiring additional subsequent bit flips.

## 6.2 Theoretical model

For the theoretical evaluation of the protocol, we extend the approach presented in Ref. [Var16] for quantum teleportation using E-LEDs, which represents a subset of the experimental E-MDI-QKD scheme. Compared to quantum teleportation, for E-MDI we require a second sender (Bob) and a second BSM (Ethan). In a way, E-MDI-QKD can be seen as Alice first performing quantum teleportation of her qubit via David and Charlie as a relay, and subsequently performing standard MDI-QKD by interfering Alice's teleported qubit and Bob's qubit at Ethan.

We begin with the general wavefunctions of the QD and laser photons. These take the general form

$$|\psi_j\rangle = A_j(t_j)C_j(t_j)|\Psi_j(t_j)\rangle, \quad (6.1)$$

consisting of the time-dependent real amplitude  $A_j(t_j)$ , overall phase  $C_j(t_j)$ , and polarisation  $|\Psi_j(t_j)\rangle$ . The overall phase in turn is given by

$$C_j(t_j) = e^{i\omega_j t_j} e^{i\phi_j(t_j)} \quad (6.2)$$

where  $\omega_j$  represents the angular optical frequency and  $\phi_j(t)$  denotes phase fluctuations as a function of time  $\Delta$ , such that

$$\langle e^{i[\phi_j(t_j) - \phi_j(t_j + \Delta)]} \rangle = e^{-|\Delta|/\tau_{\text{coh},j}} \quad (6.3)$$

for a given coherence time  $\tau_{\text{coh},j}$  [Leg03, Var16].

For laser  $L_a$  we yield:

$$|\psi_{L_a}\rangle = A_{L_a}(t_{L_a})C_{L_a}(t_{L_a})|\Psi_{L_a}\rangle, \quad (6.4)$$

$$|\Psi_{L_a}\rangle = \cos(\theta_{L_a})|H\rangle + e^{i\varphi_{L_a}}\sin(\theta_{L_a})|V\rangle, \quad (6.5)$$

and analogously for laser  $L_b$ .

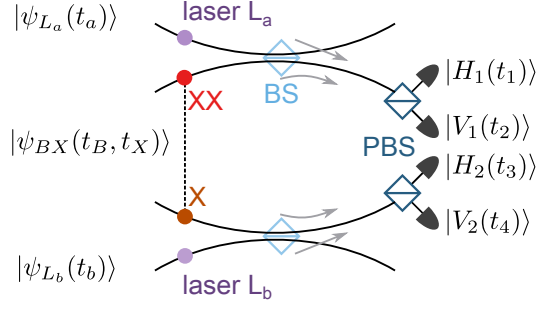


Figure 6.2: Schematic of entanglement-based MDI-QKD. Biexciton and laser A interfere on a non-polarising beam splitter; analogously exciton and laser B. Polarising beam splitters then project the photons onto the detector polarisation states  $|H_1\rangle$ ,  $|V_1\rangle$ ,  $|H_2\rangle$  and  $|V_2\rangle$ .

The E-LED emission is given by

$$|\psi_{BX}\rangle = A_{BX}(t_B, t_X) C_B(t_B) C_X(t_X) |\Psi_{BX}(t_B, t_X)\rangle. \quad (6.6)$$

The polarisation state  $|\Psi_{BX}(t_B, t_X)\rangle$  is approximated as an entangled contribution  $|\Psi_{BX,ent}\rangle$  plus a maximally mixed contribution  $|\Psi_{BX,mixed}\rangle$ . Note in this chapter, we denote biexciton contributions via the index  $B$  instead of  $XX$  to enhance legibility. The entangled contribution is given by

$$|\Psi_{BX,ent}\rangle = \frac{1}{\sqrt{2}} \left( e^{iS(t_X-t_B)} |HH\rangle + e^{-iS(t_X-t_B)} |VV\rangle \right), \quad (6.7)$$

where  $S$  is the FSS. The non-entangled contribution is given by the maximally mixed state (cf. Eq. (5.5)).

### 6.2.1 Four-photon measurement

As illustrated in Fig. 6.2, we project the four photons onto the detector polarisation states given by  $|H_1\rangle$ ,  $|V_1\rangle$  for Charlie and  $|H_2\rangle$ ,  $|V_2\rangle$  for Ethan. At each of the four detectors, the detection event may originate from either a laser or a (bi-)exciton photon. This leads to  $2^4 = 16$  total possible combinations of detected photon events.

The joint electric field amplitude of successful events is then described by the four terms

$$\begin{aligned}
 Z = & \langle H_1 | \psi_{L_a} \rangle \langle V_1 V_2 | \psi_{BX} \rangle \langle H_2 | \psi_{L_b} \rangle \\
 & + \langle V_1 | \psi_{L_a} \rangle \langle H_1 H_2 | \psi_{BX} \rangle \langle V_2 | \psi_{L_b} \rangle \\
 & + \langle H_1 | \psi_{L_a} \rangle \langle V_1 H_2 | \psi_{BX} \rangle \langle V_2 | \psi_{L_b} \rangle \\
 & + \langle V_1 | \psi_{L_a} \rangle \langle H_1 V_2 | \psi_{BX} \rangle \langle H_2 | \psi_{L_b} \rangle
 \end{aligned} \tag{6.8}$$

where each term describes a different permutation of the laser  $L_a$ ,  $XX$ ,  $X$ , and laser  $L_b$  triggering the detectors.

The remaining 12 terms then describe the cases of detectors triggering from unintended multi-photon contributions, e.g. two photons from laser  $L_a$  triggering both  $|H_1\rangle$  and  $|V_1\rangle$ , likewise for QD multi-photon events:

$$\begin{aligned}
 \tilde{Z} = & \left. \begin{aligned} & \langle H_1 V_1 | \psi_{L_a L_a} \rangle \langle H_2 | \psi_X \rangle \langle V_2 | \psi_{L_b} \rangle \\ & + \langle H_1 V_1 | \psi_{L_a L_a} \rangle \langle V_2 | \psi_X \rangle \langle H_2 | \psi_{L_b} \rangle \end{aligned} \right\} 2 \times \text{laser } L_a \\
 & \left. \begin{aligned} & + \langle H_1 | \psi_{L_a} \rangle \langle V_1 | \psi_B \rangle \langle H_2 V_2 | \psi_{L_b L_b} \rangle \\ & + \langle V_1 | \psi_{L_a} \rangle \langle H_1 | \psi_B \rangle \langle H_2 V_2 | \psi_{L_b L_b} \rangle \end{aligned} \right\} 2 \times \text{laser } L_b \\
 & \left. \begin{aligned} & + \langle H_1 V_1 H_2 | \psi_{BBX} \rangle \langle V_2 | \psi_{L_b} \rangle \\ & + \langle H_1 V_1 V_2 | \psi_{BBX} \rangle \langle H_2 | \psi_{L_b} \rangle \end{aligned} \right\} 2 \times \text{biexciton} \\
 & \left. \begin{aligned} & + \langle H_1 | \psi_{L_a} \rangle \langle V_1 H_2 V_2 | \psi_{BXX} \rangle \\ & + \langle V_1 | \psi_{L_a} \rangle \langle H_1 H_2 V_2 | \psi_{BXX} \rangle \end{aligned} \right\} 2 \times \text{exciton} \\
 & \left. \begin{aligned} & + \langle H_1 V_1 | \psi_{L_a L_a} \rangle \langle H_2 V_2 | \psi_{XX} \rangle \end{aligned} \right\} 2 \times \text{laser } L_a \text{ and } 2 \times \text{exciton} \\
 & \left. \begin{aligned} & + \langle H_1 V_1 | \psi_{BB} \rangle \langle H_2 V_2 | \psi_{L_b L_b} \rangle \end{aligned} \right\} 2 \times \text{biexciton and } 2 \times \text{laser } L_b \\
 & \left. \begin{aligned} & + \langle H_1 V_1 | \psi_{L_a L_a} \rangle \langle H_2 V_2 | \psi_{L_b L_b} \rangle \end{aligned} \right\} 2 \times \text{laser } L_a \text{ and } 2 \times \text{laser } L_b \\
 & \left. \begin{aligned} & + \langle H_1 V_1 H_2 V_2 | \psi_{BBXX} \rangle . \end{aligned} \right\} 2 \times \text{biexciton and } 2 \times \text{exciton}
 \end{aligned} \tag{6.9}$$

In addition, multiple photons could impinge on the same detector. However, these would form part of a different set of four-photon coincidences. Moreover, detection system dead times ( $\sim 80$  ns for the system used in the previous chapter) would typically prevent detection of photons in quick succession.

We can now compute the total four-photon intensity, given by  $(Z + \tilde{Z})(Z^* + \tilde{Z}^*)$ , by inserting Eqs. (6.4) – (6.7) into Eq. (6.9). In addition we make the substitutions

$$A_j^2(t_j) = n_j I_j(t_j), \quad (6.10)$$

$$A_{jk}^2(t_j, t_k) = n_j n_k g_{jk}^{(2)}(t_j, t_k), \quad (6.11)$$

where  $n_j$  is the time-averaged intensity of photon  $j$  and  $I_j(t_j)$  the normalised, time-dependent intensity.  $g_{jk}^{(2)}$  describes the time-dependent second-order correlation. To avoid confusion and without loss of generality, we assume the path length for all photons to be equally long, such that the detection delay between any two given photons equals the emission delay.

Employing symbolic computation software [Wol20], we finally compute the (normalised) total fourth-order correlation measured at the detectors to be:

$$\begin{aligned} g^{(4)}(t_1, t_2, t_3, t_4) = & \frac{1}{2} \sin^2(\theta_{L_a}) \sin^2(\theta_{L_b}) I_{L_a}(t_2) I_{L_b}(t_4) g_{BX,ent}^{(2)}(t_1, t_3) \\ & + \frac{1}{2} \cos^2(\theta_{L_a}) \cos^2(\theta_{L_b}) I_{L_a}(t_1) I_{L_b}(t_3) g_{BX,ent}^{(2)}(t_2, t_4) \\ & + \frac{1}{4} \left\{ \exp \left( -\frac{|t_2 - t_1|}{\tau_{L_a}} - \frac{|t_2 - t_1|}{\tau_{\text{coh},B}} - \frac{|t_4 - t_3|}{\tau_X} - \frac{|t_4 - t_3|}{\tau_{L_b}} \right) \right. \\ & \times \sqrt{I_{L_a}(t_1) I_{L_a}(t_2) I_{L_b}(t_3) I_{L_b}(t_4) g_{BX,ent}^{(2)}(t_1, t_3) g_{BX,ent}^{(2)}(t_2, t_4)} \\ & \times \sin(2\theta_{L_a}) \sin(2\theta_{L_b}) \cos \left[ \varphi_{L_a} + \varphi_{L_b} + \frac{1}{2} S(t_4 + t_3 - t_2 - t_1) \right. \\ & \left. \left. + (\omega_{L_a} - \omega_B)(t_2 - t_1) + (\omega_{L_b} - \omega_X)(t_4 - t_3) \right] \right\} \\ & + \tilde{g}^{(4)}(t_1, t_2, t_3, t_4). \end{aligned} \quad (6.12)$$

The first (second) term describes successful four-photon events when Alice and Bob both emit into the V (H) state. The third term describes successful four-photon events when Alice and Bob emit in the diagonal basis, requiring two-photon interference on the two non-polarising beam splitters. The biexciton and exciton intensity

are represented via the time-resolved second-order correlation  $g_{jk}^{(2)}(t_j, t_k)$  and remain inseparable, a fact that has been shown to inherently limit the indistinguishability of either emission [Sim05, Sch20]. Finally,  $\tilde{g}^{(4)}(t_1, t_2, t_3, t_4)$  are unintentional coincidences from multi-photon events and mixed E-LED emission, expanded in appendix A.2.

### 6.3 Numerical simulations

In order to model the time-dependent  $XX$  and  $X$  intensities, as well as the associated second- and higher-order correlations of the E-LED emission, we again employ the rate equation model described in Ch. 5. The resulting  $XX$  and  $X$  intensity is shown in Fig. 6.3. Here we have assumed a strong, 50 ps rectangular driving pulse at time zero, initialising the QD to the  $XX$  state. In addition we use the same QD lifetimes as in the previous chapter,  $\tau_B = 300$  ps and  $\tau_X = 500$  ps. For now we set the clock rate to be much slower than the radiative decay rates, such that the QD fully relaxes to the ground state before reexcitation. Furthermore we assume a typical coherence time of  $\tau_{\text{coh},B} = \tau_{\text{coh},X} = 150$  ps for both,  $X$  and  $XX$  [Var16].

An important factor is the choice of laser temporal pulse shape. We limit ourselves to Gaussian temporal pulse shapes, thus leaving only the FWHM and emission time as free parameters. In order to ensure a favourable temporal overlap of laser and E-LED emission, we match the temporal FWHM of laser  $L_a$  to that of the  $XX$  emission, and analogously for laser  $L_b$  and  $X$ . We then set the laser emission delay to the time where the convolution of laser and respective E-LED emission is maximal (also shown in Fig. 6.3). In addition, we tune the laser optical frequency into resonance with the respective QD emission, i.e.  $\omega_{L_a} = \omega_B$  and  $\omega_{L_b} = \omega_X$ . Inspection of Eq. (6.12) reveals that in this model the absolute optical frequency does not affect results; only the respective relative detunings do. Finally, for simplicity we focus on the case of zero fine-structure splitting  $S = 0$  and apply a typical 50 ps Gaussian detection jitter. Nevertheless, the results in this chapter can be extended directly to samples with

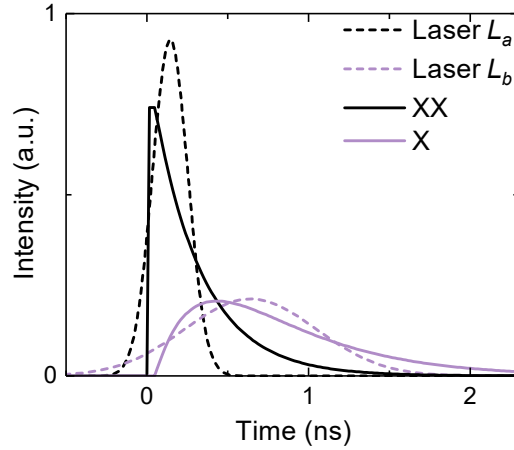


Figure 6.3: Time-resolved intensities of the four sources contributing to the MDI-QKD scheme. The mean intensity and FWHM of laser  $L_a$  is chosen to match that of the  $XX$  emission; analogously for laser  $L_b$  and  $X$ . The temporal delay of the lasers is determined by maximising the overlap with the respective  $XX$  and  $X$  emission.

non-zero FSS by taking into account the time-evolution of the  $XX$ - $X$  pair during correlation measurements (cf. Chs. 2.3.1 and 5.4).

Fig. 6.4 shows the modelled fourth-order correlation  $g^{(4)}$  (i.e. normalised, time-dependent probability of measuring the  $|\psi^+\psi^+\rangle$  state) for different polarisation encodings. To visualise the four-dimensional data (computed as a function of  $(t_1, t_2, t_3, t_4)$ ), we plot the fourth-order correlation as a function of the time delay  $\tau_{13} = t_3 - t_1$  between the  $|H_1\rangle$  and  $|H_2\rangle$  detector clicks, as well as the delay  $\tau_{24} = t_4 - t_2$  between the  $|V_1\rangle$  and  $|V_2\rangle$  detector clicks. In addition we integrate over the absolute time-delays  $t_1$  and  $t_2$ , so the plot as shown is computed via the function  $\iint g^{(4)}(t_1, t_2, t_1 + \tau_{13}, t_2 + \tau_{24}) dt_1 dt_2$ .

Panel 6.4a shows  $g^{(4)}$  for the case where Alice and Bob each send an  $|H\rangle$  encoded WCP. The x-axis plots the time-delay  $\tau_{13} = t_3 - t_1$  between the  $|H_1\rangle$  and  $|H_2\rangle$  detector clicks. Consequently, in panel 6.4a the correlation in  $\tau_{13}$ -direction predominantly shows the detection of laser  $L_b$  after  $L_a$ . Likewise, the y-axis plots the time-delay  $\tau_{24} = t_4 - t_2$  between the  $|V_1\rangle$  and  $|V_2\rangle$  detector clicks. In panel 6.4a this dominantly

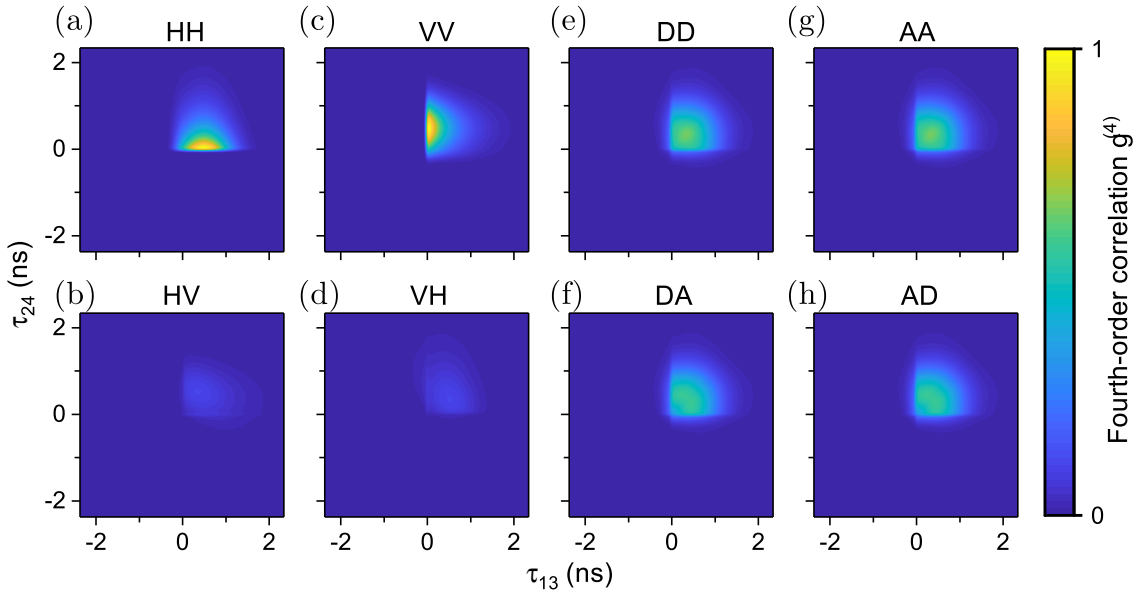


Figure 6.4: Fourth-order correlation  $g^{(4)}(\tau_{13}, \tau_{24})$  as a function of time delay  $\tau_{13} = t_3 - t_1$  between detection of  $|H_1\rangle$  and  $|H_2\rangle$ ) as well as  $\tau_{24} = t_4 - t_2$  ( $|V_1\rangle$  and  $|V_2\rangle$ ). The panels show the resulting  $g^{(4)}(\tau_{13}, \tau_{24})$  for the respective polarisation encodings of Alice's and Bob's laser. The data are computed and plotted in bins of  $32 \text{ ps} \times 32 \text{ ps}$ .

corresponds to detection of the  $X$  photon after the  $XX$  photon. Hence in this case the  $g^{(4)}$  is strongly biased towards  $t_{24} \geq 0$ .

Panel 6.4b shows the case where laser  $L_a$  is emitted in  $|H\rangle$  and laser  $L_b$  in  $|V\rangle$ . Ideally, in this case where Alice and Bob's bit have opposite parity, the QKD protocol predicts no measurement of the  $|\psi^+\psi^+\rangle$  at all. However as discussed above, unintentional multi-photon events as well as mixed E-LED emission still produce a small amount of four-photon coincidences.

In panel 6.4c the polarisation encodings of are flipped from H to V for both lasers. Hence, the resulting correlation is mirrored along the diagonal compared to panel 6.4a.

In panels 6.4e–h Alice and Bob both emit in the diagonal polarisation basis. As a consequence, the resulting  $g^{(4)}$  is diagonally symmetric when projected onto the rectilinear polarisation basis of the detectors. The difference between panels 6.4e and

6.4f relies on quantum interference on both of the two non-polarising BS, manifesting as a subtle increase in  $g^{(4)}$  along the diagonal, near the origin for positive  $\tau_{13}$ , and  $\tau_{24}$ . Before we further evaluate the correlations in the diagonal basis, in the following section we first introduce further tools for the evaluation of successful MDI-QKD.

### 6.3.1 Fidelity to the ideal E-MDI-QKD protocol

We define the E-MDI-QKD fidelity for the case of Alice emitting into  $|H\rangle$  as

$$F_{\text{MDI},H} = \frac{g_{HH}^{(4)}}{g_{HH}^{(4)} + g_{HV}^{(4)}}, \quad (6.13)$$

and analogously for  $F_{\text{MDI},V}$ ,  $F_{\text{MDI},D}$ , and  $F_{\text{MDI},A}$ . From Alice's point of view—given basis reconciliation and successful four-photon measurement—this corresponds to the probability that Bob indeed emitted into the same polarisation state as Alice.

Assuming uniformly random polarisation encoding choices, the mean fidelity over all measurements (after basis reconciliation) is then given by

$$F_{\text{MDI}} = \frac{1}{4}(F_{\text{MDI},H} + F_{\text{MDI},V} + F_{\text{MDI},D} + F_{\text{MDI},A}). \quad (6.14)$$

In turn, the overall QBER is given by  $(1 - F_{\text{MDI}})$ . For a four-state BB84 protocol such as the one investigated here, error-correction schemes are available for a QBER up to 20% [Cha02], corresponding to  $F_{\text{MDI}} \geq 0.8$ . The classical limit on the fidelity is given by  $F_{\text{MDI}} \leq 0.75$  [Var16]. Fully uncorrelated input bits produce  $F_{\text{MDI}} = 0.5$ , while anti-correlated inputs produce  $F_{\text{MDI}} \leq 0.5$ .

Fig. 6.5 shows the calculated fidelity  $F_{\text{MDI}}$  for different polarisation input encodings of Alice as defined in Eq. (6.13). Again,  $F_{\text{MDI},V}$  (panel 6.5b) corresponds to  $F_{\text{MDI},H}$  (panel 6.5a) mirrored along the diagonal axis. Although one might expect a minimum theoretical fidelity of  $F_{\text{MDI},H}, F_{\text{MDI},V} \geq 0.5$  (i.e. uncorrelated input bits) in the case of unsuccessful E-MDI-QKD, the figure reveals anti-correlated regions with  $F_{\text{MDI}}$  close to 0. An intuitive explanation of this phenomenon is provided in appendix A.3. Nevertheless, comparison with Fig. 6.4a and 6.4b shows that the fourth-order correlation is strongly concentrated towards regions where  $F \geq 0.5$ . Thus for the overall fidelity, these regions of anti-correlated input bits play only a minor role.

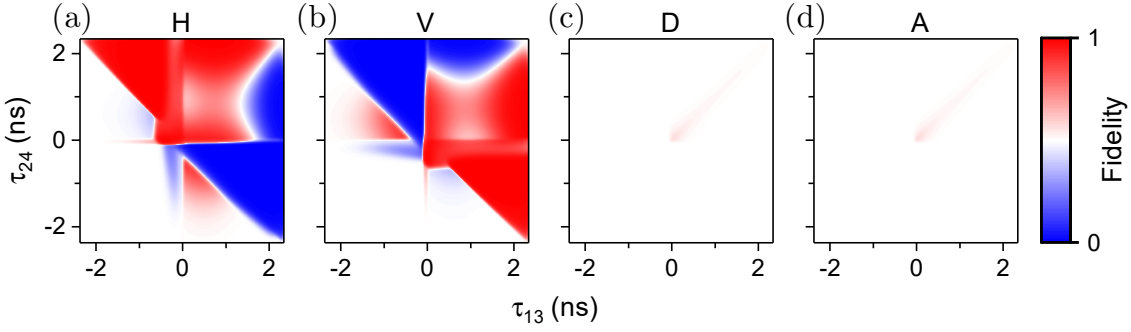


Figure 6.5: Fidelity  $F_{\text{MDI}}(\tau_{13}, \tau_{24})$  for different polarisation input encodings of Alice.

Input states in the rectangular basis (panels a and b) produce significant regions of high fidelity. Input polarisations in the diagonal basis (panels c and d) yield high fidelity only along the diagonal.

The fidelity when Alice and Bob both emit in the diagonal input basis (panels 6.5c and 6.5d) is symmetric along the diagonal. Clearly, the correlation for diagonal input bases is much more limited compared to that for rectangular input bases. As mentioned above, this is due to the reliance on two-photon interference between laser and exciton emission. As derived in Eq. (6.12), this effect scales with  $\exp(-|t_2 - t_1|/\tau_{\text{coh},B} - |t_4 - t_3|/\tau_{\text{coh},X})$ . In Figs. 6.5c and 6.5d this two-photon interference manifests as an increased fidelity along the diagonal. The model produces a maximum fidelity for  $H$  and  $V$  input polarisations (panels 6.5a and 6.5b) of 99.98 %, while the  $D$  and  $A$  input polarisations only yield a maximum of 56.83 %.

Fig. 6.6a shows the mean fourth-order-correlation  $g^{(4)}$  over all polarisation input configurations. As the figure reveals, the overall  $g^{(4)}$  is clearly biased towards the top-right quadrant where  $\tau_{13}, \tau_{24} \geq 0$ . As discussed before, this stems from the emission delay of the  $X$  photon after the  $XX$  photon. The corresponding mean fidelity  $F_{\text{MDI}}$  is shown in panel 6.6b. For positive time-delays  $\tau_{13}, \tau_{24} \geq 0$ , the fidelity  $F_{\text{MDI}}$  remains above the uncorrelated value of 0.5, approaching it asymptotically for longer time delays. The maximum fidelity as shown in the panel reaches 75.6 %, just above the classical limit of 75 %.

For a closer look at the fidelity, Fig. 6.7a shows  $F_{\text{MDI}}$  as a function of  $\tau_{13}$  while pinning  $\tau_{24} = \tau_{13}$ . The purple line corresponds exactly to a cross-section of Fig. 6.6b,

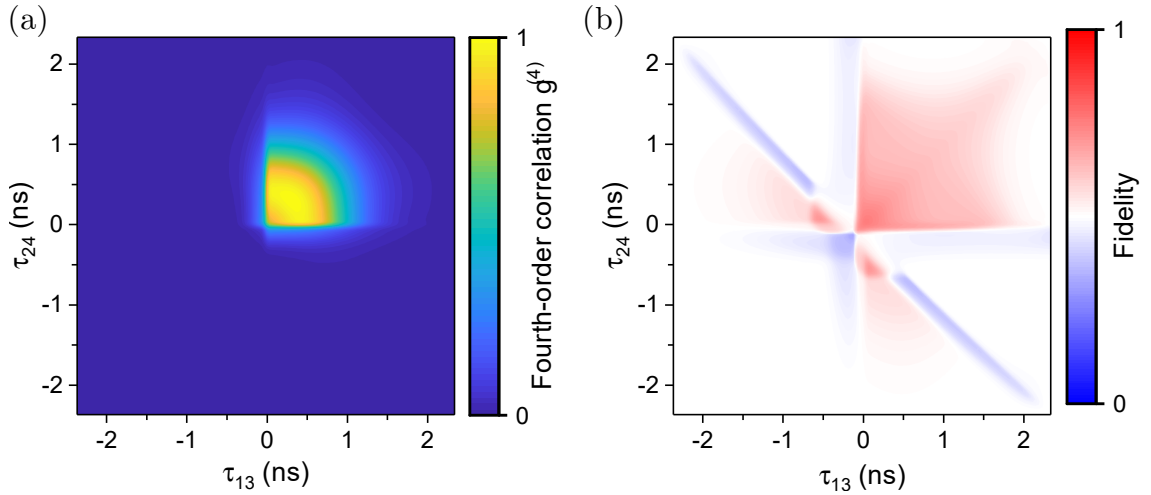


Figure 6.6: (a) Mean fourth-order correlation  $g^{(4)}(\tau_{13}, \tau_{24})$  and (b) mean fidelity  $F_{\text{MDI}}(\tau_{13}, \tau_{24})$  over all input polarisation configurations. Although the fidelity is high in some regions where either  $\tau_{13} < 0$  or  $\tau_{24} < 0$ , the fourth-order correlation is dominantly confined to the region of  $\tau_{13}, \tau_{24} > 0$ .

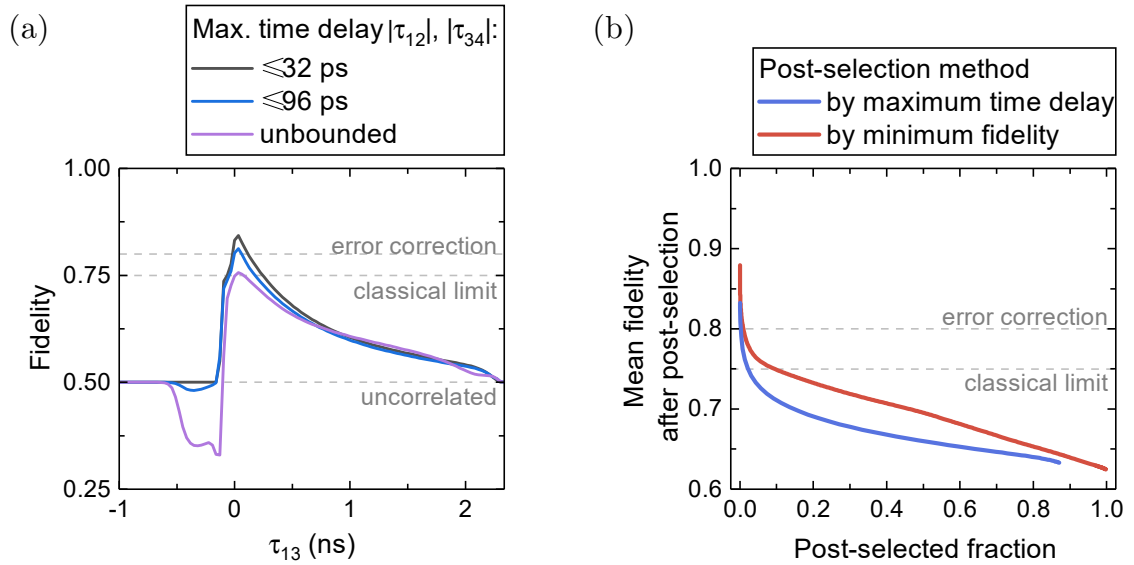


Figure 6.7: (a) Mean fidelity  $F_{\text{MDI}}$  as a function of time delay  $\tau_{13}$  (and pinning  $\tau_{24} = \tau_{13}$ ). The four-photon coincidences are post-selected via the maximum absolute time delays for both,  $\tau_{12}$  (detection delay between detectors  $D_{H1}$  and  $D_{V1}$ ) and  $\tau_{34}$  (between detectors  $D_{H2}$  and  $D_{V2}$ ). (b) Mean fidelity  $F_{\text{MDI}}$  after post-selection of coincidences via different criteria, shown as a function of post-selected fraction of coincidences.

along the diagonal where  $\tau_{24} = \tau_{13}$ . The classical limit is exceeded only briefly, at a time-delay of  $\tau_{13} \approx 32$  ps. At  $\tau_{13} < 0$  the fidelity dips below the uncorrelated value of 0.5 (cf. appendix A.3)—however, the probability of measuring a four-photon coincidence at  $\tau_{13} < 0$  is negligible (cf. Fig. 6.6).

So far we have only considered  $F_{\text{MDI}}$  as a function of  $\tau_{13}$  and  $\tau_{24}$ . The two-photon interference contribution, however, decays exponentially with the absolute time delays  $|\tau_{12}| = |t_2 - t_1|$  and  $|\tau_{34}| = |t_4 - t_3|$  between the two photons interfering on either of the beam splitters (as described in Eq. 6.12). Thus, in Fig. 6.7a we also show the fidelity when setting a limit of  $|\tau_{12}|, |\tau_{34}| \leq 96$  ps and  $\leq 32$  ps respectively. Notably, a limit of 160 ps is sufficient to reach a maximum fidelity of 81.3%, exceeding the minimum fidelity of 80% required for error correction. Further limiting the absolute delay to 32 ps yields a maximum fidelity of 84.3%.

Fig. 6.7b shows the overall mean fidelity when applying different post-selection rules. For the blue line, we set a maximum permissible time delay  $\tau_{\text{max}}$  and select those coincidences where  $0 \leq \tau_{13}, \tau_{24} \leq \tau_{\text{max}}$  and  $0 \leq |\tau_{12}|, |\tau_{34}| \leq \tau_{\text{max}}$ . For  $\tau_{13}$  and  $\tau_{24}$ , we limit the minimum time delay to 0, as we want to ensure we select coincidences where the exciton is detected after the biexciton. For  $\tau_{12}$  and  $\tau_{34}$  we only limit the absolute value of the time delay. When we set  $\tau_{\text{max}} = 32$  ps, the mean fidelity reads 83.2%, with a post-selected fraction of coincidences of 0.0031%. For a longer  $\tau_{\text{max}}$  of 96 ps, we are left with a significantly larger fraction of 0.15%, while the mean fidelity becomes 80.9%, still above the limit for error correction.

For the red line we apply a more complex post-selection method: We set a minimum fidelity, and reject all (four-dimensional  $(32 \text{ ps})^4$ ) time-bins where the corresponding fidelity is lower. To increase the post-selected fraction, the minimum fidelity is then successively lowered. As this method of post-selection is more refined than post-selecting by time-delay, the resulting mean fidelity is always higher for a given post-selected fraction. However, this method requires near-perfect knowledge of the experimental system and is perhaps of limited usefulness in a practical experiment. Nevertheless, selecting those time bins where the expected fidelity satisfies  $F_{\text{MDI}}(t_1, t_2, t_3, t_4) \geq 80\%$  we yield a mean fidelity of 81.9% and remain

with a fraction of 0.36 % of all measured four-photon coincidences. This fraction of high-fidelity coincidences depends strongly on the  $XX$  and  $X$  coherence time. For a QD with twice the coherence time, i.e.  $\tau_{\text{coh},B} = \tau_{\text{coh},X} = 300$  ps, the fraction of post-selected coincidences nearly triples to 1.04 % when using the same fidelity threshold of 80 %.

Overall we conclude that—although challenging—a practical demonstration of QKD is feasible using the proposed E-MDI-QKD scheme and a realistic E-LED source of entangled photons when employing appropriate temporal post-selection. However, to realise advantages over SPDC sources of entangled photons, improvements to the two-photon interference visibility are likely required, e.g. via enhanced coherence times. Finally, another possibility to improve the two-photon interference visibility is to increase the wave function overlap between the two photons. This could be achieved by replacing Alice’s and Bob’s laser with QD-like single-photon sources [Ben09] and stimulated photon emission [Sbr22].

## 6.4 Conclusion

In this chapter we proposed and theoretically explored the integration of an E-LED in an E-MDI-QKD scheme. The theoretical framework provides important insight into the mechanisms leading to successful four-photon correlations. Using realistic experimental parameters, we predict a fidelity of up to 84.3 % for a four-state protocol, exceeding the limit required for error-correction and, thus, enabling secure QKD using this scheme. In addition, we have identified the QD coherence time in particular as a key parameter, governing the fraction of successful E-MDI-QKD clock cycles.

The results from this chapter enable a range of future research endeavours. Further theoretical considerations involve estimations of practical key rates as a function of communication distance. Since both entanglement and optical intensity reduce towards the end of the radiative cascade, the presented scheme may feasibly benefit from a fast-clocked active reset of the radiative cascade (as presented in Ch. 5) to enhance the fraction of error-correctable four-photon coincidences. In practice, this

scheme also benefits from QD structures optimised for high collection efficiencies, such as circular Bragg grating cavities [Liu19, Wan19]. Furthermore, while E-LEDs already enable access to higher communication rates due to elimination of multi-photon-pair emission of SPDCs [Xu13], the use of WCPs for Alice's and Bob's input photon states still requires inefficient decoy states to ensure security [Hwa03]. Replacing the lasers by efficient SPS as well could, thus, lead to further multi-fold improvements of the key rate in addition to enhanced interference visibilities.

Another variation of MDI-QKD is given by twin-field QKD [Luc18], which currently offers the longest QKD communication distances for real-world implementations [Pit21, Wan22]. In analogy to E-MDI-QKD, Li et al. [Li21] have recently proposed the extension of twin-field QKD by an entangled-photon emitter node. As a result, the authors predicted the feasibility of QKD distances up to nearly 1000 km. Consequently, the work of this chapter could be extended to investigate the use of QD-like sub-Poissonian emitters in this extended twin-field QKD scheme.

Finally, the theoretical insight presented in this chapter paves the way for experimental demonstrations of E-MDI-QKD based on E-LEDs, ultimately forming a potential building block for a future long-distance quantum network.

# 7 | Summary and outlook

Quantum-light-emitting diodes make for a promising source of single and entangled photons for applications in quantum communication. An important aspect for the operation of such devices is the temporal driving technique. Consequently, the work presented in this thesis focussed on the realisation and employment of ultra-high-bandwidth QD LED devices. By theoretically and experimentally investigating different temporal driving schemes and the resulting impact on the generated quantum light, we obtained several key results:

In chapter 4 we demonstrated the design and fabrication of a QD LED capable of clock-rates up to 3.05 GHz, expanding on the findings of Bennett et al. [Ben05] and Hargart et al. [Har13]. We presented a low capacitance QD LED mesa design in order to enable high-frequency electrical operation. Via fast control of the charge carrier tunnelling rate, we were able to modulate the optical emission by nearly three orders of magnitude between clock cycles. The single-photon character of the optical emission was confirmed with a  $g^{(2)} = 0.268 \pm 0.002$ . To our knowledge, this constitutes the fastest-clocked demonstration of a single photon source [Buc12, Har13]. The limited optical recombination rate in the presented device could be enhanced by integrating the device into optical cavities with high Purcell enhancement [Dou10, Din16, Liu18], such as the recently popularised circular Bragg grating designs [Liu19, Wan19]. The achieved fast electrical control of the charge carrier population has the potential to allow further experimental insight into the underlying dynamics and enables device driving schemes such as the active reset presented in the subsequent chapter.

In chapter 5 we investigated the radiative cascade dynamics of atom-like quantum systems, such as QD LEDs. Via a theoretical rate-equation model, we identified an important result: By reinitialising the quantum system early, while the radiative cascade is still in progress, it is possible to produce entangled photon pairs at a

higher rate—compared to either continuous operation or conventional slow-pulsed operation. In addition, we expect a superior entanglement fidelity when driven in this active reset mode. We subsequently demonstrated this approach experimentally, finding an enhancement of  $(21 \pm 3)\%$  in the entangled-pair rate compared to continuous operation. For active-reset operation, entangled photons were electrically generated at a—to our knowledge—record 1.15 GHz clock rate while maintaining a  $(79.5 \pm 1.1)\%$  entanglement fidelity. When driven continuously, the device yielded an entanglement fidelity of  $(71.2 \pm 1.0)\%$ , lower than the fidelity in active reset.

We expect this result to be transferable to optical initialisation [Glä13a, Glä13b] and also to other entangled-photon sources based on radiative cascades, such as single atoms [Asp81]. This result may benefit the overall performance of entanglement-based photonic applications in the future. Although the optimum driving frequency will depend on the exact application, an active reset of the radiative cascade may raise the entangled photon pair rate in a quantum photonic communication link and thus increase the overall capacity of a quantum communication channel.

Finally, in chapter 6, we proposed and theoretically explored the integration of a QD LED in entanglement-based MDI-QKD [Xu13], potentially enabling enhanced key rates via sub-Poissonian photon statistics. The theoretical framework enables insight into the underlying dynamics required for successful quantum communication using this scheme. For realistic experimental parameters, we predict a fidelity of up to 84.3% for a four-state protocol, exceeding the limit required for error-correction and thus enabling secure QKD. The fraction of error-correctable four-photon events strongly increases with enhanced coherence time of the QD emitter. This work could be extended in the future by applying an active reset to the QD radiative cascade, and by investigating the resulting key rate for a given quantum channel. Furthermore, QD LEDs could also be used to replace the lasers of Alice and Bob, eliminating the need for decoy states in this scheme [Hwa03]. Finally, such an integration of sub-Poissonian photon sources could be extended to other MDI-QKD protocols, such as the recently popularised long-distance twin-field QKD protocol [Luc18, Li21] to potentially further enhance the quantum communication distance.

# Appendix

## A.1 Bit parity of E-MDI-QKD

In order to compute the bit-parity in table 6.1, we can project the four-photon input polarisation state  $|\Psi_{L_a}\Psi_{B_X}\Psi_{L_b}\rangle$  onto the measurement polarisation state  $\langle\psi^+\psi^+|$ . We use the symbols  $|\phi^+\rangle$ ,  $|\phi^-\rangle$ ,  $|\psi^+\rangle$ , and  $|\psi^-\rangle$  to denote the four Bell states as defined in Eqs. (2.6)f.

For an FSS of zero we use  $|\Psi_{B_X}\rangle = |\phi^+\rangle$ . When encoding both laser inputs in horizontal polarisation, we compute (via substitution and regrouping):

$$\begin{aligned} |H\phi^+H\rangle &= \frac{1}{\sqrt{2}}(|HHHH\rangle + |HV VH\rangle) \\ &= \frac{1}{2\sqrt{2}}\left(|\phi^+\phi^+\rangle + |\phi^+\phi^-\rangle + |\phi^-\phi^+\rangle + |\phi^-\phi^-\rangle \right. \\ &\quad \left. + |\psi^+\psi^+\rangle + |\psi^+\psi^-\rangle + |\psi^-\psi^+\rangle + |\psi^-\psi^-\rangle\right), \end{aligned} \quad (\text{A.1})$$

therefore  $\langle\psi^+\psi^+|H\phi^+H\rangle \neq 0$  and via an analogous computation  $\langle\psi^+\psi^+|V\phi^+V\rangle \neq 0$ . In contrast, we find  $\langle\psi^+\psi^+|H\phi^+V\rangle = \langle\psi^+\psi^+|V\phi^+H\rangle = 0$ . As a result, altogether a four-photon coincidence indicates even bit parity in the rectilinear basis.

Likewise, in the diagonal basis we find  $\langle\psi^+\psi^+|D\phi^+D\rangle = \langle\psi^+\psi^+|A\phi^+A\rangle \neq 0$  and  $\langle\psi^+\psi^+|D\phi^+A\rangle = \langle\psi^+\psi^+|A\phi^+D\rangle = 0$ . Thus in the diagonal basis, too, a four-photon coincidence indicates even bit parity.

## A.2 Unintentional four-photon correlations

In Eq. (6.12) of Ch. 6.2.1 we calculated the fourth-order correlation  $g^{(4)}(t_1, t_2, t_3, t_4)$  measured on the detectors in E-MDI-QKD. The term  $\tilde{g}^{(4)}(t_1, t_2, t_3, t_4)$  in this equation describes the resulting four-order correlation from mixed E-LED emission or unintentional four-photon coincidences and reads:

$$\begin{aligned}
\tilde{g}^{(4)}(t_1, t_2, t_3, t_4) = & \frac{1}{4} \left[ \cos^2 \theta_{L_a} \cos^2 \theta_{L_b} I_{L_a}(t_1) I_{L_b}(t_3) g_{BX, mixed}^{(2)}(t_2, t_4) \right. \\
& + \sin^2 \theta_{L_a} \sin^2 \theta_{L_b} I_{L_a}(t_2) I_{L_b}(t_4) g_{BX, mixed}^{(2)}(t_1, t_3) \\
& + \cos^2 \theta_{L_a} \sin^2 \theta_{L_b} I_{L_a}(t_1) I_{L_b}(t_4) g_{BX, mixed}^{(2)}(t_2, t_3) \\
& \left. + \sin^2 \theta_{L_a} \cos^2 \theta_{L_b} I_{L_a}(t_2) I_{L_b}(t_3) g_{BX, mixed}^{(2)}(t_1, t_4) \right] \\
& + \frac{1}{2} \frac{\eta_{L_a}}{\eta_B} \cos^2(\theta_{L_a}) \sin^2(\theta_{L_a}) I_{L_a}(t_1) I_{L_a}(t_2) \\
& \times \left[ \sin^2(\theta_{L_b}) I_X(t_3) I_{L_b}(t_4) + \cos^2(\theta_{L_b}) I_{L_b}(t_3) I_X(t_4) \right] \\
& + \frac{1}{2} \frac{\eta_{L_b}}{\eta_X} \cos^2(\theta_{L_b}) \sin^2(\theta_{L_b}) I_{L_b}(t_3) I_{L_b}(t_4) \\
& \times \left[ \cos^2(\theta_{L_a}) I_{L_a}(t_1) I_B(t_2) + \sin^2(\theta_{L_a}) I_B(t_1) I_{L_a}(t_2) \right] \\
& + \frac{1}{4} \frac{\eta_B}{\eta_{L_a}} \left[ \sin^2(\theta_{L_b}) I_{L_b}(t_4) g_{BBX}^{(3)}(t_1, t_2, t_3) \right. \\
& \quad \left. + \cos^2(\theta_{L_b}) I_{L_b}(t_3) g_{BBX}^{(3)}(t_1, t_2, t_4) \right] \tag{A.2} \\
& + \frac{1}{4} \frac{\eta_X}{\eta_{L_b}} \left[ \sin^2(\theta_{L_a}) I_{L_a}(t_2) g_{BXX}^{(3)}(t_1, t_3, t_4) \right. \\
& \quad \left. + \cos^2(\theta_{L_a}) I_{L_a}(t_1) g_{BXX}^{(3)}(t_2, t_3, t_4) \right] \\
& + \frac{1}{2} \frac{\eta_{L_a} \eta_X}{\eta_{L_b} \eta_B} \cos^2(\theta_{L_a}) \sin^2(\theta_{L_a}) I_{L_a}(t_1) I_{L_a}(t_2) g_{XX}^{(2)}(t_3, t_4) \\
& + \frac{1}{2} \frac{\eta_{L_b} \eta_B}{\eta_{L_a} \eta_X} \cos^2(\theta_{L_b}) \sin^2(\theta_{L_b}) I_{L_b}(t_3) I_{L_b}(t_4) g_{BB}^{(2)}(t_1, t_2) \\
& + \frac{\eta_{L_a} \eta_{L_b}}{\eta_B \eta_X} \cos^2(\theta_{L_a}) \sin^2(\theta_{L_a}) \cos^2(\theta_{L_b}) \sin^2(\theta_{L_b}) \\
& \quad \times I_{L_a}(t_1) I_{L_a}(t_2) I_{L_b}(t_3) I_{L_b}(t_4) \\
& + \frac{1}{4} \frac{\eta_B \eta_X}{\eta_{L_a} \eta_{L_b}} g_{BBXX}^{(4)}(t_1, t_2, t_3, t_4).
\end{aligned}$$

Here, we've made the additional substitutions

$$A_{jkl}^2(t_j, t_k, t_l) = n_j n_k n_l g_{jkl}^{(3)}(t_j, t_k, t_l), \tag{A.3}$$

$$A_{jklm}^2(t_j, t_k, t_l, t_m) = n_j n_k n_l n_m g_{jklm}^{(4)}(t_j, t_k, t_l, t_m). \tag{A.4}$$

The first four lines of Eq. (A.2) describe the contribution from maximally-mixed E-LED emission. The subsequent terms describe contributions from multi-photon

events, i.e. multiple clicks from the same laser pulse or emission of multiple  $XX$  or  $X$  photons in the same clock cycle.

### A.3 Regions of anti-correlated bit parity

In Ch. 6.3.1 the figures 6.5a and b, 6.6b, and 6.7 clearly show regions of anti-correlated input bits with fidelity  $F_{\text{MDI}} < 0.5$ . This is perhaps surprising, since one might expect at least merely uncorrelated coincidences when the MDI-QKD scheme fails, instead of anti-correlated.

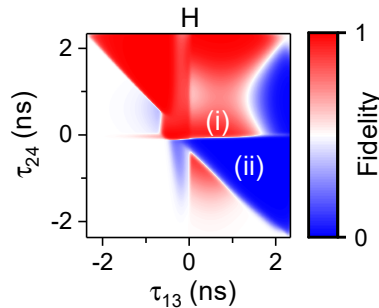


Figure A.1: Fidelity  $F_{\text{MDI},H}$  for an input encoding of  $|H\rangle$  for laser  $A$ . Regions of highly correlated (red) and anti-correlated (blue) input bit parity form. Panel reproduced from Fig. 6.5a.

We provide an intuitive explanation for this anti-correlation based on Fig. 6.5a as an example, which is reproduced again here as Fig. A.1 for convenience. The figure shows the fidelity  $F_{\text{MDI}}$  for the case where Alice emits her WCP in the  $|H\rangle$  state. In the ideal case, the entangled  $XX$ - $X$  pair is projected onto the detector polarisation states  $|V_1\rangle$  and  $|V_2\rangle$ . Due to the radiative cascade,  $X$  is emitted after  $XX$ , leading to  $\tau_{24} > 0$ —marked as region (i).

In the region marked as (ii) in Fig. A.1, however,  $\tau_{24} < 0$ , thus precluding the case described above. Instead, the most likely event leading to a four-photon coincidence in this region is as follows: A (partially) mixed  $XX$ - $X$  pair is emitted from the QD, and projected onto  $|V_1\rangle$  and  $|H_2\rangle$ . Now there are two possibilities:

1. Bob happens to emit his WCP in the  $|V\rangle$  state, projected onto the detector state  $|V_2\rangle$ . In this case,  $\tau_{24}$  is the time delay from the biexciton detection to the detection of Bob's WCP and may be less than 0. The photons projected on the detector states  $|H_1\rangle, |V_1\rangle, |H_2\rangle, |V_2\rangle$  are, in order:  $L_a, XX, X, L_b$ . Alice's and Bob's input bits are anti-correlated.
2. Bob happens to emit his WCP in the  $|H\rangle$  state, same parity as Alice. However, now no photon is projected onto  $|V_2\rangle$ . Hence the fourth detector does not trigger, and no four-photon coincidence is registered. A click on the fourth detector now requires a further, unlikely event, such as the emission of a second  $X$  photon or perhaps a dark count on the detector.

Since the first possibility is much more likely than the second possibility, the input bits are overall anti-correlated, leading to a fidelity near 0 in this region. Nevertheless, since the projection of a  $XX-X$  pair onto orthogonal polarisation states ( $|V_1\rangle$  and  $|H_2\rangle$ ) is significantly less likely than projection onto equal polarisation states ( $|V_1\rangle$  and  $|V_2\rangle$ ), the probability of measuring a four-photon coincidence in region (ii) to begin with is much less likely than a four-photon coincidence in the high-fidelity region (i).

Analogous explanations can be made for the other regions of anti-correlation in Fig. A.1 and throughout Ch. 6.3.1.

# Bibliography

- [Aha10] I. Aharonovich, S. Castelletto, D. A. Simpson, A. D. Greentree, S. Praver, *Photophysics of chromium-related diamond single-photon emitters*, Physical Review A **81**, 043813 (2010)
- [Arc14] M. Arcari, I. Söllner, A. Javadi, S. Lindskov Hansen, S. Mahmoodian, J. Liu, H. Thyrrerstrup, E. H. Lee, J. D. Song, S. Stobbe, P. Lodahl, *Near-unity coupling efficiency of a quantum emitter to a photonic crystal waveguide*, Physical Review Letters **113**, 093603 (2014)
- [Ard14] P.-L. Ardel, L. Hanschke, K. A. Fischer, K. Müller, A. Kleinkauf, M. Koller, A. Bechtold, T. Simmet, J. Wierzbowski, H. Riedl, G. Abstreiter, J. J. Finley, *Dissipative preparation of the exciton and biexciton in self-assembled quantum dots on picosecond time scales*, Physical Review B **90**, 241404(R) (2014)
- [Aru19] F. Arute, K. Arya, R. Babbush, D. Bacon, J. C. Bardin, R. Barends, R. Biswas, S. Boixo, F. G. S. L. Brandao, D. A. Buell, B. Burkett, Y. Chen, Z. Chen, B. Chiaro, R. Collins, W. Courtney, A. Dunsworth, E. Farhi, B. Foxen, A. Fowler, et al., *Quantum supremacy using a programmable superconducting processor*, Nature **574**, 505 (2019)
- [Asp81] A. Aspect, P. Grangier, G. Roger, *Experimental Tests of Realistic Local Theories via Bell's Theorem*, Physical Review Letters **47**, 460 (1981)
- [Bab92] D. I. Babic, S. W. Corzine, *Analytic expressions for the reflection delay, penetration depth, and absorptance of quarter-wave dielectric mirrors*, IEEE Journal of Quantum Electronics **28**, 514 (1992)

- [Bar02] W. L. Barnes, G. Björk, J. M. Gérard, P. Jonsson, J. Wasey, P. T. Worthing, V. Zwiller, *Solid-state single photon sources: light collection strategies*, The European Physical Journal D - Atomic, Molecular and Optical Physics **18**, 197 (2002)
- [Bas18] F. Basso Basset, S. Bietti, M. Reindl, L. Esposito, A. Fedorov, D. Huber, A. Rastelli, E. Bonera, R. Trotta, S. Sanguinetti, *High-Yield Fabrication of Entangled Photon Emitters for Hybrid Quantum Networking Using High-Temperature Droplet Epitaxy*, Nano Letters **18**, 505 (2018)
- [Bas19] F. Basso Basset, M. B. Rota, C. Schimpf, D. Tedeschi, K. D. Zeuner, S. F. Covre da Silva, M. Reindl, V. Zwiller, K. D. Jöns, A. Rastelli, R. Trotta, *Entanglement Swapping with Photons Generated on Demand by a Quantum Dot*, Physical Review Letters **123**, 160501 (2019)
- [Bas21] F. Basso Basset, M. Valeri, E. Roccia, V. Muredda, D. Poderini, J. Neuwirth, N. Spagnolo, M. B. Rota, G. Carvacho, F. Sciarrino, R. Trotta, *Quantum key distribution with entangled photons generated on demand by a quantum dot*, Science Advances **7**, eabe6379 (2021)
- [Bay99] M. Bayer, A. Kuther, A. Forchel, A. Gorbunov, V. B. Timofeev, F. Schäfer, J. P. Reithmaier, T. L. Reinecke, S. N. Walck, *Electron and Hole  $g$  Factors and Exchange Interaction from Studies of the Exciton Fine Structure in  $In_{0.60}Ga_{0.40}As$  Quantum Dots*, Physical Review Letters **82**, 1748 (1999)
- [Bay02] M. Bayer, G. Ortner, O. Stern, A. Kuther, A. A. Gorbunov, A. Forchel, P. Hawrylak, S. Fafard, K. Hinzer, T. L. Reinecke, S. N. Walck, J. P. Reithmaier, F. Klopff, F. Schäfer, *Fine structure of neutral and charged excitons in self-assembled  $In(Ga)As/(Al)GaAs$  quantum dots*, Physical Review B **65**, 3216 (2002)
- [Bec01] C. Becher, A. Kiraz, P. Michler, A. Imamoğlu, W. V. Schoenfeld, P. M. Petroff, L. Zhang, E. Hu, *Nonclassical radiation from a single self-assembled  $InAs$  quantum dot*, Physical Review B **63**, 121312 (2001)

- [Bel64] J. S. Bell, *On the Einstein Podolsky Rosen paradox*, Physics Physique Fizika **1**, 195 (1964)
- [Ben84] C. H. Bennett, G. Brassard, *Quantum cryptography: Public key distribution and coin tossing*, in *International Conference on Computers, Systems & Signal Processing*, volume 560, pp. 7–11 (1984)
- [Ben92] C. H. Bennett, G. Brassard, N. D. Mermin, *Quantum cryptography without Bell's theorem*, Physical Review Letters **68**, 557 (1992)
- [Ben93] C. H. Bennett, G. Brassard, C. Crépeau, R. Jozsa, A. Peres, W. K. Wootters, *Teleporting an unknown quantum state via dual classical and Einstein-Podolsky-Rosen channels*, Physical Review Letters **70**, 1895 (1993)
- [Ben00] O. Benson, C. Santori, M. Pelton, Y. Yamamoto, *Regulated and entangled photons from a single quantum dot*, Physical Review Letters **84**, 2513 (2000)
- [Ben05] A. J. Bennett, D. C. Unitt, P. See, A. J. Shields, P. Atkinson, K. Cooper, D. A. Ritchie, *Electrical control of the uncertainty in the time of single photon emission events*, Physical Review B **72**, 033316 (2005)
- [Ben08] A. J. Bennett, R. B. Patel, A. J. Shields, K. Cooper, P. Atkinson, C. A. Nicoll, D. A. Ritchie, *Indistinguishable photons from a diode*, Applied Physics Letters **92**, 193503 (2008)
- [Ben09] A. J. Bennett, R. B. Patel, C. A. Nicoll, D. A. Ritchie, A. J. Shields, *Interference of dissimilar photon sources*, Nature Physics **5**, 715 (2009)
- [Ben10a] A. J. Bennett, R. B. Patel, J. Skiba-Szymanska, C. A. Nicoll, I. Farrer, D. A. Ritchie, A. J. Shields, *Giant Stark effect in the emission of single semiconductor quantum dots*, Applied Physics Letters **97**, 031104 (2010)
- [Ben10b] A. J. Bennett, M. A. Pooley, R. M. Stevenson, M. B. Ward, R. B. Patel, A. B. de La Giroday, N. Sköld, I. Farrer, C. A. Nicoll, D. A. Ritchie, A. J. Shields, *Electric-field-induced coherent coupling of the exciton states in a single quantum dot*, Nature Physics **6**, 947 (2010)

- [Bha20] M. K. Bhaskar, R. Riedinger, B. Machielse, D. S. Levonian, C. T. Nguyen, E. N. Knall, H. Park, D. Englund, M. Lončar, D. D. Sukachev, M. D. Lukin, *Experimental demonstration of memory-enhanced quantum communication*, Nature **580**, 60 (2020)
- [Bim01] D. Bimberg, M. Grundmann, N. N. Ledencov, *Quantum dot heterostructures* (Wiley, Chichester, 2001), reprinted edition, ISBN 978-0-471-97388-1
- [Boa18] A. Boaron, G. Boso, D. Rusca, C. Vulliez, C. Autebert, M. Caloz, M. Perrenoud, G. Gras, F. Bussières, M.-J. Li, D. Nolan, A. Martin, H. Zbinden, *Secure Quantum Key Distribution over 421 km of Optical Fiber*, Physical Review Letters **121**, 190502 (2018)
- [Böc08] C. Böckler, S. Reitzenstein, C. Kistner, R. Debusmann, A. Löffler, T. Kida, S. Höfling, A. Forchel, L. Grenouillet, J. Claudon, J. M. Gérard, *Electrically driven high-Q quantum dot-micropillar cavities*, Applied Physics Letters **92**, 091107 (2008)
- [Bou15] S. Bounouar, M. Müller, A. M. Barth, M. Glässl, V. M. Axt, P. Michler, *Phonon-assisted robust and deterministic two-photon biexciton preparation in a quantum dot*, Physical Review B **91**, 161302(R) (2015)
- [Bou18] S. Bounouar, C. d. La Haye, M. Strauß, P. Schnauber, A. Thoma, M. Gschrey, J.-H. Schulze, A. Strittmatter, S. Rodt, S. Reitzenstein, *Generation of maximally entangled states and coherent control in quantum dot microlenses*, Applied Physics Letters **112**, 153107 (2018)
- [Bri98] H.-J. Briegel, W. Dür, J. I. Cirac, P. Zoller, *Quantum Repeaters: The Role of Imperfect Local Operations in Quantum Communication*, Physical Review Letters **81**, 5932 (1998)
- [Buc12] S. Buckley, K. Rivoire, J. Vučković, *Engineered quantum dot single-photon sources*, Reports on Progress in Physics **75**, 126503 (2012)

- [Cha02] H. F. Chau, *Practical scheme to share a secret key through a quantum channel with a 27.6% bit error rate*, Physical Review A **66**, 060302(R) (2002)
- [Cha20] P. Chaiwongkhot, S. Hosseini, A. Ahmadi, B. L. Higgins, D. Dalacu, P. J. Poole, R. L. Williams, M. E. Reimer, T. Jennewein, *Enhancing secure key rates of satellite QKD using a quantum dot single-photon source*, <http://arxiv.org/pdf/2009.11818v1> (2020)
- [Che18] Y. Chen, M. Zopf, R. Keil, F. Ding, O. G. Schmidt, *Highly-efficient extraction of entangled photons from quantum dots using a broadband optical antenna*, Nature Communications **9**, 2994 (2018)
- [Cho07] C.-W. Chou, J. Laurat, H. Deng, K. S. Choi, H. de Riedmatten, D. Felinto, H. J. Kimble, *Functional quantum nodes for entanglement distribution over scalable quantum networks*, Science **316**, 1316 (2007)
- [Cir95] J. I. Cirac, P. Zoller, *Quantum Computations with Cold Trapped Ions*, Physical Review Letters **74**, 4091 (1995)
- [Cla69] J. F. Clauser, M. A. Horne, A. Shimony, R. A. Holt, *Proposed Experiment to Test Local Hidden-Variable Theories*, Physical Review Letters **23**, 880 (1969)
- [Cla08] J. Clarke, F. K. Wilhelm, *Superconducting quantum bits*, Nature **453**, 1031 (2008)
- [Din16] X. Ding, Y. He, Z.-C. Duan, N. Gregersen, M.-C. Chen, S. Unsleber, S. Maier, C. Schneider, M. Kamp, S. Höfling, C.-Y. Lu, J.-W. Pan, *On-Demand Single Photons with High Extraction Efficiency and Near-Unity Indistinguishability from a Resonantly Driven Quantum Dot in a Micropillar*, Physical Review Letters **116**, 020401 (2016)

- [Doh13] M. W. Doherty, N. B. Manson, P. Delaney, F. Jelezko, J. Wrachtrup, L. C. Hollenberg, *The nitrogen-vacancy colour centre in diamond*, Physics Reports **528**, 1 (2013)
- [Dou10] A. Dousse, J. Suffczyński, A. Beveratos, O. Krebs, A. Lemaître, I. Sagnes, J. Bloch, P. Voisin, P. Senellart, *Ultrabright source of entangled photon pairs*, Nature **466**, 217 (2010)
- [Dre94] H. Drexler, D. Leonard, W. Hansen, J. P. Kotthaus, P. M. Petroff, *Spectroscopy of quantum levels in charge-tunable InGaAs quantum dots*, Physical Review Letters **73**, 2252 (1994)
- [Dür99] W. Dür, H.-J. Briegel, J. I. Cirac, P. Zoller, *Quantum repeaters based on entanglement purification*, Physical Review A **59**, 169 (1999)
- [Dzu15] B. Dzurnak, R. M. Stevenson, J. Nilsson, J. F. Dynes, Z. L. Yuan, J. Skiba-Szymanska, I. Farrer, D. A. Ritchie, A. J. Shields, *Quantum key distribution with an entangled light emitting diode*, Applied Physics Letters **107**, 261101 (2015)
- [Ein35] A. Einstein, B. Podolsky, N. Rosen, *Can Quantum-Mechanical Description of Physical Reality Be Considered Complete?*, Physical Review **47**, 777 (1935)
- [Eke91] A. K. Ekert, *Quantum cryptography based on Bell's theorem*, Physical Review Letters **67**, 661 (1991)
- [Eke98] A. Ekert, R. Jozsa, *Quantum algorithms: entanglement-enhanced information processing*, Philosophical Transactions of the Royal Society of London. Series A: Mathematical, Physical and Engineering Sciences **356**, 1769 (1998)
- [Ell06] D. J. P. Ellis, A. J. Bennett, A. J. Shields, P. Atkinson, D. A. Ritchie, *Electrically addressing a single self-assembled quantum dot*, Applied Physics Letters **88**, 133509 (2006)

- [Fey86] R. P. Feynman, *Quantum mechanical computers*, Foundations of Physics **16**, 507 (1986)
- [Fin01] J. J. Finley, A. D. Ashmore, A. Lemaître, D. J. Mowbray, M. S. Skolnick, I. E. Itskevich, P. A. Maksym, M. Hopkinson, T. F. Krauss, *Charged and neutral exciton complexes in individual self-assembled In(Ga)As quantum dots*, Physical Review B **63**, 073307 (2001)
- [Fla19] F. Flamini, N. Spagnolo, F. Sciarrino, *Photonic quantum information processing: a review*, Reports on Progress in Physics **82**, 016001 (2019)
- [Fog17] A. Fognini, A. Ahmadi, M. Zeeshan, J. T. Fokkens, S. J. Gibson, N. Sherlekar, S. J. Daley, D. Dalacu, P. J. Poole, K. D. Jöns, V. Zwiller, M. E. Reimer, *Path to perfect photon entanglement with a quantum dot*, <https://arxiv.org/abs/1710.10815> (2017)
- [Fow89] G. R. Fowles, *Introduction to Modern Optics* (Dover Publications, New York, 1989), 2nd edition, ISBN 978-0-486-65957-2
- [Fox06] M. Fox, *Quantum optics: An introduction*, volume 6 of *Oxford master series in physics* (Oxford University Press, Oxford, 2006), ISBN 978-0-19-856673-1
- [Fry00a] P. W. Fry, J. J. Finley, L. R. Wilson, A. Lemaître, D. J. Mowbray, M. S. Skolnick, M. Hopkinson, G. Hill, J. C. Clark, *Electric-field-dependent carrier capture and escape in self-assembled InAs/GaAs quantum dots*, Applied Physics Letters **77**, 4344 (2000)
- [Fry00b] P. W. Fry, I. E. Itskevich, D. J. Mowbray, M. S. Skolnick, J. J. Finley, J. A. Barker, E. P. O'Reilly, L. R. Wilson, I. A. Larkin, P. A. Maksym, M. Hopkinson, M. Al-Khafaji, J. P. David, A. G. Cullis, G. Hill, J. C. Clark, *Inverted electron-hole alignment in InAs-GaAs self-assembled quantum dots*, Physical Review Letters **84**, 733 (2000)
- [Fun10] C.-H. F. Fung, X. Ma, H. F. Chau, *Practical issues in quantum-key-distribution postprocessing*, Physical Review A **81**, 012318 (2010)

- [Gam96] D. Gammon, E. S. Snow, B. V. Shanabrook, D. S. Katzer, D. Park, *Fine structure splitting in the optical spectra of single GaAs quantum dots*, Physical Review Letters **76**, 3005 (1996)
- [Gao12] W. B. Gao, P. Fallahi, E. Togan, J. Miguel-Sanchez, A. Imamoglu, *Observation of entanglement between a quantum dot spin and a single photon*, Nature **491**, 426 (2012)
- [Ger07] B. D. Gerardot, S. Seidl, P. A. Dalgarno, R. J. Warburton, D. Granados, J. M. Garcia, K. Kowalik, O. Krebs, K. Karrai, A. Badolato, P. M. Petroff, *Manipulating exciton fine structure in quantum dots with a lateral electric field*, Applied Physics Letters **90**, 041101 (2007)
- [Gis02] N. Gisin, G. Ribordy, W. Tittel, H. Zbinden, *Quantum cryptography*, Reviews of Modern Physics **74**, 145 (2002)
- [Gis07] N. Gisin, R. Thew, *Quantum communication: Landscapes compared*, Nature Photonics **1**, 165 (2007)
- [Glä13a] M. Glässl, A. M. Barth, V. M. Axt, *Proposed robust and high-fidelity preparation of excitons and biexcitons in semiconductor quantum dots making active use of phonons*, Physical Review Letters **110**, 147401 (2013)
- [Glä13b] M. Glässl, A. M. Barth, K. Gawarecki, P. Machnikowski, M. D. Croitoru, S. Lüker, D. E. Reiter, T. Kuhn, V. M. Axt, *Biexciton state preparation in a quantum dot via adiabatic rapid passage: Comparison between two control protocols and impact of phonon-induced dephasing*, Physical Review B **87**, 085303 (2013)
- [Gop88] A. Gopinath, H. Atwater, *Simulation of GaAs p-i-n diodes*, IEEE Transactions on Electron Devices **35**, 414 (1988)
- [Gsc13] M. Gschrey, F. Gericke, A. Schübler, R. Schmidt, J.-H. Schulze, T. Heindel, S. Rodt, A. Strittmatter, S. Reitzenstein, *In situ electron-beam lithography of deterministic single-quantum-dot mesa-structures using low-temperature*

- cathodoluminescence spectroscopy*, Applied Physics Letters **102**, 251113 (2013)
- [Gsc15] M. Gschrey, A. Thoma, P. Schnauber, M. Seifried, R. Schmidt, B. Wohlfeil, L. Krüger, J.-H. Schulze, T. Heindel, S. Burger, F. Schmidt, A. Strittmatter, S. Rodt, S. Reitzenstein, *Highly indistinguishable photons from deterministic quantum-dot microlenses utilizing three-dimensional in situ electron-beam lithography*, Nature Communications **6**, 7662 (2015)
- [Han18] L. Hanschke, K. A. Fischer, S. Appel, D. Lukin, J. Wierzbowski, S. Sun, R. Trivedi, J. Vučković, J. J. Finley, K. Müller, *Quantum dot single-photon sources with ultra-low multi-photon probability*, npj Quantum Information **4**, 1026 (2018)
- [Har13] F. Hargart, C. A. Kessler, T. Schwarzbäck, E. Koroknay, S. Weidenfeld, M. Jetter, P. Michler, *Electrically driven quantum dot single-photon source at 2 GHz excitation repetition rate with ultra-low emission time jitter*, Applied Physics Letters **102**, 011126 (2013)
- [Hef92] B. L. Heffner, *Deterministic, analytically complete measurement of polarization-dependent transmission through optical devices*, IEEE Photonics Technology Letters **4**, 451 (1992)
- [Hei17] T. Heindel, A. Thoma, M. von Helversen, M. Schmidt, A. Schlehahn, M. Gschrey, P. Schnauber, J.-H. Schulze, A. Strittmatter, J. Beyer, S. Rodt, A. Carmele, A. Knorr, S. Reitzenstein, *A bright triggered twin-photon source in the solid state*, Nature Communications **8**, 14870 (2017)
- [Hel98] W. Heller, U. Bockelmann, G. Abstreiter, *Electric-field effects on excitons in quantum dots*, Physical Review B **57**, 6270 (1998)
- [Hel01] J. N. Helbert, *Handbook of VLSI Microlithography, 2nd Edition: Principles, Technology and Applications*, Materials Science and Process Technology (Elsevier professional, s.l., 2001), 2nd edition, ISBN 978-0-08-094680-1

- [Hon87] C. K. Hong, Z. Y. Ou, L. Mandel, *Measurement of subpicosecond time intervals between two photons by interference*, Physical Review Letters **59**, 2044 (1987)
- [Hou12] J. Houel, A. V. Kuhlmann, L. Greuter, F. Xue, M. Poggio, B. D. Gerardot, P. A. Dalgarno, A. Badolato, P. M. Petroff, A. Ludwig, D. Reuter, A. D. Wieck, R. J. Warburton, *Probing single-charge fluctuations at a GaAs/AlAs interface using laser spectroscopy on a nearby InGaAs quantum dot*, Physical Review Letters **108**, 107401 (2012)
- [Hub17] D. Huber, M. Reindl, Y. Huo, H. Huang, J. S. Wildmann, O. G. Schmidt, A. Rastelli, R. Trotta, *Highly indistinguishable and strongly entangled photons from symmetric GaAs quantum dots*, Nature Communications **8**, 15506 (2017)
- [Hub18a] D. Huber, M. Reindl, J. Aberl, A. Rastelli, R. Trotta, *Semiconductor quantum dots as an ideal source of polarization-entangled photon pairs on-demand: a review*, Journal of Optics **20**, 073002 (2018)
- [Hub18b] D. Huber, M. Reindl, S. F. Covre da Silva, C. Schimpf, J. Martín-Sánchez, H. Huang, G. Piredda, J. Edlinger, A. Rastelli, R. Trotta, *Strain-Tunable GaAs Quantum Dot: A Nearly Dephasing-Free Source of Entangled Photon Pairs on Demand: An on-demand source of nearly-maximally entangled photon pairs*, Physical Review Letters **121**, 033902 (2018)
- [Hud07] A. J. Hudson, R. M. Stevenson, A. J. Bennett, R. J. Young, C. A. Nicoll, P. Atkinson, K. Cooper, D. A. Ritchie, A. J. Shields, *Coherence of an entangled exciton-photon state*, Physical Review Letters **99**, 266802 (2007)
- [Huo13] Y. H. Huo, A. Rastelli, O. G. Schmidt, *Ultra-small excitonic fine structure splitting in highly symmetric quantum dots on GaAs (001) substrate*, Applied Physics Letters **102**, 152105 (2013)

- [Huw17] J. Huwer, R. M. Stevenson, J. Skiba-Szymanska, M. B. Ward, A. J. Shields, M. Felle, I. Farrer, D. A. Ritchie, R. V. Penty, *Quantum-Dot-Based Telecommunication-Wavelength Quantum Relay*, *Physical Review Applied* **8**, 024007 (2017)
- [Hwa03] W.-Y. Hwang, *Quantum key distribution with high loss: toward global secure communication*, *Physical Review Letters* **91**, 057901 (2003)
- [Int15] International Telecommunication Union, *Nomenclature of the frequency and wavelength bands used in telecommunications: Recommendation ITU-R V.431-8* (2015)
- [Jam01] D. F. V. James, P. G. Kwiat, W. J. Munro, A. G. White, *Measurement of qubits*, *Physical Review A* **64**, 052312 (2001)
- [Jon41] R. C. Jones, *A New Calculus for the Treatment of Optical Systems I Description and Discussion of the Calculus*, *Journal of the Optical Society of America* **31**, 488 (1941)
- [Jon47] R. C. Jones, *A New Calculus for the Treatment of Optical Systems VI Experimental Determination of the Matrix\**, *Journal of the Optical Society of America* **37**, 110 (1947)
- [Jon97] K. A. Jones, M. W. Cole, W. Y. Han, D. W. Eckart, K. P. Hilton, M. A. Crouch, B. H. Hughes, *Comparison of PdGeTiPt and NiGeAu ohmic contacts to n-GaAs and PdGeTiPt and TiPd contacts to p+-GaAs*, *Journal of Applied Physics* **82**, 1723 (1997)
- [Joy04] B. A. Joyce, D. D. Vvedensky, *Self-organized growth on GaAs surfaces*, *Materials Science and Engineering R* **46**, 127 (2004)
- [Joz94] R. Jozsa, *Fidelity for Mixed Quantum States*, *Journal of Modern Optics* **41**, 2315 (1994)
- [Kal17a] N. Kalb, A. A. Reiserer, P. C. Humphreys, J. J. W. Bakermans, S. J. Kamerling, N. H. Nickerson, S. C. Benjamin, D. J. Twitchen, M. Markham,

- R. Hanson, *Entanglement distillation between solid-state quantum network nodes*, Science **356**, 928 (2017)
- [Kal17b] T. Kaldewey, S. Lüker, A. V. Kuhlmann, S. R. Valentin, A. Ludwig, A. D. Wieck, D. E. Reiter, T. Kuhn, R. J. Warburton, *Coherent and robust high-fidelity generation of a biexciton in a quantum dot by rapid adiabatic passage*, Physical Review B **95**, 161302(R) (2017)
- [Kan98] B. E. Kane, *A silicon-based nuclear spin quantum computer*, Nature **393**, 133 (1998)
- [Kan17] M. Kantner, M. Mittnenzweig, T. Koprucki, *Hybrid quantum-classical modeling of quantum dot devices*, Physical Review B **96**, 205301 (2017)
- [Kei17] R. Keil, M. Zopf, Y. Chen, B. Höfer, J. Zhang, F. Ding, O. G. Schmidt, *Solid-state ensemble of highly entangled photon sources at rubidium atomic transitions*, Nature Communications **8**, 15501 (2017)
- [Kim08] H. J. Kimble, *The quantum internet*, Nature **453**, 1023 (2008)
- [Kir17] G. Kiršanskė, H. Thyrrerstrup, R. S. Daveau, C. L. Dreeßen, T. Pregolato, L. Midolo, P. Tighineanu, A. Javadi, S. Stobbe, R. Schott, A. Ludwig, A. D. Wieck, S. I. Park, J. D. Song, A. V. Kuhlmann, I. Söllner, M. C. Löbl, R. J. Warburton, P. Lodahl, *Indistinguishable and efficient single photons from a quantum dot in a planar nanobeam waveguide*, Physical Review B **96**, 174 (2017)
- [Kni01] E. Knill, R. Laflamme, G. J. Milburn, *A scheme for efficient quantum computation with linear optics*, Nature **409**, 46 (2001)
- [Kuh15] A. V. Kuhlmann, J. H. Prechtel, J. Houel, A. Ludwig, D. Reuter, A. D. Wieck, R. J. Warburton, *Transform-limited single photons from a single quantum dot*, Nature Communications **6**, 8204 (2015)

- [Kul04] N. Kularatna, D. Dias, *Essentials of modern telecommunications systems*, Artech House telecommunications library (Artech House, Boston and London, 2004), ISBN 978-1-58053-491-8
- [Kup20] T. Kupko, M. von Helversen, L. Rickert, J.-H. Schulze, A. Strittmatter, M. Gschrey, S. Rodt, S. Reitzenstein, T. Heindel, *Tools for the performance optimization of single-photon quantum key distribution*, npj Quantum Information **6**, 29 (2020)
- [Kur13] T. Kuroda, T. Mano, N. Ha, H. Nakajima, H. Kumano, B. Urbaszek, M. Jo, M. Abbarchi, Y. Sakuma, K. Sakoda, I. Suemune, X. Marie, T. Amand, *Symmetric quantum dots as efficient sources of highly entangled photons: Violation of Bell's inequality without spectral and temporal filtering*, Physical Review B **88**, 041306(R) (2013)
- [Kwi95] P. G. Kwiat, K. Mattle, H. Weinfurter, A. Zeilinger, A. V. Sergienko, Y. Shih, *New high-intensity source of polarization-entangled photon pairs*, Physical Review Letters **75**, 4337 (1995)
- [Lee17] J. P. Lee, E. Murray, A. J. Bennett, D. J. P. Ellis, C. Dangel, I. Farrer, P. Spencer, D. A. Ritchie, A. J. Shields, *Electrically driven and electrically tunable quantum light sources*, Applied Physics Letters **110**, 071102 (2017)
- [Leg03] T. Legero, T. Wilk, A. Kuhn, G. Rempe, *Time-resolved two-photon quantum interference*, Applied Physics B **77**, 797 (2003)
- [Li21] B.-H. Li, Y.-M. Xie, Z. Li, C.-X. Weng, C.-L. Li, H.-L. Yin, Z.-B. Chen, *Long-distance twin-field quantum key distribution with entangled sources*, Optics Letters **46**, 5529 (2021)
- [Lin11] C.-H. Lin, W.-T. You, H.-Y. Chou, S.-J. Cheng, S.-D. Lin, W.-H. Chang, *Anticorrelation between the splitting and polarization of the exciton fine structure in single self-assembled InAs/GaAs quantum dots*, Physical Review B **83**, 075317 (2011)

- [Lin19] Y. Lin, Y. Ye, W. Fang, *Electrically driven single-photon sources*, Journal of Semiconductors **40**, 071904 (2019)
- [Liu18] F. Liu, A. J. Brash, J. O'Hara, L. M. P. P. Martins, C. L. Phillips, R. J. Coles, B. Royall, E. Clarke, C. Bentham, N. Prtljaga, I. E. Itskevich, L. R. Wilson, M. S. Skolnick, A. M. Fox, *High Purcell factor generation of indistinguishable on-chip single photons*, Nature Nanotechnology **13**, 835 (2018)
- [Liu19] J. Liu, R. Su, Y. Wei, B. Yao, S. F. C. d. Silva, Y. Yu, J. Iles-Smith, K. Srinivasan, A. Rastelli, J. Li, X. Wang, *A solid-state source of strongly entangled photon pairs with high brightness and indistinguishability*, Nature Nanotechnology **14**, 586 (2019)
- [Lo99] H.-K. Lo, H. F. Chau, *Unconditional security of quantum key distribution over arbitrarily long distances*, Science **283**, 2050 (1999)
- [Lo12] H.-K. Lo, M. Curty, B. Qi, *Measurement-device-independent quantum key distribution*, Physical Review Letters **108**, 130503 (2012)
- [Luc18] M. Lucamarini, Z. L. Yuan, J. F. Dynes, A. J. Shields, *Overcoming the rate-distance limit of quantum key distribution without quantum repeaters*, Nature **557**, 400 (2018)
- [Lüt99] N. Lütkenhaus, J. Calsamiglia, K.-A. Suominen, *Bell measurements for teleportation*, Physical Review A **59**, 3295 (1999)
- [Mic09] P. Michler, *Single semiconductor quantum dots*, Nanoscience and technology (Springer, Berlin, 2009), ISBN 978-3-540-87445-4
- [Min19] M. Minder, M. Pittaluga, G. L. Roberts, M. Lucamarini, J. F. Dynes, Z. L. Yuan, A. J. Shields, *Experimental quantum key distribution beyond the repeaterless secret key capacity*, Nature Photonics **13**, 334 (2019)
- [Mor01] E. Moreau, I. Robert, L. Manin, V. Thierry-Mieg, J. M. Gérard, I. Abram, *Quantum Cascade of Photons in Semiconductor Quantum Dots*, Physical Review Letters **87**, 183601 (2001)

- [Mül14] M. Müller, S. Bounouar, K. D. Jöns, M. Glässl, P. Michler, *On-demand generation of indistinguishable polarization-entangled photon pairs*, Nature Photonics **8**, 224 (2014)
- [Mül18] T. Müller, J. Skiba-Szymanska, A. B. Krysa, J. Huwer, M. Felle, M. Anderson, R. M. Stevenson, J. Heffernan, D. A. Ritchie, A. J. Shields, *A quantum light-emitting diode for the standard telecom window around 1,550 nm*, Nature Communications **9**, 862 (2018)
- [Mül20] J. R. A. Müller, R. M. Stevenson, J. Skiba-Szymanska, G. Shooter, J. Huwer, I. Farrer, D. A. Ritchie, A. J. Shields, *Active reset of a radiative cascade for entangled-photon generation beyond the continuous-driving limit*, Physical Review Research **2**, 043292 (2020)
- [Nie10] M. A. Nielsen, I. L. Chuang, *Quantum computation and quantum information* (Cambridge Univ. Press, Cambridge, 2010), 10th anniversary edition, ISBN 978-1-107-00217-3
- [Nil13] J. Nilsson, *Electrically generated entangled light for optical quantum information applications*, Doctoral thesis, Université Blaise Pascal, Clermont-Ferrand (2013)
- [Now14] A. K. Nowak, S. L. Portalupi, V. Giesz, O. Gazzano, C. Dal Savio, P.-F. Braun, K. Karrai, C. Arnold, L. Lanco, I. Sagnes, A. Lemaître, P. Senellart, *Deterministic and electrically tunable bright single-photon source*, Nature Communications **5**, 3240 (2014)
- [Olb17] F. Olbrich, J. Höschele, M. Müller, J. Kettler, S. Luca Portalupi, M. Paul, M. Jetter, P. Michler, *Polarization-entangled photons from an InGaAs-based quantum dot emitting in the telecom C-band*, Applied Physics Letters **111**, 133106 (2017)

- [Pat10] R. B. Patel, A. J. Bennett, I. Farrer, C. A. Nicoll, D. A. Ritchie, A. J. Shields, *Two-photon interference of the emission from electrically tunable remote quantum dots*, Nature Photonics **4**, 632 (2010)
- [Pau17] M. Paul, F. Olbrich, J. Höschel, S. Schreier, J. Kettler, S. L. Portalupi, M. Jetter, P. Michler, *Single-photon emission at 1.55  $\mu\text{m}$  from MOVPE-grown InAs quantum dots on InGaAs/GaAs metamorphic buffers*, Applied Physics Letters **111**, 033102 (2017)
- [Pel03] M. Pelton, J. Vučković, G. Solomon, C. Santori, B. Zhang, J. Plant, Y. Yamamoto, *An efficient source of single photons: a single quantum dot in a micropost microcavity*, Physica E: Low-dimensional Systems and Nanostructures **17**, 564 (2003)
- [Pit21] M. Pittaluga, M. Minder, M. Lucamarini, M. Sanzaro, R. I. Woodward, M.-J. Li, Z. Yuan, A. J. Shields, *600-km repeater-like quantum communications with dual-band stabilization*, Nature Photonics **15**, 530 (2021)
- [Qiu14] J. Qiu, *Quantum communications leap out of the lab*, Nature **508**, 441 (2014)
- [Rei18] M. Reindl, D. Huber, C. Schimpf, S. F. C. da Silva, M. B. Rota, H. Huang, V. Zwiller, K. D. Jöns, A. Rastelli, R. Trotta, *All-photon quantum teleportation using on-demand solid-state quantum emitters*, Science Advances **4**, eaau1255 (2018)
- [Sal10] C. L. Salter, R. M. Stevenson, I. Farrer, C. A. Nicoll, D. A. Ritchie, A. J. Shields, *An entangled-light-emitting diode*, Nature **465**, 594 (2010)
- [San11] N. Sangouard, C. Simon, H. de Riedmatten, N. Gisin, *Quantum repeaters based on atomic ensembles and linear optics*, Reviews of Modern Physics **83**, 33 (2011)
- [Sau20] K. E. Sautter, K. D. Vallejo, P. J. Simmonds, *Strain-driven quantum dot self-assembly by molecular beam epitaxy*, Journal of Applied Physics **128**, 031101 (2020)

- [Sbr22] F. Sbresny, L. Hanschke, E. Schöll, W. Rauhaus, B. Scaparra, K. Boos, E. Zubizarreta Casalengua, H. Riedl, E. Del Valle, J. J. Finley, K. D. Jöns, K. Müller, *Stimulated Generation of Indistinguishable Single Photons from a Quantum Ladder System*, Physical Review Letters **128**, 093603 (2022)
- [Sca09] V. Scarani, H. Bechmann-Pasquinucci, N. J. Cerf, M. Dušek, N. Lütkenhaus, M. Peev, *The security of practical quantum key distribution*, Reviews of Modern Physics **81**, 1301 (2009)
- [Sch09] A. Schliwa, M. Winkelnkemper, A. Lochmann, E. Stock, D. Bimberg, *In(Ga)As/GaAs quantum dots grown on a (111) surface as ideal sources of entangled photon pairs*, Physical Review B **80**, 161307 (2009)
- [Sch12] C. Schneider, S. Höfling, A. Forchel, *Growth of III–V semiconductor quantum dots*, in A. G. Tartakovskii (editor), *Quantum dots*, p. 3 (Cambridge University Press, Cambridge and New York, 2012), ISBN 978-1-107-01258-5
- [Sch16] A. Schlehahn, A. Thoma, P. Munnely, M. Kamp, S. Höfling, T. Heindel, C. Schneider, S. Reitzenstein, *An electrically driven cavity-enhanced source of indistinguishable photons with 61% overall efficiency*, APL Photonics **1**, 011301 (2016)
- [Sch20] E. Schöll, L. Schweickert, L. Hanschke, K. D. Zeuner, F. Sbresny, T. Lettner, R. Trivedi, M. Reindl, S. F. Da Covre Silva, R. Trotta, J. J. Finley, J. Vučković, K. Müller, A. Rastelli, V. Zwiller, K. D. Jöns, *Cruc of Using the Cascaded Emission of a Three-Level Quantum Ladder System to Generate Indistinguishable Photons*, Physical Review Letters **125**, 233605 (2020)
- [Sch21] C. Schimpf, M. Reindl, D. Huber, B. Lehner, S. F. Da Covre Silva, S. Manna, M. Vyvlecka, P. Walther, A. Rastelli, *Quantum cryptography with highly entangled photons from semiconductor quantum dots*, Science Advances **7**, eabe8905 (2021)

- [Scu97] M. O. Scully, M. S. Zubairy, *Quantum optics* (Cambridge University Press, Cambridge, 1997), ISBN 978-0-521-43595-6
- [Sei05] S. Seidl, M. Kroner, P. A. Dalgarno, A. Högele, J. M. Smith, M. Ediger, B. D. Gerardot, J. M. Garcia, P. M. Petroff, K. Karrai, R. J. Warburton, *Absorption and photoluminescence spectroscopy on a single self-assembled charge-tunable quantum dot*, *Physical Review B* **72**, 2958 (2005)
- [Sei06] S. Seidl, M. Kroner, A. Högele, K. Karrai, R. J. Warburton, A. Badolato, P. M. Petroff, *Effect of uniaxial stress on excitons in a self-assembled quantum dot*, *Applied Physics Letters* **88**, 203113 (2006)
- [Sen09] J. M. Senior, M. Y. Jamro, *Optical fiber communications: Principles and practice* (Prentice Hall, Harlow, 2009), 3rd edition, ISBN 978-0-13-032681-2
- [Sen12] P. Senellart, *Deterministic light-matter coupling with single quantum dots*, in A. G. Tartakovskii (editor), *Quantum dots*, p. 137 (Cambridge University Press, Cambridge and New York, 2012), ISBN 978-1-107-01258-5
- [Sen17] P. Senellart, G. Solomon, A. White, *High-performance semiconductor quantum-dot single-photon sources*, *Nature Nanotechnology* **12**, 1026 (2017)
- [Shi07] A. J. Shields, *Semiconductor quantum light sources*, *Nature Photonics* **1**, 215 (2007)
- [Sim05] C. Simon, J.-P. Poizat, *Creating single time-bin-entangled photon pairs*, *Physical Review Letters* **94**, 030502 (2005)
- [Som16] N. Somaschi, V. Giesz, L. de Santis, J. C. Loredó, M. P. Almeida, G. Hornecker, S. L. Portalupi, T. Grange, C. Antón, J. Demory, C. Gómez, I. Sagnes, N. D. Lanzillotti-Kimura, A. Lemaître, A. Auffeves, A. G. White, L. Lanco, P. Senellart, *Near-optimal single-photon sources in the solid state*, *Nature Photonics* **10**, 340 (2016)
- [SS17] J. Skiba-Szymanska, R. M. Stevenson, C. Varnava, M. Felle, J. Huwer, T. Müller, A. J. Bennett, J. p. Lee, I. Farrer, A. B. Krysa, P. Spencer, L. E.

- Goff, D. A. Ritchie, J. Heffernan, A. J. Shields, *Universal Growth Scheme for Quantum Dots with Low Fine-Structure Splitting at Various Emission Wavelengths*, *Physical Review Applied* **8**, 014013 (2017)
- [Ste02] R. M. Stevenson, R. M. Thompson, A. J. Shields, I. Farrer, B. E. Kardynal, D. A. Ritchie, M. Pepper, *Quantum dots as a photon source for passive quantum key encoding*, *Physical Review B* **66**, 081302 (2002)
- [Ste06] R. M. Stevenson, R. J. Young, P. Atkinson, K. Cooper, D. A. Ritchie, A. J. Shields, *A semiconductor source of triggered entangled photon pairs*, *Nature* **439**, 179 (2006)
- [Ste08] R. M. Stevenson, A. J. Hudson, A. J. Bennett, R. J. Young, C. A. Nicoll, D. A. Ritchie, A. J. Shields, *Evolution of entanglement between distinguishable light states*, *Physical Review Letters* **101**, 170501 (2008)
- [Ste12a] R. M. Stevenson, A. J. Bennett, A. J. Shields, *Electrically operated entangled light sources based on quantum dots*, in A. G. Tartakovskii (editor), *Quantum dots*, pp. 319–340 (Cambridge University Press, Cambridge and New York, 2012), ISBN 978-1-107-01258-5
- [Ste12b] R. M. Stevenson, C. L. Salter, J. Nilsson, A. J. Bennett, M. B. Ward, I. Farrer, D. A. Ritchie, A. J. Shields, *Indistinguishable entangled photons generated by a light-emitting diode*, *Physical Review Letters* **108**, 040503 (2012)
- [Ste17] D. A. Steck, *Classical and Modern Optics*, <http://steck.us/teaching> (2017)
- [Str37] I. N. Stranski, L. Krastanow, *Zur Theorie der orientierten Ausscheidung von Ionenkristallen aufeinander*, *Monatshefte für Chemie* **71**, 351 (1937)
- [Str76] I. Strzalkowski, S. Joshi, C. R. Crowell, *Dielectric constant and its temperature dependence for GaAs, CdTe, and ZnSe*, *Applied Physics Letters* **28**, 350 (1976)

- [Sze98] S. M. Sze (editor), *Modern semiconductor device physics*, A Wiley-Interscience publication (Wiley, New York, NY, 1998), ISBN 978-0-471-15237-8
- [Tah11] S. Tahamtan, A. Goodarzi, S. P. Abbasi, A. Hodaei, M. S. Zabihi, J. Sabbaghzadeh, *Investigation on the effect of annealing process parameters on AuGeNi ohmic contact to n-GaAs using microstructural characteristics*, *Microelectronics Reliability* **51**, 1330 (2011)
- [Tar12] A. G. Tartakovskii (editor), *Quantum dots: Optics, electron transport, and future applications* (Cambridge University Press, Cambridge and New York, 2012), ISBN 978-1-107-01258-5
- [Tro12] R. Trotta, E. Zallo, C. Ortix, P. Atkinson, J. D. Plumhof, J. van den Brink, A. Rastelli, O. G. Schmidt, *Universal recovery of the energy-level degeneracy of bright excitons in InGaAs quantum dots without a structure symmetry*, *Physical Review Letters* **109**, 147401 (2012)
- [Tro14] R. Trotta, J. S. Wildmann, E. Zallo, O. G. Schmidt, A. Rastelli, *Highly entangled photons from hybrid piezoelectric-semiconductor quantum dot devices*, *Nano Letters* **14**, 3439 (2014)
- [Tro16] R. Trotta, J. Martín-Sánchez, J. S. Wildmann, G. Piredda, M. Reindl, C. Schimpf, E. Zallo, S. Stroj, J. Edlinger, A. Rastelli, *Wavelength-tunable sources of entangled photons interfaced with atomic vapours*, *Nature Communications* **7**, 10375 (2016)
- [Uns16] S. Unsleber, Y.-M. He, S. Gerhardt, S. Maier, C.-Y. Lu, J.-W. Pan, N. Gregersen, M. Kamp, C. Schneider, S. Höfling, *Highly indistinguishable on-demand resonance fluorescence photons from a deterministic quantum dot micropillar device with 74% extraction efficiency*, *Optics Express* **24**, 8539 (2016)

- [Var67] Y. P. Varshni, *Temperature dependence of the energy gap in semiconductors*, *Physica* **34**, 149 (1967)
- [Var16] C. Varnava, R. M. Stevenson, J. Nilsson, J. Skiba-Szymanska, B. Dzurňák, M. Lucamarini, R. V. Penty, I. Farrer, D. A. Ritchie, A. J. Shields, *An entangled-LED-driven quantum relay over 1 km*, *npj Quantum Information* **2**, 145 (2016)
- [Ven01] J. A. Venables, *Introduction to surface and thin film processes* (Cambridge Univ. Press, Cambridge, 2001), reprinted edition, ISBN 978-0-521-78500-6
- [Vir20] P. Virtanen, R. Gommers, T. E. Oliphant, M. Haberland, T. Reddy, D. Cournapeau, E. Burovski, P. Peterson, W. Weckesser, J. Bright, S. J. van der Walt, M. Brett, J. Wilson, K. J. Millman, N. Mayorov, A. R. J. Nelson, E. Jones, R. Kern, E. Larson, C. J. Carey, Í. Polat, Y. Feng, E. W. Moore, J. VanderPlas, D. Laxalde, J. Perktold, R. Cimrman, I. Henriksen, E. A. Quintero, C. R. Harris, A. M. Archibald, A. H. Ribeiro, F. Pedregosa, P. van Mulbregt, *SciPy 1.0: fundamental algorithms for scientific computing in Python*, *Nature Methods* **17**, 261 (2020)
- [Vog07] M. M. Vogel, S. M. Ulrich, R. Hafenbrak, P. Michler, L. Wang, A. Rastelli, O. G. Schmidt, *Influence of lateral electric fields on multiexcitonic transitions and fine structure of single quantum dots*, *Applied Physics Letters* **91**, 051904 (2007)
- [Wah98] M. Wahl, R. Erdmann, K. Lauritsen, H.-J. Rahn, *Hardware solution for continuous time-resolved burst detection of single molecules in flow*, in G. E. Cohn (editor), *Systems and Technologies for Clinical Diagnostics and Drug Discovery*, SPIE Proceedings, pp. 173–178 (SPIE, 1998)
- [Wan08] Q. Wang, W. Chen, G. Xavier, M. Swillo, T. Zhang, S. Sauge, M. Tengner, Z.-F. Han, G.-C. Guo, A. Karlsson, *Experimental decoy-state quantum key distribution with a sub-poissonian heralded single-photon source*, *Physical Review Letters* **100**, 090501 (2008)

- [Wan16] X.-L. Wang, L.-K. Chen, W. Li, H.-L. Huang, C. Liu, C. Chen, Y.-H. Luo, Z.-E. Su, D. Wu, Z.-D. Li, H. Lu, Y. Hu, X. Jiang, C.-Z. Peng, L. Li, N.-L. Liu, Y.-A. Chen, C.-Y. Lu, J.-W. Pan, *Experimental Ten-Photon Entanglement*, Physical Review Letters **117**, 210502 (2016)
- [Wan19] H. Wang, H. Hu, T.-H. Chung, J. Qin, X. Yang, J.-P. Li, R.-Z. Liu, H.-S. Zhong, Y.-M. He, X. Ding, Y.-H. Deng, Q. Dai, Y.-H. Huo, S. Höfling, C.-Y. Lu, J.-W. Pan, *On-Demand Semiconductor Source of Entangled Photons Which Simultaneously Has High Fidelity, Efficiency, and Indistinguishability*, Physical Review Letters **122**, 113602 (2019)
- [Wan22] S. Wang, Z.-Q. Yin, D.-Y. He, W. Chen, R.-Q. Wang, P. Ye, Y. Zhou, G.-J. Fan-Yuan, F.-X. Wang, Y.-G. Zhu, P. V. Morozov, A. V. Divochiy, Z. Zhou, G.-C. Guo, Z.-F. Han, *Twin-field quantum key distribution over 830-km fibre*, Nature Photonics **16**, 154 (2022)
- [War00] R. J. Warburton, C. Schafflein, D. Haft, F. Bickel, A. Lorke, K. Karrai, J. M. Garcia, W. Schoenfeld, P. M. Petroff, *Optical emission from a charge-tunable quantum ring*, Nature **405**, 926 (2000)
- [War07] M. B. Ward, T. Farrow, P. See, Z. L. Yuan, O. Z. Karimov, A. J. Bennett, A. J. Shields, P. Atkinson, K. Cooper, D. A. Ritchie, *Electrically driven telecommunication wavelength single-photon source*, Applied Physics Letters **90**, 063512 (2007)
- [War14] M. B. Ward, M. C. Dean, R. M. Stevenson, A. J. Bennett, D. J. P. Ellis, K. Cooper, I. Farrer, C. A. Nicoll, D. A. Ritchie, A. J. Shields, *Coherent dynamics of a telecom-wavelength entangled photon source*, Nature Communications **5**, 3316 (2014)
- [Wol20] Wolfram Research, Inc., *Mathematica* (Wolfram Research, Inc., Champaign, Illinois, 2020), 12.2 edition

- [Woo98] W. K. Wootters, *Entanglement of Formation of an Arbitrary State of Two Qubits*, Physical Review Letters **80**, 2245 (1998)
- [Xia19] Z.-H. Xiang, J. Huwer, R. M. Stevenson, J. Skiba-Szymanska, M. B. Ward, I. Farrer, D. A. Ritchie, A. J. Shields, *Long-term transmission of entangled photons from a single quantum dot over deployed fiber*, Scientific Reports **9**, 4111 (2019)
- [Xu13] F. Xu, B. Qi, Z. Liao, H.-K. Lo, *Long distance measurement-device-independent quantum key distribution with entangled photon sources*, Applied Physics Letters **103**, 061101 (2013)
- [Xu15] F. Xu, M. Curty, B. Qi, Lo Hoi-Kwong, *Measurement-Device-Independent Quantum Cryptography*, IEEE Journal of Selected Topics in Quantum Electronics **21**, 148 (2015)
- [Xu20] F. Xu, X. Ma, Q. Zhang, H.-K. Lo, J.-W. Pan, *Secure quantum key distribution with realistic devices*, Reviews of Modern Physics **92**, 025002 (2020)
- [Yar89] A. Yariv, *Quantum electronics* (John Wiley & Sons, Hoboken and Toronto, 1989), 3rd edition, ISBN 978-0-471-60997-1
- [Yin16] H.-L. Yin, T.-Y. Chen, Z.-W. Yu, H. Liu, L.-X. You, Y.-H. Zhou, S.-J. Chen, Y. Mao, M.-Q. Huang, W.-J. Zhang, H. Chen, M. J. Li, D. Nolan, F. Zhou, X. Jiang, Z. Wang, Q. Zhang, X.-B. Wang, J.-W. Pan, *Measurement-Device-Independent Quantum Key Distribution Over a 404 km Optical Fiber*, Physical Review Letters **117**, 190501 (2016)
- [You05] R. J. Young, R. M. Stevenson, A. J. Shields, P. Atkinson, K. Cooper, D. A. Ritchie, K. M. Groom, A. I. Tartakovskii, M. S. Skolnick, *Inversion of exciton level splitting in quantum dots*, Physical Review B **72**, 113305 (2005)
- [You09] R. J. Young, R. M. Stevenson, A. J. Hudson, C. A. Nicoll, D. A. Ritchie, A. J. Shields, *Bell-inequality violation with a triggered photon-pair source*, Physical Review Letters **102**, 030406 (2009)

- [Yua02] Z. Yuan, B. E. Kardynal, R. M. Stevenson, A. J. Shields, C. J. Lobo, K. Cooper, N. S. Beattie, D. A. Ritchie, M. Pepper, *Electrically driven single-photon source*, *Science* **295**, 102 (2002)
- [Yua08] Z.-S. Yuan, Y.-A. Chen, B. Zhao, S. Chen, J. Schmiedmayer, J.-W. Pan, *Experimental demonstration of a BDCZ quantum repeater node*, *Nature* **454**, 1098 (2008)
- [Yua18] Z. Yuan, A. Plews, R. Takahashi, K. Doi, W. Tam, A. W. Sharpe, A. R. Dixon, E. Lavelle, J. F. Dynes, A. Murakami, M. Kujiraoka, M. Lucamarini, Y. Tanizawa, H. Sato, A. J. Shields, *10-Mb/s Quantum Key Distribution*, *Journal of Lightwave Technology* **36**, 3427 (2018)
- [Zha15] J. Zhang, J. S. Wildmann, F. Ding, R. Trotta, Y. Huo, E. Zallo, D. Huber, A. Rastelli, O. G. Schmidt, *High yield and ultrafast sources of electrically triggered entangled-photon pairs based on strain-tunable quantum dots*, *Nature Communications* **6**, 10067 (2015)
- [Zop19] M. Zopf, R. Keil, Y. Chen, J. Yang, D. Chen, F. Ding, O. G. Schmidt, *Entanglement Swapping with Semiconductor-Generated Photons Violates Bell's Inequality*, *Physical Review Letters* **123**, 160502 (2019)